ECAP-2018-001

Investigations of VUV-sensitive Photosensors at Cryogenic Temperatures for the nEXO Experiment

Master's thesis

submitted by

Judith Schneider

January 10, 2018

Physikalisches Institut IV
Erlangen Centre for Astroparticle Physics
Friedrich-Alexander-Universität Erlangen-Nürnberg

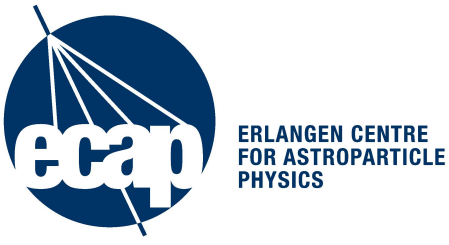

1. Supervisor: PD Dr. Thilo Michel
2. Supervisor: Prof. Dr. Gisela Anton

Contents

Introduction

Neutrinos are almost massless, have no electric charge nor colour charge and are the least interactive particles in the universe which makes them hard to detect. The neutrino has been postulated by W. Pauli in 1930 [1]. Only 25 years later – in 1956 – it has been detected by C. L. Cowan and F. Reines [2]. After 62 years of research, there are still many unknowns concerning the neutrino. The absolute masses are not known, neither is the exact mass hierarchy nor is known whether there exists an magnetic moment or if the neutrino is its own antiparticle. E. Majorana provided the mathematical description of a neutrino which is its own antiparticle [3]. Such particles are called Majorana particles. In 1939, W. H. Furry proposed the neutrinoless double beta decay ($0\nu\beta\beta$-decay) as a practical tool to prove the possible Majorana nature of the neutrino [4]. One of the future experiments to search for the $0\nu\beta\beta$-decay is the nEXO experiment. It will be realised with about 5 t of liquid xenon and silicon photomultiplier (SiPMs) to detect the vacuum ultraviolet (VUV)-scintillation light which is emitted when radiactive decays and other events deposit energy in the xenon. SiPMs are semiconductor photodetectors with a single photon resolution. A lot of pioneering work has been done in the 1960s by R. J. McIntyre and co-workers [5] as well as by R. H. Haitz and his colleagues [6]. The microstructure development of semiconductors and the know-how of the microchip production industry enabled the application of integrated circuits within the detector itself, thus providing extremely small and effective detectors. Key persons in this development were V. Golovin [7] and Z. Sadygov [8]. Nowadays, SiPMs are produced by the standard Metal-Oxide-Silicon (MOS) process which is relatively simple and cheap [9]. SiPMs have only been commercially available since 2005 [10]. Although their application is not yet as large established as for photomultiplier tubes (PMTs), there are already experiments using SiPMs for instance GERDA Phase 2, the FACT telescope or the MEG experiment.

The nEXO experiment has certain requirements to the photodetectors for example a sensitivity of at least 15 % to VUV-light and a low correlated noise. Possible candidates have to be characterised. Within the scope of this work, a SiPM from FBK has been investigated with respect to the requirements of the nEXO experiment and an absolute calibration of the reference detector – a PMT from Hamamatsu K.K. – has been performed. An overview of the physical basics of the $0\nu\beta\beta$-decay is followed by a general description of the nEXO experiment as well as an introduction to the functionality of SiPMs and PMTs in chapt. 1. In chapt. 2, the basic concept of the absolute calibration of a PMT is described along with the used setup and analysis methods. The results are presented and discussed. Chapt. 3 and chapt. 4 cover the characterisation of the used SiPM. This includes measurements in the absence of light with which fundamental parameters such as gain, breakdown voltage, darkcount rate, afterpulsing and optical crosstalk can be determined as well as measurements with xenon scintillation light for the determination of the PDE. The work is concluded by a summary and ideas for further developments of the used setup and analysis routine.

Chapter 1

Physical Basics

For a better understanding for the measurements carried out in this work, some physical basics are explained in this chapter. This includes the theoretic principle of the $0\nu\beta\beta$-decay with its underlying mechanisms, the physical implications and an experimental approach as well as one possible realisation consisting in the nEXO experiment. A description of the structure, working principle and characteristics of the light detectors investigated in this work – SiPMs and PMTs – is given.

1.1 Neutrinoless Double Beta Decay

The neutrino has always been a bizarre particle. Not only is it extremely hard to detect, it has also provided insight in physics beyond the Standard Model (SM) that is to say neutrino oscillations. Neutrino oscillations demonstrated that neutrinos – which is forbidden in the SM – indeed have mass. This is a necessary precondition for an exceptional mechanism called the $0\nu\beta\beta$-decay.

For a better understanding and as a physical motivation, the main principles of the double beta decay ($2\nu\beta\beta$-decay) are explained in this section. On this basis, the hypothetical $0\nu\beta\beta$-decay is described together with the physical implications in case such a decay is observed. Finally, the experimental requirements for the search for the $0\nu\beta\beta$-decay are described already indicating possible realisations.

1.1.1 Double Beta Decay

During the single beta decay, a neutron of a nucleus decays into a proton under the emission of an electron and an electron antineutrino. The atomic number increases by 1 whereas the mass number stays the same. This is shown schematically in fig. 1.1. The binding energy of the final nucleus is lower than the initial one, so energy is released. There are some nuclides for which the single beta decay is not possible. In fig. 1.2, the level diagram is shown for this scenario. The final nucleus has a larger binding energy than the initial one. Without external energy input, a transition is impossible. A decay in a state with an increase of the atomic number by 2 would be energetically possible. This is called the $2\nu\beta\beta$-decay. Two neutrons of the same nucleus each decay at the same time into a proton, an electron and an electron antineutrino [11]:

$$(Z, A) \rightarrow (Z + 2, A) + 2\mathrm{e}^- + 2\overline{\nu}_\mathrm{e}\,, \tag{1.1}$$

where Z is the atomic number, A the mass number, e^- the electron and $\overline{\nu}_\mathrm{e}$ the electron antineutrino. The corresponding Feynman diagram is shown in fig. 1.3. Two electrons and two electron antineutrinos are produced. The energy spectrum is shown in fig. 1.5 where on the x-axis, the summed energy E of both electrons is normalised to the Q-value which is the total energy of the decay. It results in a continuous shape because of the production of two antineutrinos.

The $2\nu\beta\beta$-decay was first considered by M. Goeppert-Mayer in 1935 [12]. The first actual measurement was performed by M. G. Inghram and J. H. Reynolds in 1950 [13]. They used a chemical method measuring the decay of ^{130}Te to ^{130}Xe indirectly. The first direct observation was only in 1987 by S. R. Elliott, A. A. Hahn and M. K. Moe [14]. They measured the decay of ^{82}Se decaying into ^{82}Kr. There are only 35 nuclides capable of doing the $2\nu\beta\beta$-decay [15]. In many experiments such as EXO-200, NEMO and CUORICINO this decay has already been measured for different nuclides. The $2\nu\beta\beta$-decay is the rarest decay ever detected [15]. The measured half-lifes lie in the order of magnitudes of $T_{1/2} \approx (10^{18} - 10^{21})\,\mathrm{yr}$ [15].

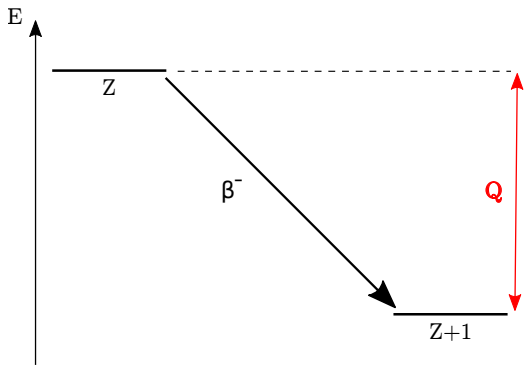

Figure 1.1: Schematic level diagram of the single beta decay. Energy is released with the decay as the final state is stronger bound than the intial one. Adapted from [16].

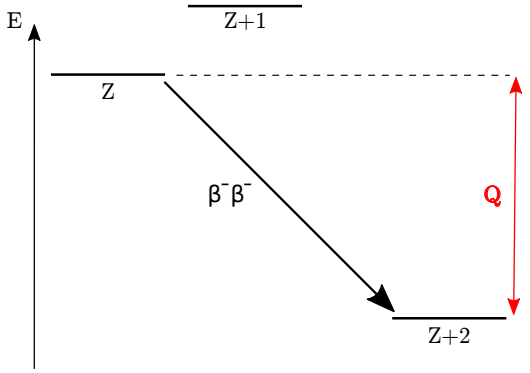

Figure 1.2: Schematic level diagram of the $2\nu\beta\beta$-decay. The single beta decay is not possible, since the final nucleus would be less bound compared to the initial one. But the final state of the $2\nu\beta\beta$-decay is stronger bound, so this decay is possible. Adapted from [16].

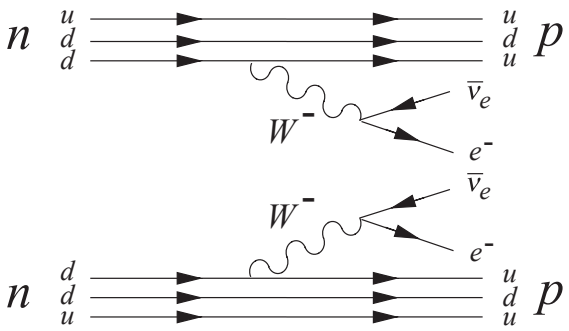

Figure 1.3: Feynman diagram of the $2\nu\beta\beta$-decay. Two neutrons of one nucleus decay at the same time into two protons under the emission of two electrons and two electron antineutrinos. Reprinted from [11].

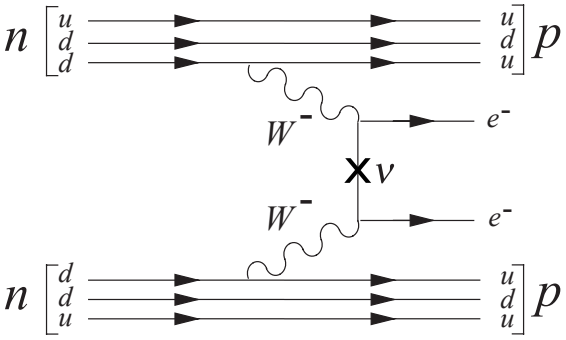

Figure 1.4: Feynman diagram of the $0\nu\beta\beta$-decay. Two neutrons of one nucleus decay at the same time into two protons under the emission of two electrons and no electron antineutrinos. Reprinted from [11].

1.1.2 Neutrinoless Double Beta Decay

Originating from the $2\nu\beta\beta$-decay, one can consider another decay, the so-called $0\nu\beta\beta$-decay. It is a hypothetical decay first proposed by W. H. Furry in 1939 picking up the idea that the neutrino may be its own antiparticle [4]. This possibility was first considered by E. Majorana in 1937 [3]. The search for the $0\nu\beta\beta$-decay is a practical tool to test this theory. The decay is the following [11]:

$$(Z, A) \rightarrow (Z + 2, A) + 2\mathrm{e}^{-} \,. \tag{1.2}$$

Compared to eq. 1.1 for the $2\nu\beta\beta$-decay, only the two electron antineutrinos are missing. The underlying process is the same. One possible mechanism is shown in the Feynman diagram in fig. 1.4. Two conditions must be fulfilled that such a decay can occur. Firstly, neutrinos must not be massless. Due to the observation of neutrino oscillations, it is known that neutrinos possess a

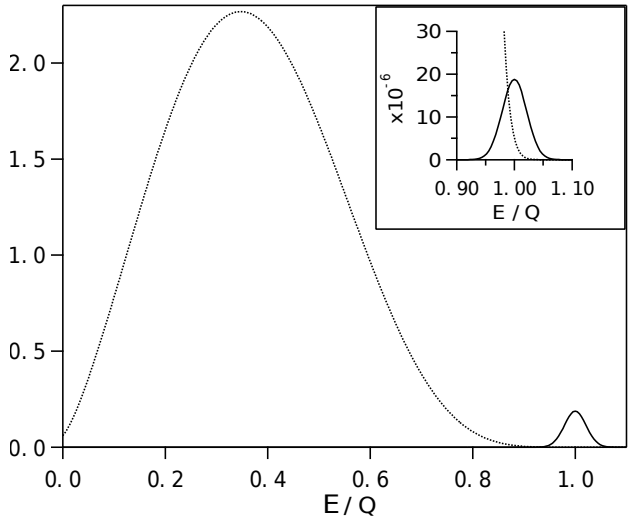

Figure 1.5: Number of events over the summed energy of both electrons normalised to the Q-value. The signal of the $2\nu\beta\beta$-decay as well as the one of the $0\nu\beta\beta$-decay are depicted. A zoom into the $0\nu\beta\beta$-decay-signal reveals the true scaling compared to the one of the $2\nu\beta\beta$-decay as well as an overlap of both spectra. Reprinted from [18].

non-zero rest mass. This allows a helicity flip from a right-handed antineutrino to a left-handed antineutrino. This happens at the "x" in the Feynman diagram. Secondly, the neutrino must be its own antiparticle. The observation of the $0\nu\beta\beta$-decay immediately implies that the neutrino is a Majorana particle [17].

In fig. 1.5, the energy spectrum of the $0\nu\beta\beta$-decay is shown as well. The continuous shape comes from the $2\nu\beta\beta$-decay. In contrast to that, the small peak at the Q-value is the signal one would expect originating from the $0\nu\beta\beta$-decay. Since there are no neutrinos produced, the total energy of the decay is transferred to the two electrons. The most feasible way to search for the $0\nu\beta\beta$-decay is to look at the endpoint of the $2\nu\beta\beta$-decay spectrum.

1.1.3 Physical Implications

Measuring the $0\nu\beta\beta$-decay immediately implies certain physical consequences. Firstly, it proves one more time that neutrinos are not massless. Secondly, it gives evidence of the total lepton number violation. Thirdly, the PMNS mixing matrix for neutrino oscillations changes. Currently, the PMNS is calculated under the assumption that neutrinos are not their own antiparticles. Such a particle is also called Dirac particle. With the observation of the $0\nu\beta\beta$-decay, at least two additional majorana phases α_1, α_2 must be added and the PMNS changes to [19]:

$$U_{\mathrm{PMNS}}^{\mathrm{Majorana}} = U_{\mathrm{PMNS}}^{\mathrm{Dirac}} \begin{pmatrix} 1 & 0 & 0 \\ 0 & e^{i\frac{\alpha_1}{2}} & 0 \\ 0 & 0 & e^{i\frac{\alpha_2}{2}} \end{pmatrix}, \tag{1.3}$$

where $U_{\mathrm{PMNS}}^{\mathrm{Majorana}}$ is the mixing matrix for the Majorana and $U_{\mathrm{PMNS}}^{\mathrm{Dirac}}$ for the Dirac case.

And fourthly, which is the main consequence, the observation of the $0\nu\beta\beta$-decay would prove the Majorana nature of the neutrino meaning that the neutrino is its own antiparticle. This would be further physics beyond the SM.

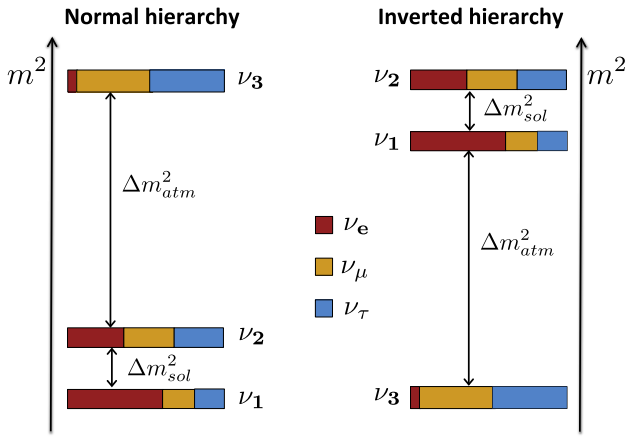

Figure 1.6: NH and IH of the neutrinos. ν_1, ν_2, ν_3 are the mass eigenstates of the neutrinos. The colour indicates the flavour composition of the different mass eigenstates. The y-axis shows the mass square differences of the several mass eigenstates. Reprinted from [20].

With the detection of the $0\nu\beta\beta$-decay, it may be possible to determine the absolute neutrino mass hierarchy. Measurements of neutrino oscillations are only sensitive to the mass square differences of the mass eigenstates. An exception is the sign of $\Delta m^2_{12} \equiv \Delta m^2_2 - \Delta m^2_1$, which is known from measurements of solar neutrinos. The signs of the other mass square differences are unknown. This results in two possibilities of mass ordering shown in fig. 1.6. The y-axis indicates the mass square of the single states and ν_1, ν_2 and ν_3 are the different mass eigenstates of the neutrinos. The flavour composition of each mass eigenstate is displayed by different colours. Either m^2_3 is larger than m^2_2, then the so-called normal hierarchy (NH) is valid. In case m^2_3 is lighter than m^2_2, the inverted hierarchy (IH) is correct. By detecting the $0\nu\beta\beta$-decay, there are stronger constraints on the real hierarchy.

1.1.4 Requirements for an Experiment

Experiments for searching the $0\nu\beta\beta$-decay require certain experimental demands. The actual goal is to determine the half-life $T^{0\nu}_{1/2}$ of the $0\nu\beta\beta$-decay. It can be calculated via [21]:

$$\left(T^{0\nu}_{1/2}\right)^{-1} = G^{0\nu}(Q, Z) \cdot \left|M^{0\nu}\right|^2 \cdot \frac{m^2_{\beta\beta}}{m^2_{\mathrm{e}}}\,, \tag{1.4}$$

where $G^{0\nu}$ is a phase-space factor depending on the Q-value and the atomic number, $M^{0\nu}$ is the nuclear matrix element depending on the nuclide, m_{e} is the electron mass and $m_{\beta\beta}$ is the so-called effective neutrino Majorana mass which can be calculated as follows [15]:

$$m_{\beta\beta} = \left|\sum_{i=1}^{3} m_i \cdot \left(U^{\mathrm{Majorana}}_{\mathrm{e},i}\right)^2\right|\,. \tag{1.5}$$

$U^{\mathrm{Majorana}}_{\mathrm{e},i}$ are the single components of the modified PMNS for the Majorana case for the electron flavour. $m_{\beta\beta}$ is a good quantity to compare different experiments concerning their sensitivity, because it is independent on the nuclide. Figure 1.7 shows the probability bands of $m_{\beta\beta}$ versus the lightest neutrino mass m_{min} which is different depending on the hierarchy. For the NH, m_1

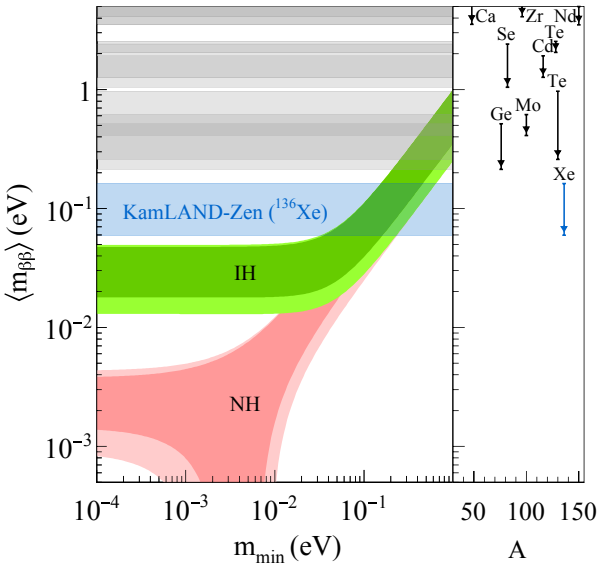

Figure 1.7: $m_{\beta\beta}$ depending on m_{min} with the presently best lower limit on $m_{\beta\beta}$ in blue. Coloured dark shaded are the predictions based on the best-fit values of neutrino oscillations for the IH (green) and the NH (red). The light shaded regions represent the $3\,\sigma$ ranges calculated from the oscillation parameter uncertainties. For comparison, the lower limits for other nuclides are shown at the right side. Adapted from [22].

is the lightest mass, in case of the IH, it is m_3. The light shaded regions correspond to the $3\,\sigma$ ranges which have been calculated from the oscillation parameter uncertainties whereas the dark shaded regions denote the best-fit values of the neutrino oscillations. Currently excluded are the regions for $m_{\beta\beta} > 60\,\text{meV}$ by $0\nu\beta\beta$-decay experiments [22] with 90 % CL. Improving the sensitivity on $m_{\beta\beta}$ implies large-scale detectors and long exposure times. The sensitivity η on $m_{\beta\beta}$ can be calculated as follows according to [21]:

$$\eta = K_2 \cdot \sqrt{\frac{1}{\epsilon \cdot G^{0\nu}(Q,Z) \cdot |M^{0\nu}|^2}} \cdot \left(\frac{c \cdot \Delta E}{M_{\beta\beta} \cdot t} \right)^{1/4} , \tag{1.6}$$

which is proportional to several parameters. K_2 is a constant, ϵ represents the signal detection effiency, $G^{0\nu}(Q,Z)$ the phase space factor of the $0\nu\beta\beta$-decay, $|M^{0\nu}|$ the nuclear matrix element, c the background rate, ΔE the energy resolution, $M_{\beta\beta}$ the used mass of the $\beta\beta$ decaying nuclide and t the exposure time. For a lower $m_{\beta\beta}$, these parameters should be chosen so that η is decreased. Some parameters, such as ϵ, $G^{0\nu}(Q,Z)$ and $|M^{0\nu}|$, contribute with the square root, whereas c, ΔE, $M_{\beta\beta}$ and t come with the forth root. Parameters contributing with the square root have more impact on η than the ones contributing with the forth root. $G^{0\nu}(Q,Z)$ and $|M^{0\nu}|$ depend on the nuclide. They should be as large as possible [21]. A suitable choice of the nuclide is more relevant for improving η than the setup parameters as for example M and t. Favoured elements regarding the product of $G^{0\nu}(Q,Z)$ and $|M^{0\nu}|$ are for example ^{82}Se, ^{130}Te and ^{150}Nd.

Another important parameter is the background rate which needs to be as low as possible. There are several contributions to background. One is cosmic radiation, mostly muons doing neutron activation in the surrounding material of the detector. For the reduction of this background component, most laboratories are built underground. Additional muon vetos can exclude signals

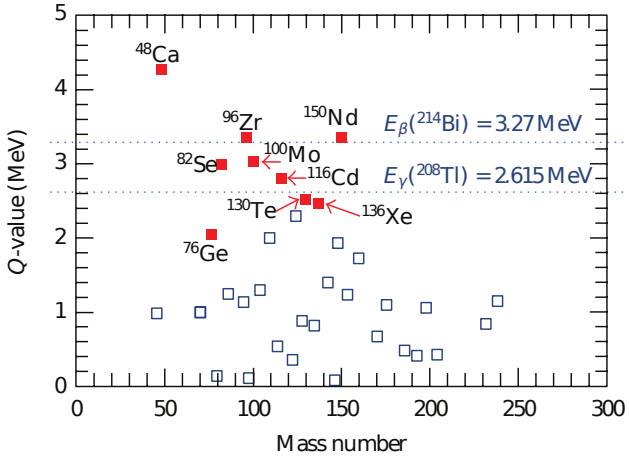

Figure 1.8: Q-value of different nuclides. The dottet lines refer to the highest decay energies of γ-transitions and β-decays. Favoured are nuclides above most background. The nine most suitable candidates are highlighted in red. Reprinted from [21].

originating from muons. The second factor is radiation from external sources as rock. Different shieldings surround the detector and reduce the radiation. A third component is radiation from the detector and the shieldings itself. To minimise this effect, only highly radiopure materials are used as well as purification processes during the experiment.

A further requirement for an experiment is a good energy resolution. The expected signal of the $0\nu\beta\beta$-decay would be a δ-peak at the Q-value, but due to the finite energy resolution, the peak is smeared. A zoom on the endpoint spectrum is depicted in the upper right corner of fig. 1.5. It indicates two problems. Firstly, the signal expected from the $0\nu\beta\beta$-decay is less than seven orders of magnitudes smaller than the one of the $2\nu\beta\beta$-decay. Secondly, both signals overlap each other. Due to these limitations, a good energy resolution is required to improve the ratio of $0\nu\beta\beta$-decay and $2\nu\beta\beta$-decay events. $0\nu\beta\beta$-decay candidates with a slow $2\nu\beta\beta$-decay rate (long half-life) as for example ^{136}Xe are preferred [21].

From the experimental point of view, the following three factors are the most stringent for the design of an experiment. The first one is the Q-value of the $0\nu\beta\beta$-decay nuclide. It is probably the most relevant one since it has impact on the phase space as well as on the background. Despite all the arrangements in order to reduce the background, there are always natural decays. This includes several γ-transitions as well as β-decays with certain decay energies. Both impose an irreducible background up to 3.27 MeV [21]. In fig. 1.8, the dependence of the Q-value on the mass number is displayed for the 35 candidates capable of doing the $2\nu\beta\beta$-decay. The dottet lines indicate the maximum energies of the background processes. For the γ-transitions, the ^{208}Tl peak at 2.615 MeV is most dominant, whereas the background due to the β-decay is present up to 3.27 MeV. Nuclides with a Q-value as high as possible are required. The nine most favourable candidates concerning the Q-value are highlighted in red [19, 21]. Good candidates are for example ^{48}Ca, ^{96}Zr and ^{150}Nd, because their Q-value lies above most background.

Another criterion is the natural abundance together with the enrichment. For a low η, large-scale detectors are needed. This requires a high natural abundance or an easy enrichment. For most candidates, the natural abundance lies in the range of some percent [21]. Together with the cost and efficiency, the enrichment is easier for some elements than for others. This is the case

for ^{136}Xe. In contrast to that, the three nuclides most favoured by the Q-value are very hard to enrich [21].

Many detectors use the $2\nu\beta\beta$-decay material as source material for the signal and at the same time as detection material. This simplifies the use of large nuclide masses. Furthermore, it increases the energy resolution significantly. But not all nuclides are compatible with an appropriate detection technique. Desired candidates are high purity semiconductor crystals as for example ^{76}Ge used in GERDA or noble gasses like ^{136}Xe implemented in EXO-200 [15, 18, 21].

1.2 The nEXO Experiment

In the past 70 years, there have been many experiments searching for the $2\nu\beta\beta$-decay as well as for the $0\nu\beta\beta$-decay. While the $0\nu\beta\beta$-decay has not been detected so far, the $2\nu\beta\beta$-decay has been measured in a wide range of experiments. One of those is the EXO-200 experiment. It is one of the pioneering experiments using a liquid noble gas, in particular ^{136}Xe. EXO-200 discovered the $2\nu\beta\beta$-decay of ^{136}Xe in 2011. Based on the work of EXO-200, nEXO will be a future experiment to investigate the $0\nu\beta\beta$-decay.

In the following, a short overview of the nEXO experiment itself and the current baseline concepts are given. In addition to that, the detection principle is described and the goals of the nEXO experiment are underlined.

1.2.1 Overview

Not all the requirements for an experiment mentioned earlier can be met simultaneously. One has always to favour certain aspects with respect to others trying to achieve the best sensitivity to $T^{0\nu}_{1/2}$ and $m_{\beta\beta}$. The current best limit for $m_{\beta\beta}$ is (60–161) meV achieved by the KamLAND-Zen experiment [22]. In order to extend the sensitivity to the entire IH region, innovative ideas and techniques have to be applied. One of the next generation experiments is the nEXO experiment which is in the pre-R&D-phase. It will be an ultralow background ton scale experiment presumably located in SNOLAB at a depth of about 2 km corresponding to 6 000 mw.e. [23, 24]. SNOLAB is one of the deepest clean room facilities in the world thus providing excellent shielding from cosmic radiation and extremely low background rates and is situated near Sudbury, Ontario in Canada [23]. The nEXO experiment will use an entire xenon mass of about 5 t enriched to about 90 % in ^{136}Xe [24, 25]. It is planned to reach a resolution of $\sigma/E \leq 1\,\%$ at the Q-value at 2.458 MeV [26] and a sensitivity to $m_{\beta\beta}$ of about (5.7–17.7) meV [25].

1.2.2 Baseline Concepts

A conceptual sketch of the nEXO experiment is shown in fig. 1.9. The baseline concept and the dimensions are taken from [25, 27] and are preliminary. According to this concept, the detector is surrounded by several layers. At the outermost, there is a water tank with 10 m diameter and 9 m height. It serves as neutron shielding and as an active muon veto. Integrated PMTs measure the Cherenkov light from muons. The next layer is an insulation vacuum to minimise the heat input from outside. Inside, a tank with liquid HFE used as cooling agent is placed. It also contains the actual detector. For the nEXO experiment, it is planned to use a single sided single phase time projection chamber (TPC). A schematic design is shown in fig. 1.10. The TPC has a cylindrical shape with 130 cm diameter and 130 cm height. It is supposed to be hanging down into the HFE

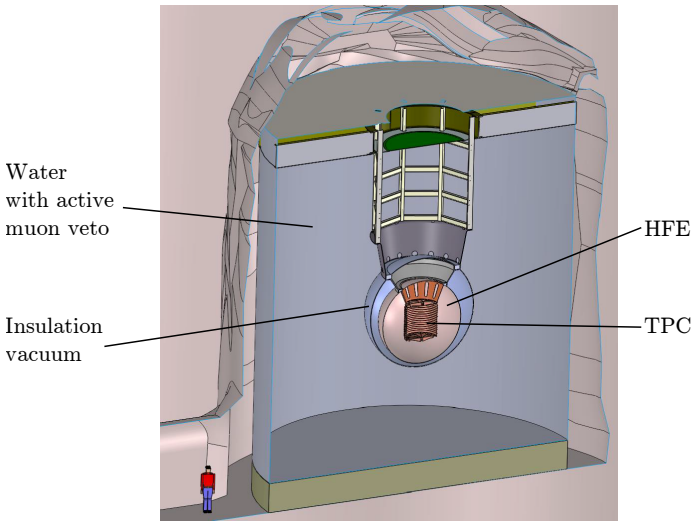

Figure 1.9: Engineering design of the planned setup for the nEXO experiment. The actual detector is formed by a TPC filled with LXe. It is surrounded by a cooling fluid and an insulation vaccum. Both are enclosed by a huge water tank. Reprinted from [27].

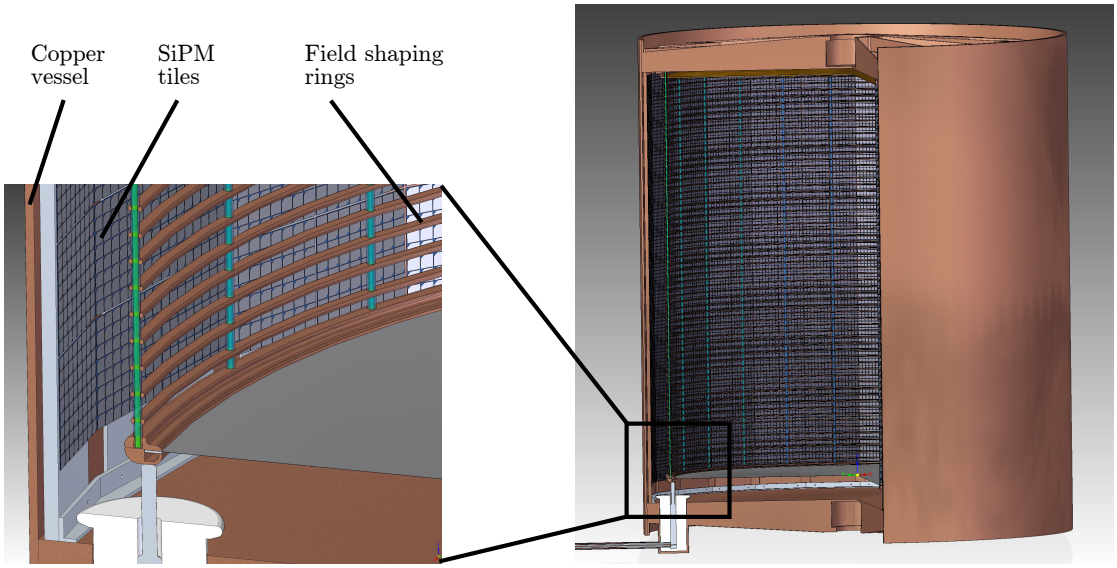

Figure 1.10: Schematic view of the TPC for the nEXO experiment. The left picture shows the bottom edge of the TPC. At the back, the SiPM tiles are visible. In front, the field shaping rings are placed. The right picture depicts a section view of the entire TPC. Reprinted from [27].

as illustrated in fig. 1.9. The TPC is filled with LXe. Its huge volume provides an extremely high self-shielding. It is planned to use a drift field of 400 V/cm. Field shaping rings surround the inner volume to improve the electric drift field. The anode consists of so-called charge readout tiles. Each tile includes x- and y-chains of pads which are arranged similar to a chequer board. They contain 30×30 channels with 3 mm strip pitch and isolated intersections. Their purpose is to collect the electrons of a signal (charge readout). For the light detection (light readout), it is planned to use SiPMs (see sec. 1.3). They detect the VUV scintillation light of LXe at 178 nm. The entire inner surface is covered with SiPMs. 8×8 detectors are combined to tiles, 30 tiles to a ladder stave. All in all, 24 staves are arranged in a cylindrical shape which gives a total sensitive photodector area of about $4\,\mathrm{m}^2$. As the whole TPC is cooled, the entire electronic including the photodetectors is operated at cryogenic temperatures.

1.2.3 Detection Principle

When a $0\nu\beta\beta$-decay occurs in the detector, the outgoing electrons produce two different signal components. On the one hand, the electrons ionise the xenon atoms which generates an electron cloud. On the other hand, scintillation light in the VUV range is generated after the excitation of xenon atoms by the electrons. Both the ionisation electrons as well as the scintillation photons are detected. This enables a 3D reconstruction of the event in the detector. The scintillation photons reach the SiPMs almost instantaneously. Their arrival time is noted as the time stamp t_{light}. The electron cloud is drifted in the electric field towards the anode where the electrons are collected. Due to the pad structure, the xy-position of the electron cloud on the anode can be resolved. The arrival time is denoted as t_{charge}. Together with t_{light}, the position z of the initial event can be reconstructed via the formula:

$$t_{\mathrm{charge}} - t_{\mathrm{light}} = \frac{z}{v_{\mathrm{Drift}}}\,, \tag{1.7}$$

in which v_{Drift} denotes the constant drift velocity in LXe. For the scintillation and ionisation signal, not only the time and position, but also the individual energy is measured. This enables the reconstruction of the total energy deposition of the event.

1.2.4 Goals

The main goal of the nEXO experiment is to answer the fundamental question whether the neutrino is its own antiparticle. An energy resolution of lower than 1 % at the Q-value is aimed at. It is estimated to reach a sensitivity to $m_{\beta\beta}$ of about (5.7–17.7) meV [25]. The 90 % CL exclusion sensitivity to $m_{\beta\beta}$ versus the lightest neutrino mass m_{min} for the NH (left) and the IH (right) is depicted in fig. 1.11 The width of the horizontal bands results from the uncertainty of the nuclear matrix elements. The dashed bands for the hierarchies is due to the unknown Majorana phases whereas the solid lines originate from the 90 % CL errors of the 3-flavour neutrino fit of reference. After running nEXO for 10 yr, it is expected to cover almost the entire IH region. This corresponds to a lower limit of half-life for LXe of $T^{0\nu}_{1/2} \approx 9.2 \times 10^{27}$ yr with a 90 % CL exclusion sensitivity. It is predicted to achieve a background rate of $2.9 \times 10^{-4}\,\mathrm{cts\,FWHM^{-1}kg^{-1}\,yr^{-1}}$ in the inner 2 000 kg of LXe [25].

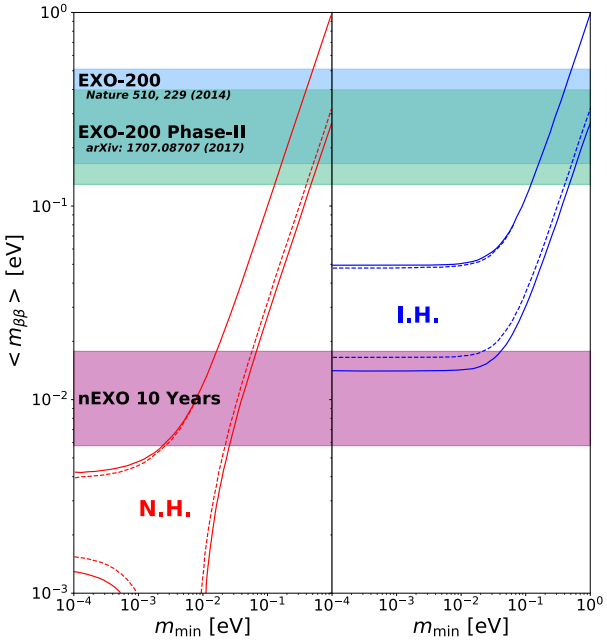

Figure 1.11: $m_{\beta\beta}$ depending on the minimum neutrino mass for both hierarchies. The coloured bands compare the sensitivity bands of the predecessor experiment – EXO-200 – with the expected sensitivity of the nEXO experiment running for 10 yr. nEXO will cover most of the IH. Reprinted from [25].

1.3 Silicon Photomultiplier

In the nEXO experiment, SiPMs will be used for the light detection. SiPMs are semiconductor photodetectors which consist of many single pixels connected in parallel on a common silicon substrate. Each pixel consists of a photodiode. A reverse bias voltage (U_{bias}) is applied to every single pixel. As soon as the breakdown voltage (U_{break}) is reached, a current can flow even in the reverse direction. A SiPM is operated 10 % to 20 % above U_{break}. This is called Geiger mode. The term is derived from the Geiger-Müller counter referring to the self-reinforcing multiplication process of the electrons. This enables the detection of single photons with a SiPM.

In this section, the basic structure and working principle of SiPMs is described. An overview of several geometric and electrical properties of a SiPM is given. Various noise contributions such as darkcount rate (DCR), afterpulsing (AP) and optical crosstalk (CT) are explained as well as the photon detection efficiency (PDE). The requirements on SiPMs for the nEXO experiments are presented and discussed.

1.3.1 Setup

A schematic view and cross section of a SiPM is visible in fig. 1.12. The base material is formed by the substrate body. At the top, many single pixels are integrated. They are mechanically separated by gaps filled with a highly photon-absorbing material, the so-called trenches. This will become important in sec. 1.3.4.3. Integrated conduction paths are running at the top of the detector providing each pixel with U_{bias}. Every pixel is connected in series with a quenching resistor (see

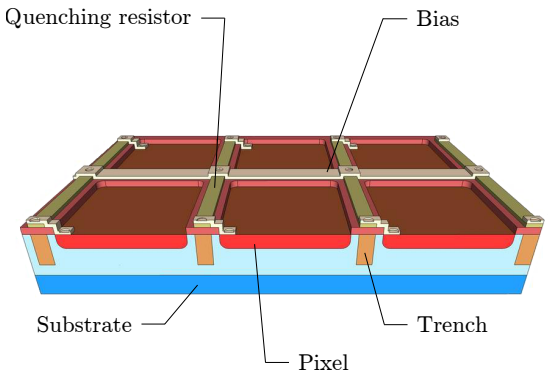

Figure 1.12: Cross section of the pixel structure of a SiPM. Each pixel is provided by U_{bias} and has its own quenching resistor. The bottom is formed by the low doped substrate. Adapted from [28].

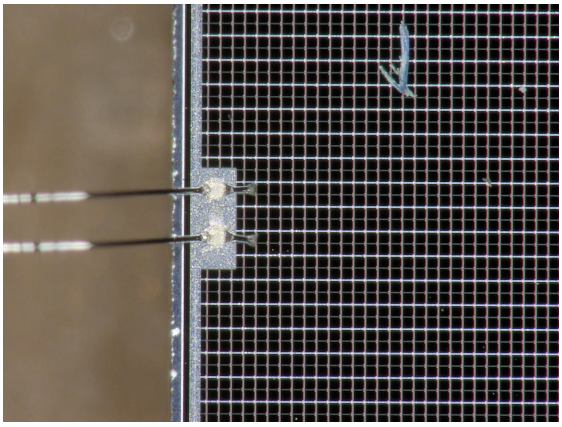

Figure 1.13: Detail of a SiPM with its pixel structure as well as quenching resistors and conduction paths for U_{bias}. The supply voltage including the output signal is applied and tapped, respectively, by wire bonds which are visible at the left.

sec. 1.3.2). A top view of a SiPM used in this thesis can be seen in fig. 1.13. It shows the pixel structure as well as the bias paths and the quenching resistors.

An exemplary cross section of a single pixel is shown in fig. 1.14. It is formed by a n-p-i-p-diode. The different layers are generated by different doping levels and doping depths of the same bulk material. Doping denotes the systematic insertion of impurity atoms in the intrinsic (non-doped) substrate. There are two different types of doping. The first one is the n-doping. A foreign atom with a higher number of valence electrons than m is inserted into an element grid with m valence electrons. The additional electrons are bound less than the other ones. P-doping means an atom with a lower number of valence electrons is brought into the intrinsic material. This results in the situation that electrons "are missing" in the grid and further electrons are captured easily [29, 30]. When a n- and a p-doped layer are brought together, a pn-junction is created. Electrons from the n-layer diffuse to the p-layer recombining with the holes. The n-layer becomes positve charged and the p-layer negative. This mechanism leads to the formation of a depletion zone within the junction. Between the two layers, a constant diffusion voltage (U_{diff}) is formed. When a voltage is applied to the pn-junction, there are two possibilities. The first one is forward bias meaning that the external voltage points in the opposite direction as U_{diff}. This is the principle of a LED. For semiconductor photodectors, a reverse bias is applied increasing the depletion layer. This reduces the thermal noise.

A SiPM is processed on a silicon wafer which is about 200 nm to 300 nm thick. It forms the common substrate body [9, 32] and consists of very low doped silicon of either p- or n-type. In fig. 1.14, it is a p-type layer. The low doping with a charge carrier concentration of $n \approx 10^{12}\,\text{cm}^{-3}$ [29] is indicated by the minus. On top, the avalanche zone is placed. Its charge carrier concentration is higher than the substrate with $n = (10^{13}\text{–}10^{17})\,\text{cm}^{-3}$ [29]. The top of a pixel is formed by the entrance window consisting of a highly doped layer of the opposite doping type compared to the substrate. In this case, a n^+ doping is used. The plus indicates a high doping. The entrance window is about 0.4 µm thin [9, 33] and highly positively charged. Together with the p-layer, it forms the pn-junction where the multiplication occurs. On top, there is a SiO_2 layer of approximately

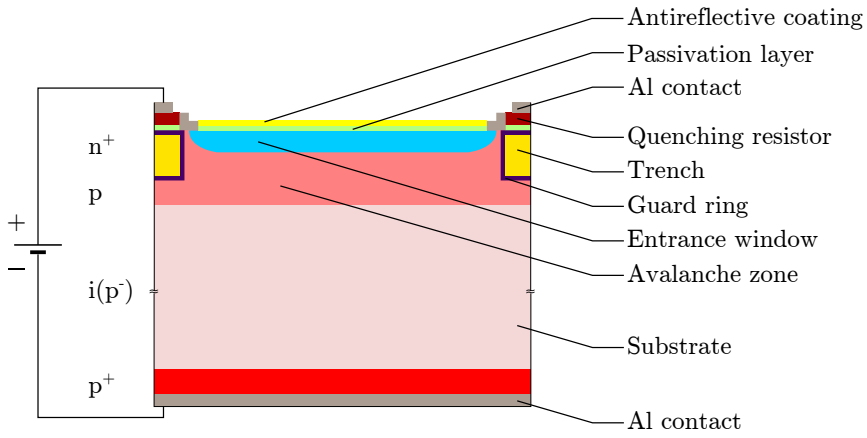

Figure 1.14: Schematic cross section of one pixel in the static case. The different doping layers are shown. Between both sides of the pixel, a reverse U_{bias} is applied. Adapted from [10, 31].

200 nm thickness to neutralise the electrons from the resulting open bonds at the surface of the entrance window [10]. This is the passivation layer. Most SiPMs are covered with an additional antireflective coating. It is about 30 nm thick [33] and minimises reflections at the surface of the pixel due to the strong discrepancy of the refractive indices of silicon and air. At the bottom of the wafer, a highly doped layer of the same type as the substrate – in this case p^+ – is placed. Along with the entrance window both layers serve as electrodes of the pixel and are connected to the external U_{bias} and the quenching resistor via e.g. aluminium contacts. The pixel structure shown in fig. 1.14 is for a p-i-p-n diode. All p-layers can be replaced by n-ones and vice versa. The single pixels are not only mechanically separated by the trenches, but also electrically by guard rings in order to reduce leakage currents and high field regions at the surface of the pixels. They are made of a conducting material and avoid peripheral avalanche breakdown [10, 31, 34].

1.3.2 Working Principle

The main working principle will be explained on the basis of fig. 1.15. An incoming photon with energy $E_{\text{ph}} = h\nu$ is absorbed in the intrinsic layer. For the relevant photon energies in the range of few electronvolts, the internal photoeffect is the dominant interaction process. The excess energy of the photon is converted into the kinetic energy of the electron-hole pair. As the electron is generated by an incoming photon, it is also called photoelectron. Due to the external electric field, electron and hole are drifted in opposite directions. When one of the charge carriers reaches the pn^+-region, the so-called avalanche breakdown is initiated. Both types of charge carriers (electron and hole) acquire enough energy between two scattering events in the electric field to trigger multiplication processes [30]. For reason of transparency, only the multiplication of the electrons is drawn in fig. 1.15. Multiplication occurs when the charge carriers obtain enough energy to generate further electron-hole pairs in subsequent collisions. An avalanche develops. With the operation of the pixel in Geiger mode, the number of produced secondary electrons is no longer proportional to the number of photoelectrons. Regardless of the number of incident photons or produced photoelectrons in the pixel, the same amount of secondary electrons is generated. It cannot be distinguished whether one or more photons impinged onto the pixel. The advantage is that the multiplication is so large that single photons can be detected. The number of generated

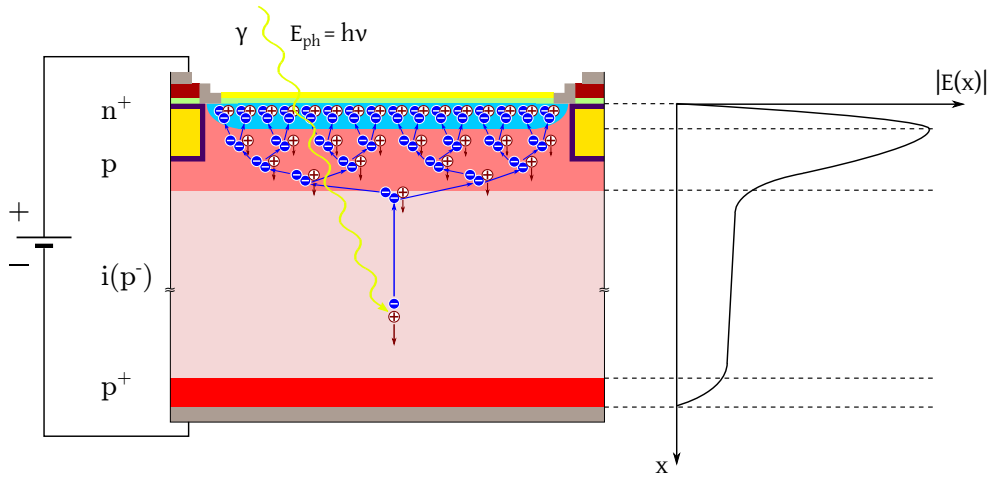

Figure 1.15: Schematic cross section and electric field of one pixel during an avalanche. A photon is aborbed and creates an electron-hole pair which is drifted towards the multiplication region. The electric field is so large that secondary electron-hole pairs are generated. Adapted from [10, 31].

electron-hole pairs increases exponentially during the avalanche breakdown. This is a self-sustaining process. In order to restore the sensitivity to further incoming photons, the avalanche has to be interrupted. The most common technique is to use passive quenching. This is for example realised by a high-omic resistor in series with the pixel. The working principle and the signal formation is explained in the following according to the model developed by R. H. Haitz [6].

In fig. 1.16a, the equivalent circuit of one pixel is shown. It can be described by an internal resistor R_D in case of current flow, a capacity C_D created by the pn-junction, an internal voltage source describing the breakdown voltage U_break and a control switch S indicating the two possible modes of the pixel: ON and OFF. According to [5], R_D origniates from three different contributions: spreading resistance, space charge effects and internal heating. The spreading resistance arises from the pn-junction and is constant for small currents. Space charge effects originate from the dipole-like distribution during an avalanche of mainly electrons at one end of the pixel and holes at the other which changes the resistance. As an avalanche commences, some of the energy is also deposited in form of phonons. This causes internal heating of the avalanche region altering the resistance as well. A more detailed discussion is given in [5, 35].

The state of a pixel before an avalanche occurs at $t = t_0$ can be described by the capacitance C_D in series with the quenching resistor R_D. This corresponds to S in OFF position. At this time $t < t_0$, C_D is fully charged at $U_\mathrm{D} = U_\mathrm{bias} > U_\mathrm{break}$ and no current is flowing through the circuit. The voltage U_Q across R_Q is 0 which is also shown in fig. 1.16b. When an avalanche is initiated in the pixel at $t = t_0$, the new situation can be described by enclosing R_D and U_break. This refers to the switch in ON position. It causes a very short current spike in the pixel with a duration of about 10^{-11} s [6] at a maximum voltage of $I_\mathrm{max} = (U_\mathrm{bias} - U_\mathrm{break})/R_\mathrm{D}$. C_D is discharged exponentially through R_D with a time constant $\tau_\mathrm{dis} = R_\mathrm{D}C_\mathrm{D}$ for $t_0 < t < t_1$. At the same time, the pixel gets conductive and a current I_D starts to flow. This causes a voltage drop of U_D down to U_0 and an increasing voltage U_Q across R_Q up to $U_\mathrm{bias} - U_0$. I_D decreases until it reaches the operating point $I_0 = (U_\mathrm{bias} - U_\mathrm{break})/(R_\mathrm{Q} + R_\mathrm{D})$. According to R. J. McIntyre [5], the quenching of the avalanche is caused with a so-called turn-off probability P_{10} by statistical fluctuations bringing the number

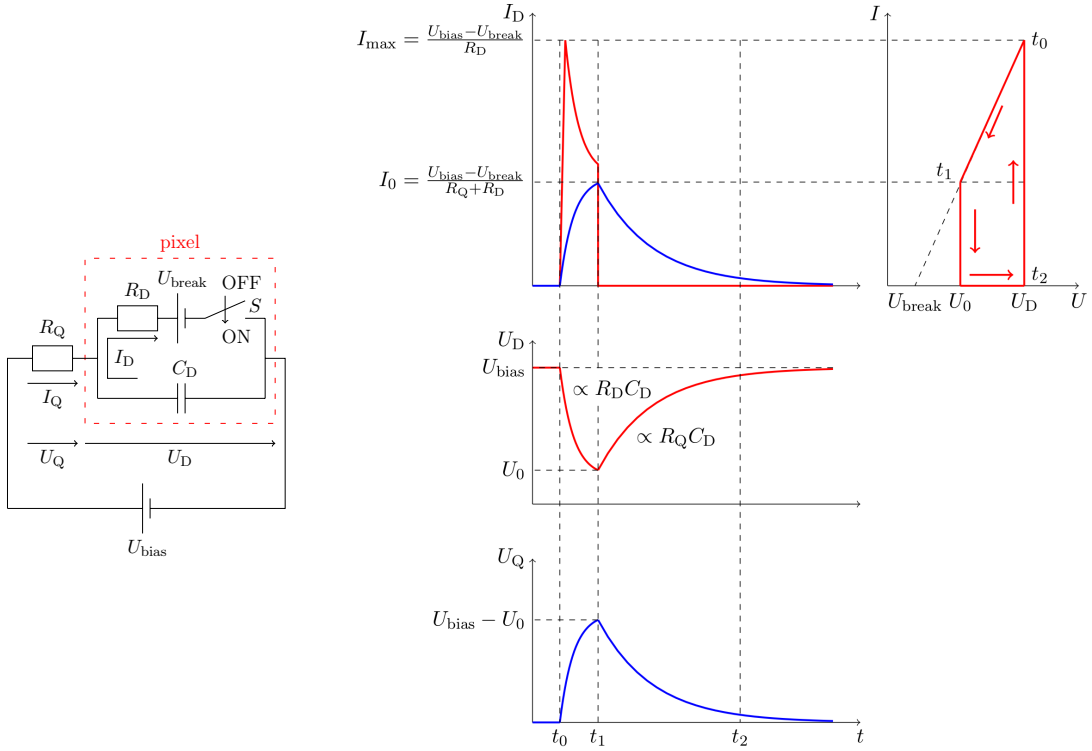

(a) Equivalent circuit of one pixel. **(b)** Current and voltage development in a single pixel.

Figure 1.16: Model for the electrical behaviour of a pixel according to [6]. (a) shows the equivalent circuit of one pixel consisting of a resistor R_D, an internal supply voltage U_{break}, a bistable switch S and a junction capacity C_D. (b) displays the current and voltage behaviour of the pixel and R_Q. Adapted from [6, 33].

of charge carriers in the breakdown region to zero. As from the moment the avalanche is quenched at time $t = t_1$, the current I_D in the pixel drops abruptly to 0. This state is again described by S in OFF position. The capacitance C_D recharges to U_{bias} with a time constant $\tau_R = R_Q C_D$. This happens at $t_1 < t < t_2$ until the pixel has recharged. All pixels are connected in parallel and the output voltage of each pixel is summed up to the final output signal.

1.3.3 Geometric and Electrical Properties

Each SiPM has some geometric and electrical properties differing from detector to detector. They have impact on the behaviour of the SiPM and are described in this section.

Bias voltage:
The external voltage applied to a SiPM is called U_{bias}. It can be positive or negative which depends on the doping profile of the SiPM. A SiPM is typically operated approximately (10–20) % above U_{break} [36]. For a lower U_{bias}, the gain is generally too low and for a higher U_{bias}, noise effects such as CT become too dominant.

Breakdown Voltage:
The breakdown voltage U_{break} is the voltage at which a current can flow in reverse bias mode. But the avalanche must be triggered at first by a free charge carrier in the multiplication region.

Depending on the SiPM type, U_{break} can differ between 20 V and 90 V. This is because several parameters as the size of the pixel or the exact doping profile influence U_{break}.

Overvoltage:
For a better comparison between different SiPM devices, the so-called overvoltage (U_{over}) is used instead of U_{bias}. It is the difference of U_{bias} and U_{break} [37]:

$$U_{\text{over}} = |U_{\text{bias}} - U_{\text{break}}| \ . \tag{1.8}$$

It is an important parameter since nearly all relevant characteristics are specified depending on U_{over}.

Quenching Resistance:
The quenching resistance R_{Q} is a high omic polysilicon resistor operated in series with its corresponding pixel. Its purpose is to quench the avalanche in the pixel avoiding permanent damage and restoring the sensitivity to further incoming light. R_{Q} lies in the range of (100–1000 kΩ [31, 38] depending on the size and thus on the capacity and internal resistance of the pixel. It is determined by the width, the doping and the depletion zone of the pixel. A thicker depletion zone also results in a higher omic resistance demanding a larger value for R_{Q}. With its impact on the signal shape, it strongly influences the dead time as well as the recovery time. This is especially critical for the recovery time. It should be kept as small as possible demanding a small R_{Q}. But it must be still large enough to lower the current so that avalanche can be quenched. An appropriate choice of R_{Q} is essentially for the behaviour of the SiPM.

Internal Capacity:
Each pixel has an internal capacity C_{D}. It depends on both size and width of the depletion zone. The larger the pixel is, the larger is also C_{D}. This relation also applies to the thickness of the pixel. For a constant pixel area, the number of electrons in the pixel increases for a thicker pixel and also C_{D}. This causes the DCR to rise drastically (see sec. 1.3.4.1). It sets a practical limit on the maximal achievable pixel size and also the maximal attainable gain. Typcial values of C_{D} are in the range of some fF [9, 31]. As it is fairly small, its impact on the pulse shape is relatively low compared to R_{Q}.

Dead Time:
In fig. 1.16, the time between t_0 and t_1 is called dead time of the pixel. Further incoming photons are not detected. The reason is that during an avalanche, no further avalanche can be triggered in the same pixel. The dead time lasts typcially only few nanoseconds [9].

Recovery Time:
After the initiation of an avalanche, there is also a recovery time τ_{R} of the pixel. This is the time span between t_1 and t_2. The pixel is not fully recharged yet, but capable of detecting incoming photons. This results in a lower U_{bias} and a lower gain. Signals measured in this time interval are significantly smaller than signals detected at e.g. $t = t_0$.

Pulse Shape:
SiPMs possess a very asymmetric pulse shape. This mainly results from the signal formation explained in the previous section. A schematic sketch of a typical SiPM pulse can be seen in fig. 1.17. A SiPM-pulse has an extremely steep rising edge in the region of several picoseconds [9, 31, 39]. In contrast to that, the falling edge is relatively long with 100 ns to 300 ns [33]. It mainly depends on the value of R_{Q} which influences the duration of τ_{R}. For some devices, there

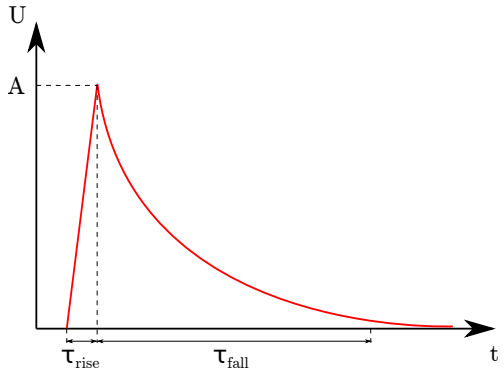

Figure 1.17: Qualitative sketch of a typical SiPM pulse with voltage over time. It has a very short rise time of less than 1 ns reaching its highest voltage value A of the pulse. Then an exponential fallging edge with a duration of about 100 ns to 300 ns follows.

are two time constants describing the falling edge. The first is a relatively fast one presumably produced by a so-called parasitic capacity C_Q of the quenching resistor with values of about some pF, the second a larger one from R_Q [9, 39]. Additional factors of the readout system such as impedance, capacitance and finite bandwidth of amplifier or oscilloscope can have impact on the time constants. The maximum of the pulse is the pulse amplitude A. As all pixels are connected in parallel, A is quantized and increases for an increasing number of triggered pixels.

Gain:
The total number of secondary electrons produced during one avalanche is called gain G. It is the internal amplification factor of the pixel and thus the SiPM. It can be calculated as follows [40]:

$$\mathrm{G} = \frac{C_\mathrm{pixel} \cdot U_\mathrm{over}}{e}\,, \tag{1.9}$$

where $C_\mathrm{pixel} = C_\mathrm{D} + C_\mathrm{Q}$ and e denotes the elementary charge. G is typically about 10^6 [9, 31, 32]. There is a strong dependence of G on U_over. This is because the applied electric field increases with increasing U_over. The charge carriers are stronger accelerated and thus obtain the necessary energy to initiate multiplication processes earlier. Since the size of the avalanche region stays the same, the charge carriers can reach this energy more often. In sum, there are more secondary electrons generated and G increases. According to [41], there is a linear dependence of G to U_over but no dependence on the temperature.

Trigger Probability:
A free electron in the space charge region – for instance generated by an incoming photon – does not necessarily produce a signal in the detector. Only with a certain probability, the electron, the hole or both initiate an avalanche. This is called the trigger probability P_trig. It is a function of the single trigger probabilities of electron and hole. Both probabilities depend on U_over and the position at which the electron-hole pair has been generated. They increase with an increasing U_over, but the trigger probability of an electron is always larger than the one of a hole [42]. P_trig strongly influences other parameters such as crosstalk and photon detection efficiency (see sec. 1.3.4.3 and 1.3.5).

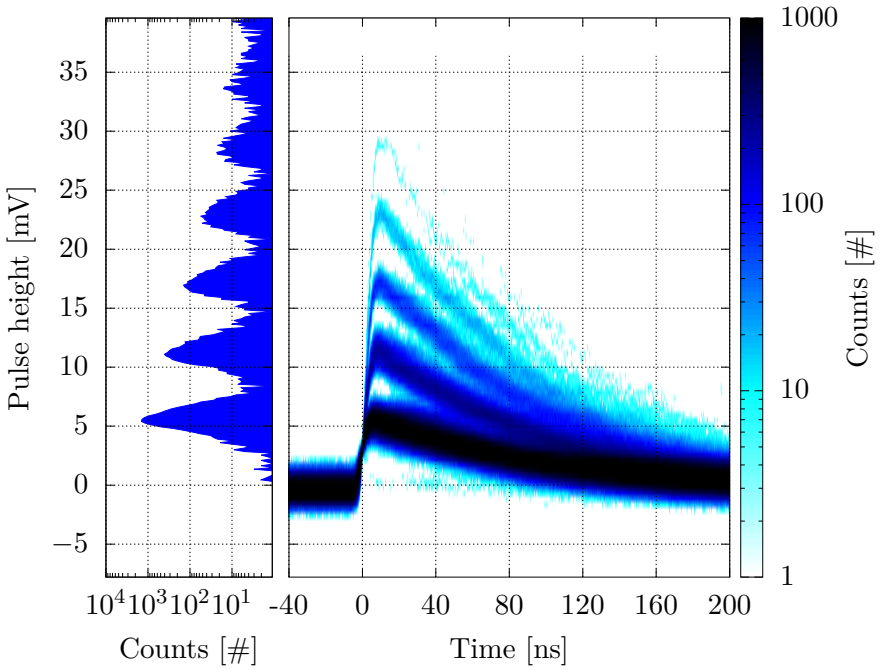

Figure 1.18: Displayment of many hundreds of pulses overlayed to each other. The colour indicates the counts. It can be distinguished between 1 p.e., 2 p.e. and higher orders. At the left, the projection of the number of pulses is shown. It is called pulse height spectrum. It shows the quantification of the individual pulse heights.

Geometric Efficiency:
Not the entire surface of a SiPM contributes to the sensitive area. This is due to the quenching resistors and conduction paths at the surface as well as the trenches between the pixels. All these components reduce the ratio of sensitive and entire detector area. This fraction is called geometric efficiency ϵ_{geo}. It depends on the size of the pixels as well as on their total number. For a fixed area A_{SiPM}, ϵ_{geo} increases for fewer but larger pixels. Typical value of the pixel pitch are about 50 µm [9]. The total area A_{SiPM} is about 1 mm^2 to 36 mm^2 [32, 43, 44].

Single Photon Resolution:
A SiPM has a single photon resolution. The reason is the pixel structure operated in Geiger mode. For a given U_{over}, the same amount of secondary electrons is generated during one avalanche for every pixel. Thus, the response of the pixels is uniform. The signal of every pixel is summed up to the total output and the signal of two triggered pixels is about twice the one of one triggered pixel. This can be seen in fig. 1.18. It shows the output voltage depending on the time. Several pulses of a measurement are plotted in overlay. The colourbar indicates the number of counts. The lowest pulse corresponds to one triggered pixel, the next one to two and so on. Since the number of triggered pixels corresponds to the number of created photoelectrons, a pulse describing one triggered pixel is also called 1 photoelectron equivalent (p.e.), higher ones 2 p.e. etc. In fig. 1.18, there are up to 5 p.e. visible. Single photons are detected assuming that one photon impinges onto one pixel. This only works for low intensities as every SiPM has a finite amount of pixels. For large intensities, saturation effects occur. In order to guarantee a linear response, only low intensities and a uniformly illumination should be used.

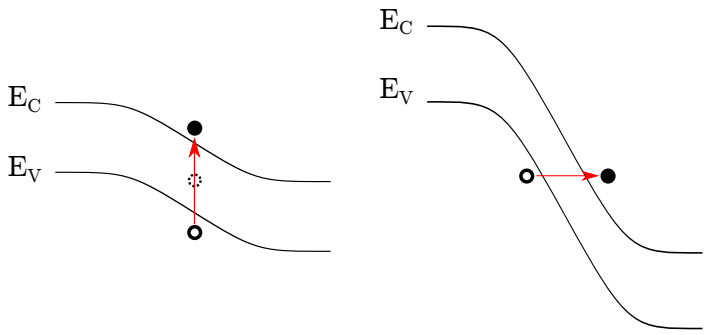

(a) Thermal generation

(b) Field-assisted generation (tunneling)

Figure 1.19: Schematic view of the two main process responsible for DCR: thermal generation (a) and field-assisted generation (b). Both processes can also happen trap-assistedly meaning that the excitation is firstly to a trap and then to the conduction band. This requires less energy. Adapted from [9, 38].

1.3.4 Contributions to noise

There are different components contributing to the noise in a SiPM. These are the darkcount rate (DCR), afterpulsing (AP) and optical crosstalk (CT). They can be classified into primary or uncorrelated noise in case of the DCR and secondary or correlated noise including both AP and CT. The different contributions and processes are discussed in the following.

1.3.4.1 Darkcount Rate

Even in the total absence of photons, there will be signals detected. This is due to the darkcount events. The counts per time is called DCR. There are two main processes. The first one is the thermally induced generation of electron-hole pairs. It is caused by the transition of an electron from the valence band into the conduction band due to phonon interactions. This is shown in fig. 1.19a. E_V denotes the upper edge of the valence and E_C the lower level of the conduction band. Due to the thermal movement of the lattice, the electrons can gain enough energy to be directly excited from E_V to E_C. Defects and impurities can strongly increase this probability.

The second process responsible for the DCR is the field-assisted charge carrier generation or internal field emission. The model was developed from C. Zener for insulators in 1934 [45] and further developed for semiconductors by K. B. McAfee et al. in 1992 [46]. According to [47], internal field emission includes band to band tunneling as well as tunneling from defect centers. As the density of defect centers in the breakdown region should be small, it can be neglected. The mechanism of band to band tunneling is displayed in fig. 1.19b. It only becomes relevant for high U_{bias}, e.g. several volts above U_{break} [47]. In this case, the curvature of both valence and conduction band is increased until it is possible for the electrons to transit from E_V to E_C. This is called direct band-to-band tunneling. This effect strongly increases for a higher U_{over}.

Further related to tunneling processes is the so-called Poole–Frenkel effect proposed by J. Frenkel in 1938 [48]. It describes how an electron can be excited into the conduction band even when its thermal energy is much lower than E_g. This is because part of its energy comes from the large electric field.

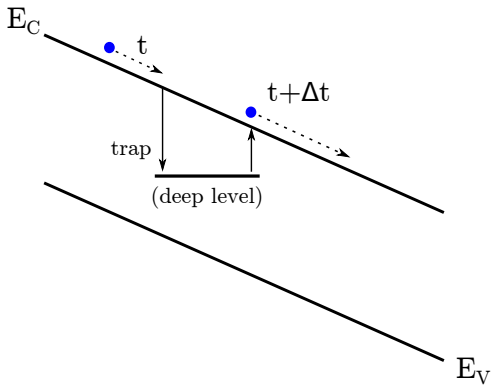

Figure 1.20: Schematic view of the trapping mechanism during an avalanche process. An electron in the conduction band is trapped at time t into a deep level defect. After a certain time $t + \Delta t$, the electron is released from the trap. Adapted from [10, 33].

Other effects have to be taken into account, too. For higher U_{over}, the trigger probability increases causing more often a free charge carrier to generate a signal [49]. This increases the voltage dependence of the DCR even more. As already mentioned in sec. 1.3.3, the number of free charge carriers and the total pixel size have a strong impact on the DCR. The more free charge carriers are available in a pixel, the higher the DCR will be imposing an upper limit on the feasible pixel size [31]. Every free charge carrier in the depleted region of a pixel can trigger an avalanche and an output signal. This signal is identical to one originating from an incoming photon. Since the DCR depends on U_{over}, it can be reduced to lower the DCR. This is not always wanted because of the reduction of G going along with a worse signal-to-noise ratio. Another possibility is cooling. Typcial values for the DCR are (0.1–1) MHz/mm^2 [9, 31] at room temperature which can be reduced down to few Hz/mm^2 for temperatures of about $-100\,^\circ$C.

1.3.4.2 Afterpulsing

Another process sometimes referred to as secondary dark pulses is AP. The exact mechanisms are not fully understood yet. It is commonly believed to originate from electrons which have been trapped during an avalanche at time t in deep level or impurity defects of the silicon. These charge carriers are released after some time $t + \Delta t$. This is schematically drawn in fig. 1.20. If the trapping occurs after the dead time of the pixel, the released charge carrier can trigger another avalanche. When this happens during the recovery time of the pixel, the signal will be significantly lower than a 1 p.e. pulse. Pulses occuring after the recovery time have the pulse height of a 1 p.e. pulse.

The time of release depends on the mean lifetime τ_{A} of the trap. It is closely related to the energy of the trap level and is different for every single trap. S. Cova et al. measured lifetimes between several ns and µs [50] at 30 °C. They also observed a strong increase for lower temperatures in the range of one order of magnitudes. Measurements of F. Retière indicate no or at least no strong dependence of τ_{A} on U_{over} [51].

Similar to the DCR, there are several effects believed to be responsible for the release of charge carriers from the traps. The first one is thermal excitation. This explains the strong temperature dependence of τ_{A}. Furthermore, there are two kinds of electric field effects [52]. The first one is the Frenkel-Poole effect already mentioned in sec. 1.3.4.1 which is the dominant one for low

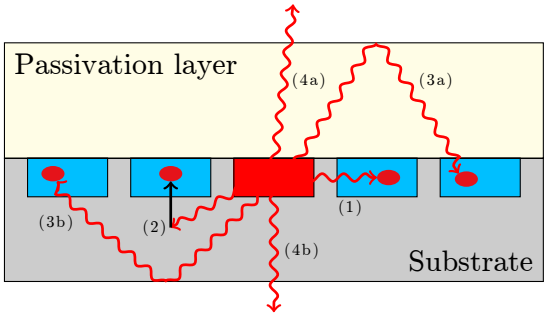

Figure 1.21: Different interaction mechanisms of photons produced during an avalanche in a pixel. Adapted from [55].

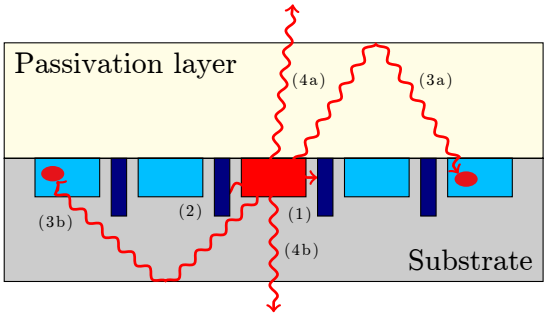

Figure 1.22: Schematic view of the reduction of CT by integrating deep trenches filled with a highly absorbing material between the single pixels. Adapted from [55].

electric fields according to [52]. In the presence of an electric field, the potential barrier is lowered [53, 54]. This increases the probability to release the charge carrier. Tunneling effects can further increase the number of charge carriers released from a trapping center. G. Vincent et al. divide tunneling into pure tunneling only governed by the electric field and U_{over} as well as phonon assisted tunneling where part of the energy is provided by phonon interactions [52].

Other aspects have to be taken into account, too. The number of trapped charge carriers increases with the gain. The more charge carriers are trapped, the earlier will be the release of the first one. The probability has been measured in [50]. It decreases exponentially over time. Not every released charge carrier triggers an avalanche. The earlier a charge carrier escapes from the trap, the lower is the voltage the pixel has already recovered to which lowers P_{trig}.

The probability P_{AP} of an afterpulsing event can be calculated via the product of the probability P_{cap} to capture an electron, the exponential decrease of τ_{A} with time and P_{trig} [33]:

$$P_{\text{AP}} = P_{\text{cap}} \cdot \frac{\exp\left(-\frac{t}{\tau_{\text{A}}}\right)}{\tau_{\text{A}}} \cdot P_{\text{trig}} \propto U_{\text{over}}^2 \,. \tag{1.10}$$

Because of the individual τ_{A} of the single traps, one must actually sum over the different τ_{A_i}. As P_{cap} depends linearly on G and therewith on U_{over} which also applies to $P_{\text{trig}} \propto U_{\text{over}}$, a quadratic dependence on U_{over} is predicted. This could be experimentally confirmed by [51].

1.3.4.3 Optical Crosstalk

When one pixel is triggered, a signal can be induced in a neighbouring pixel. There is no general explanation for this effect so far. It is commonly believed to be produced by optical photons generated during the avalanche process. These photons can undergo different processes shown in fig. 1.21. They can either reach directly (1) a neighbouring pixel and trigger an avalanche or indirectly via reflections at the top (3a) or bottom (3b) of the SiPM. A negligible fraction can create an electron-hole pair in the substrate (2) which diffuses to the pn-junction of the pixel and can trigger a retarded avalanche. As the diffusion takes a certain time, it is often referred to as delayed crosstalk. Reflections at the front or back of the device can trigger non-adjacent pixels. Not all photons interact with the material of the SiPM. Some leave the front (4a) or back (4b) of the SiPM. According to [56], this happens much more often for (4a) than for (4b). Trenches

are implemented between the pixel filled with a highly opaque material to absorb the photons and reduce CT. This is illustrated in fig. 1.22. Mechanism (1) and (2) can be reduced while (3a) and (3b) remain mostly undisturbed. Recent investigations by I. Rech et al. [56] indicate that (3b) has a strong contribution to CT. For both processes (1) and (3), the photon propagation time is so short that the original as well the additional avalanches occur simultaneously within the time resolution [51]. It has been measured that for typcial gain values of 10^6, there are about 30 photons created [57]. This deteriorates the achievable photon counting resolution significantly since two ore more events are detected instead of the one initial event. With respect to the nEXO experiment, it is important to determine the CT probability and correct for it.

The exact mechanisms for the origin of those photons are not finally clarified. There are various possible explanations and theories. N. Akil et al. developed a model including several mechanisms and investigated different pn devices [58]. According to the model, there are at least three different processes responsible for the production of the photons. At lower energies up to $\approx 2\,\mathrm{eV}$, primarily indirect interband transitions are believed to be the origin of photon emission in silicon. An electron from the conduction band transits to the valence band where only a part of the released energy is transferred to the emitted photon whereas the rest goes into the excitation of phonons. From $\approx 2\,\mathrm{eV}$ to $\approx 2.3\,\mathrm{eV}$, intraband Bremsstrahlung processes seem to dominate the photon emission. This involves relaxations between states of either an electron within the conduction or a hole within the valence band, respectively. Photons with higher energies may be produced by direct interband transitions. The entire energy is transferred to the photon resulting in energies up to 3.4 eV. A. G. Chynoweth and K. G. McKay observed no significant temperature dependence of the photon emission spectrum [59].

Not every photon induces a signal. One has also to consider P_{trig} which is proportional to G and thus U_{over}. In addition to that, the number of photons produced within an avalanche increases with G. This suggests a quadratic increase of CT with U_{over} which could be confirmed in [51]. As both CT and AP can only govern an initial event, they are labelled as correlated noise.

1.3.5 Photon detection effiency

One of the most important characteristics for a SiPM is the PDE. This is the probability that an incoming photon induces a signal in the SiPM. It can be determined as the product of the following quantities [9, 33, 60]:

$$\begin{aligned}\mathrm{PDE} &= \epsilon_{\mathrm{geo}} \cdot \mathrm{QE} \cdot P_{\mathrm{trig}} \\ &= \epsilon_{\mathrm{geo}}(A_{\mathrm{SiPM}}, A_{\mathrm{pixel}}) \cdot \mathrm{QE}(\tilde{T}, \lambda, T) \cdot P_{\mathrm{trig}}(U_{\mathrm{over}}, x)\,. \end{aligned} \tag{1.11}$$

The geometric efficiency ϵ_{geo}, the quantum efficiency (QE) and the trigger probability P_{trig} determine the PDE. All three quantities acquire values between 0 and 1. ϵ_{geo} describes the percentage of the sensitive area limited by the ratio of A_{SiPM} and A_{pixel}. This has already been described in detail in sec. 1.3.3. ϵ_{geo} is desired to be as close to 1 as possible which increases the fraction of light reaching the sensitive area. It typically lies between 0.6 and 0.8 [31].

The QE is the probability that a photon generates an electron-hole pair which arrives at the avalanche region [33]. There are two factors which determine the QE. The first one is the external QE of the SiPM. It is determined by the reflection, absorption and transmission of light at the surface. For the QE, the transmission $\tilde{T}$ on the surface of the SiPM is most important. Due to the different refractive indices of silicon and air, a relatively large fraction of incoming light is reflected

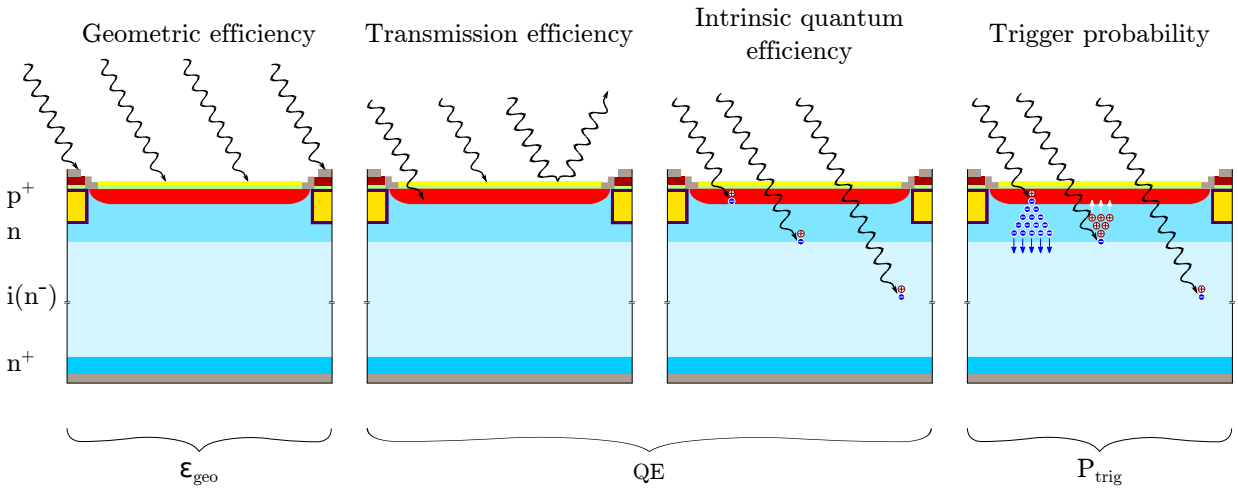

Figure 1.23: Summary of the different components determining the final PDE value. This includes the geometric, transmission and intrinsic quantum efficiency as well as the trigger probability. Adapted from [33].

at the top of the pixel. The reflectance can reach up to 30 % [31]. In order to reduce this, an antireflective coating can be applied which maximises $\tilde{T}$. It should further be mentioned that $\tilde{T}$ is angle dependent implicating an angular dependence of the PDE as well. The probability for a photon to pass the entrance window and generate an electron-hole pair in the active volume is the intrinsic quantum efficiency. It is strongly dependent on the wavelength λ of the incoming light. The total QE can reach (80–90) % which is a lot higher than for example for PMTs (see sec. 1.4.3).

Because of the strong dependence of P_{trig} on U_{over}, the PDE increases with U_{over} as well. Although a high U_{over} would be desired, this is mostly not possible because of the accompanied increase of parasitic noise such as CT, AP and DCR. Eventually, there has to be found a compromise between noise and PDE. In contrast to several noise contributions, the PDE does not seem to have a strong temperature dependence [41] suggesting that cooling could reduce parasitic noise drastically without any efficiency losses. The several dependencies of the PDE are combined in fig. 1.23 once more.

1.3.6 Requirements for the nEXO Experiment

Concerning the nEXO experiment, the required specifications impose a challenge especially with regard to the SiPMs. They will be used because of several advantages compared to other light detector such as PMTs or avalanche photodiodes (APDs). One of them is the condition that for the single compounds of the nEXO detector, only ultrapure materials are used. Silicon can be manufactured extremely radiopure which is not the case for PMTs. The required maximal radioactivity content contributed by SiPMs is specified to be 0.1, 1, 10 nBq/mm^2 for ^{238}U, ^{232}Th and ^{40}K, respectively [61]. The radiopurity would also be provided by APDs, but those fail to detect single photons. This is necessary for nEXO because of the huge detector volume resulting in a large mean propagation path of the generated photons. Very low light intensities reach the photodectors. The probably most challenging requirement is the property to detect ultraviolet light of $\lambda = (170\text{–}180)$ nm [61]. This is problematic since standard SiPMs are not sensitive to UV

Table 1.1: Requirements for SiPMs concerning the nEXO experiment [26, 61].

Parameter	Specification	Comment
U_{over}	$> 3\,\text{V}$	for negligible electronic noise
Gain	$> 3 \times 10^6$	for negligible electronic noise
PDE	$> 15\,\%$	at (170-180) nm in gas/vacuum
DCR	$< 50\,\text{Hz/mm}^2$	at -104 °C
Correlated noise	< 0.2	at -104 °C, combining CT and AP within 1 µs
Single photodetector active area	$> 1\,\text{cm}^2$	
Radioactivity content	(0.1, 1, 10) nBq/mm^2	for ^{238}U, ^{232}Th and ^{40}K, respectively
Gain fluctuations and electronic noise	< 0.1 p.e.	
Capacity	$< 50\,\text{pF/mm}^2$	for read-out electronics
Single photon timing resolution	$< 100\,\text{ns}$	

light. The reason is that UV light is absorbed in the antireflective layer. For this application, only special SiPMs can be used without any antireflective coating. This lowers the PDE because of the lower $\tilde{T}$ and QE. The detection of UV light is problematic due to the extremely short absorption length. Special treatments and doping structures have to be applied. An overview of the demanded characteristics is given in tab. 1.1. Some of those quantities such as capacity and gain fluctuations depend on the final read-out electronics and are not relevant here. Others, like the active area and radioactivity are already achieved or still have to be tested on the final sample. The main focus lies on the PDE together with the noise contributions DCR, CT and AP. A PDE of at least 15 % is required with a correlated noise of less than 0.2 with 1 µ. The DCR should not exeed 50 Hz/mm^2. It has to be mentioned that the values for all parameters have to be obtained at cryogenic temperatures of about $-100\,°\text{C}$.

1.4 Photomultiplier Tubes

PMTs are light detectors capable of identifying single photons. They cover a broad spectrum of implementations within particle physics since their first application in the 1930s. Their uncomplicated operation, low darkrate and a high amplification factor are optimal properties for experiments investigating low light intensities. They are no choice for the nEXO experiment due to the relatively large background from radioactive contaminations of the detector itself compared to SiPMs. A PMT has been used as a reference detector to evaluate the light response of a SiPM in this work. Their influence to the output parameters, the single components of a PMT, their operating principle and the most relevant operating parameters are explained. An overview of the noise constituents is given which will be important for a better understanding of the single photon spectrum measurements.

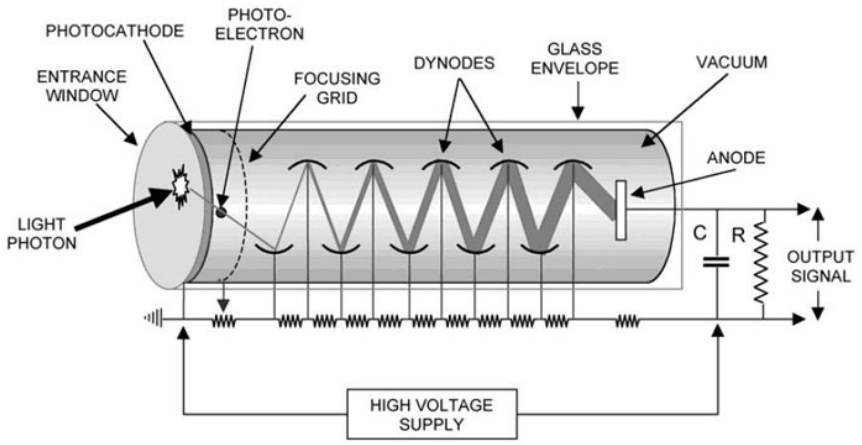

Figure 1.24: Principle structure of a PMT. The basic components are the photocathode converting the light into electrons which are amplified by the dynode structure. At the end, the electrons are collected by the anode. The entire system is placed into a vacuum tube made of glass. Voltage divider are connected to the dynodes for a cascading potential. Reprinted from [63]

1.4.1 Basic Structure and Operating Principle

A PMT converts light into an electric signal and amplifies it. This property is similar to a SiPM, whereas the structure of a PMT is completely different. This can be seen in fig. 1.24 for a transmission mode head-on PMT as such a type is used in this thesis. Further types along with a detailed description can be found in [62]. A PMT consists of an evacuated glass tube with an entrance window on one side. In case of a head-on PMT, it is located at the front of the tube. Incident light passes the entrance window and impinges onto the photocathode. It is semi-transparent for a transmission mode PMT. The photon creates a photoelectron which is directed onto a series of electrodes (dynodes) by a focusing grid. Their purpose is to amplify the single electron to a measurable signal which is tapped at the anode. A high voltage is applied via voltage dividers in order to ensure a stable amplification. The two fundamental phenomena of the operation principle of a PMT are photoemission and secondary emission (see sec. 1.4.2).

1.4.2 Single Components

A PMT is assembled by several components which are essentially for the signal formation. In the following, the different elements are explained in more detail.

Entrance Window
Incident light passes the entrance window. Different materials possess different transmission properties. Borosilicate glass is only suitable for wavelengths higher than 300 nm, whereas ultraviolet glass, quartz, magnesium fluoride and sapphire have transmissions down to the ultraviolet region. Quartz has the advantage of a low radioactive background, while sapphire can also resist severe environmental impacts [64]. Not only the material but also the geometry must match the application. Sometimes, a small entrance window of $5\,\mathrm{cm}^2$ is sufficient whereas other applications require a sensitivity of almost $360\,^\circ$. The PMT used in this work has a sensitive area of about $420.25\,\mathrm{mm}^2$.

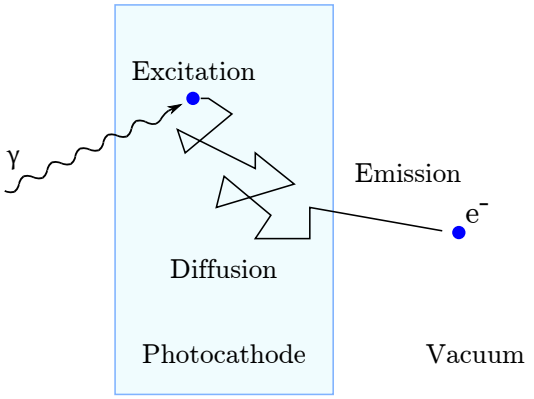

Figure 1.25: The three steps of photoemission occuring in the photocathode of a PMT. An incident photon creates an electron via the external photoeffect (excitation). It diffuses to the surface of the photocathode and is emitted into the vacuum. Adapted from [65].

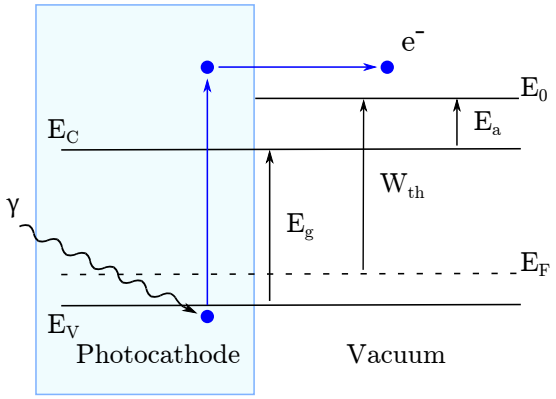

Figure 1.26: Photoemission process in the band model for an alkali metal. The minimum energy for the electron is $E_{\mathrm{min}} > E_{\mathrm{g}} + E_{\mathrm{a}}$. Adapted from [65, 66, 67].

Photocathode:
The photocathode converts the incoming light into electrons. For head-on geometries, the photocathode material is applied at the inside of the entrance window. It is semi-transparent and emits the electrons in the opposite direction to the incident light. This is called transmission mode. The photoemission process can be separated into three distinct sub-processes. Those are excitation, diffusion and emission. They are shown in fig. 1.25. In the following, the processes are described in more detail for the case of a metal photocathode as used in this work.

An incoming photon with energy $E_{\mathrm{ph}} = h \cdot \nu > E_{\mathrm{g}}$ reaches the photocathode and excites an electron to the conduction band via the external photoelectric effect. In fig. 1.26, the underlying process is shown for an alkali metal with positive electron affinity. Valence and conduction band are separated via the band gap E_{g}. The released electron in the material diffuses to the surface. On its way, it loses energy due to collisions with other electrons and phonons. In metals, the conduction band is partially occupied by electrons and the main energy loss of the photoelectron happens via collisions with free electrons of the material. This leads to an escape depth of only a few atomic radii [65]. In order to be emitted into the vacuum, the electron must have received enough energy to overcome the potential barrier of the photocathode surface which is the work function W_{th}. The necessary minimum energy for the electron is the sum of the band gap and the electron affinity: $E_{\mathrm{min}} > E_{\mathrm{g}} + E_{\mathrm{a}}$. If the photoelectron has lost so much energy that it could not overcome the surface barrier, it will not be emitted into the vacuum. The entire emission process last typically less than 10^{-11} s [68].

Electron-Optical Input System:
The electron-optical input system collects and focuses the emitted electrons onto the first dynode. A schematic sketch of the relevant parts as well as of some equipotential lines and electron trajectories is depicted in fig 1.27. Photocathode and focusing electrode are on the same potential whereas the accelerating electrode is on the same potential as the first dynode.

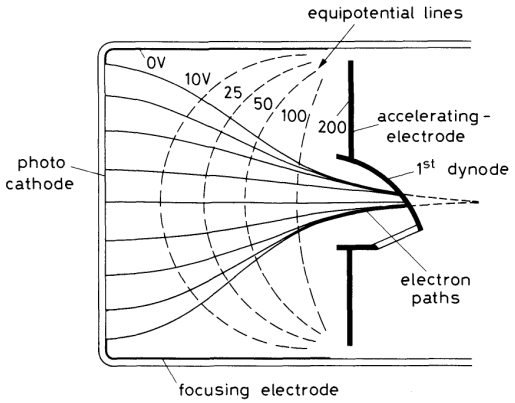

Figure 1.27: Schematic view the electron-optical input system of a PMT. Its basic components are the photocathode, a focusing electrode at the side of the tube and an accelerating electrode. Reprinted from [65].

The electron-optical input system has to fulfil two requirements. Firstly, the system must focus as many electrons onto the dynode as possible, independently on the initial velocity and point of origin of the electrons. The second requirement is that the transit time t_{transit} the electrons need from cathode to first dynode should not differ for different points of origins and velocities [65].

Multiplier Structure:
When the photoelectrons are focused onto the first dynode, they have to be converted into a measurable signal. This is performed by the multiplier structure consisting of several dynodes. The photoelectron impinges onto the first dynode and produces further electrons, the so-called secondary electrons. This multiplication process is repeated over several stages until a sufficient amplification is achieved. The secondary emission process is similar to the photoemission with the difference that the energy is now provided by the primary electron and more than one additional electron is generated. There are different dynode configurations available. The PMT used in this work consists of a metal channel dynode structure. It is formed of extremely thin electrodes which are very close to each other.

Voltage Dividers:
For secondary emission, a constant electric field between the dynodes is important. Each dynode must be at a higher potential than the previous one and stable over time. The most feasible way to achieve this is to use a stabilised high voltage supply (HV) together with voltage dividers. Commonly, some resistors in parallel to the dynodes are used. Other types can be found in [65]. The resistor chain can consist of equal resistances resulting in equal voltage steps between all dynodes and the maximum amplification for a fixed HV. Another option is to increase the interdynode voltages towards the anode. This can increase the output pulse or optimise time characteristics.

The HV can be applied as positive or negative polarity [65, 66, 69]. Positive polarity means that the photocathode is maintained at ground while the anode is at a very high positive potential. This configuration is usually preferred when low intensities and pulse counting is used (for different operating modes see also sec. 1.4.3). For negative polarity, the photocathode is on a high negative potential whereas the anode is grounded. In this case, the tube has to be insulated from the

surroundings. Negative polarity is mostly used for continuous flux measurements. In this work, positive polarity is used.

Capacitors in parallel to the resistors are sometimes added between the last few stages of dynodes. Those help to improve the output linearity. At the end of the electron multiplier system, high currents can occur. The capacitors are inserted to provide the necessary charge during a peak periode [64, 69].

Anode:
The secondary electrons emitted from the last dynode have to be collected and transferred to an external circuit. This is performed by the anode. In general, a rod, plate or mesh electrode is used [66]. An appropriate potential difference between the last dynode and the anode is important to minimise space charge effects. High currents especially during the last stages of multiplication and at the anode can form an electron cloud around the emitting electrode. For high densities, it can superimpose the applied electric field. Further arriving electrons are repelled. Larger resistances are chosen between the last dynodes and the anode to avoid this. Finally, the anode impedance has to be in accordance with the impedance of the output connection [65, 66, 69].

1.4.3 Operating Parameters

For the performance of measurements, several operating parameters are substantial. The most relevant ones for this work are discussed in the following.

Detection Efficiency:
The detection efficiency (DE) is the ratio of the number N_γ of detected events to the number N_{ph} of incident photons [66, 69]:

$$\mathrm{DE} = \frac{N_\gamma}{N_{\mathrm{ph}}}\,. \tag{1.12}$$

It consists of two components. The first one is the QE which is the probability that an incident photon creates a photoelectron. It can be written as the ratio of the number N_{e} of created electrons and the number of impinging photons:

$$\mathrm{QE} = \frac{N_{\mathrm{e}}}{N_{\mathrm{ph}}}\,. \tag{1.13}$$

Typical values of the QE are between 10 % and 30 % [64, 70]. The second component is the collection efficiency (CE) of the first dynode. It is the ratio of the number of photoelectrons reaching the first dynode and the number of photoelectrons leaving the photocathode. It is typically larger than 80 % [65]. Strictly speaking, each single dynode has its own collection efficiency contributing to the overall CE. This is neglected in the following, since the most relevant parameter is the CE between cathode and first dynode. The efficiency to collect the single photoelectron is much lower than the one for the already multiplied signal at later stages. So finally, the DE can be written as the product of QE and CE [66]:

$$\mathrm{DE} = \mathrm{QE} \cdot \mathrm{CE}\,. \tag{1.14}$$

Both QE and CE depend on the wavelength.

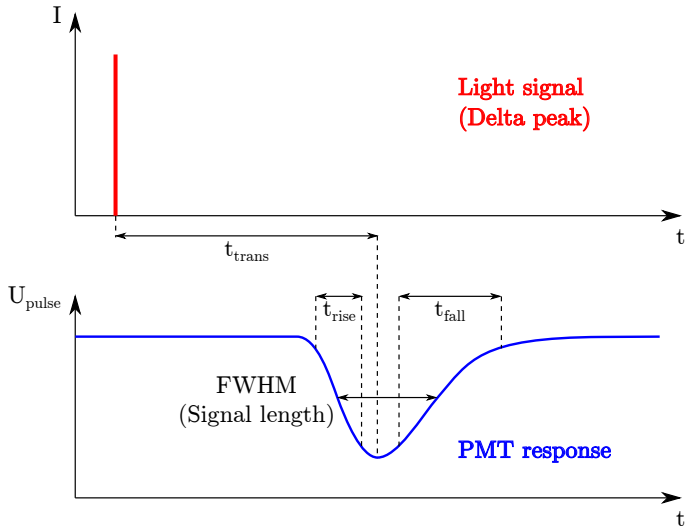

Figure 1.28: Time characteristics of a PMT. The FWHM describes the pulse width. Adapted from [64, 66, 67].

Gain:
The multiplication factor of the photoelectron to the number of secondaries reaching the anode is called gain M. It is the product of the CE and the secondary emission coefficients of the single dynodes [65, 66, 69]:

$$M = \mathrm{CE} \cdot \prod_{i=1}^{n} \delta_i \overset{\delta_i \equiv \delta}{=} \mathrm{CE} \cdot \delta^n \,. \tag{1.15}$$

For a uniform behaviour of all dynodes, the secondary emission coefficients δ_i are equal and eq. 1.15 can be simplified such as shown above. Typical values for δ are between 3 and 50 [10]. With 3 to 10 multiplication stages of the PMT, this leads to M in the order of 10^4 to 10^7.

Pulse shape:
The pulse shape can be described by three parameters which are transit time, rise time and FWHM. They are shown in fig. 1.28. A light signal – indicated as delta peak – impinges onto the PMT. The time between the occurence of the peak and the signal response of the PMT is called transit time t_{trans}. It depends on the dynode structure and lies typically in the range of 10 ns to 100 ns [64]. The rise time t_{rise} lasts only 1 ns to 20 ns and is the time the signal needs to increase from 10 % to 90 % of the pulse height [66]. The FWHM describes the signal length. It is usually 2.5 times larger than t_{rise} [66]. One can also take the fall time which is the time required to decrease from 90 % to 10 % of the pulse height.

Operation Modes:
A PMT can be operated in different modes. The first possibility is to operate the PMT in current mode. The signal charge is integrated and the current output is proportional to the total charge of each pulse. The anode output can be connected directly to a current measuring device and negative polarity has to be used. This kind of operation mode is mostly used for high intensities and a constant illumination or a high frequency. But only anode output currents lower than 100 µA can be managed [64, 65, 67].

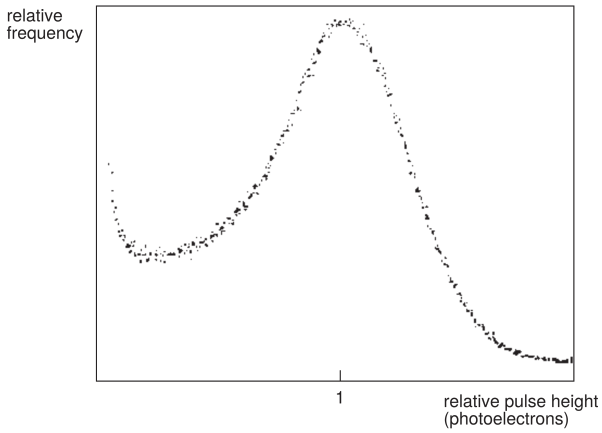

Figure 1.29: SES of a PMT normalised to the height of 1 p.e. The nonzero width of the 1 p.e.-pulse results from the fluctuations in the photoemission and secondary emission processes. The accumulation of events < 0.5 p.e. originates from events with a lower multiplication factor such as inelastically backscattered electrons. Reprinted from [65].

Another option is to use pulse mode. It is often applied together with positive polarity. The anode output has to be connected to a resistor at first and then the signal voltage can be measured. This allows to investigate individual pulses for amplitude, charge and time characteristics. Pulse mode is mostly used for measurements of low light intensities. PMTs operated in this mode can handle high peak currents such as 200 mA [64]. A special case of the pulse mode is the so-called photon counting mode. Each detected photon is resolved separately at the anode of the PMT. This is only possible for extremely weak intensities and frequencies so that there is no pile-up of the single pulses. The PMT in this work has been operated in the photon counting mode.

Single Electron Spectrum:
When the amplitude of single electrons is plotted into a histogram, one obtains a single electron spectrum (SES). An example is shown in fig. 1.29. The pulse height is normalised to the height of 1 p.e. Large fluctuations in the secondary emission process cause large amplitude variations in the spectrum. An incident photon can simply pass through the photocathode and create a photoelectron at one of the dynodes. Because of the smaller amplification factor, a resulting pulse will be smaller. According to [71], this contribution is rather small. Another problem are electron losses within the muliplier system. This can happen either by reflection and absorption at the dynode or by electrons leaving the active area of the multiplier. Both loss mechansisms result into a shift of the SES to smaller values. The most relevant process producing small pulses are inelastically backscattered photoelectrons at the first dynode. These electrons are accelerated towards the dynode again yielding a lower energy fraction than before the collision. This lowers the amplification factor significantly. It happens for a relatively large fraction between 10 % and 20 % resulting in pulses with an amplitude of only 1/3 with respect of the single electron pulse height [65, 71].

1.4.4 Contributions to Noise

In general, there are three major contributions to noise. The first one are statistical fluctuations which broaden the SES. Darkcount events produce signals even in the absence of light. Several correlated background processes can occur provoked by either a real signal or a darkcount event. A description of the single mechanisms and originating processes is given in the following.

1.4.4.1 Statistical Noise

It has already been indicated that the broad distribution in fig. 1.29 arises from fluctuations in the signal. These are due to the nature of noise. This statistical noise – sometimes also called shot noise – always accompanies a signal and cannot be eliminated. In a PMT, shot noise originates from fluctuations in the number of created photoelectrons as well as fluctuations in the secondary emission process [64, 65, 66, 69, 72].

1.4.4.2 Darkcount and Darkcurrent

Not all noise contributions originate from shot noise which only occurs when a signal is detected. There is also a noise contribution even without any incident light. This is the DCR or darkcurrent in case of continuous readout. There is a continuous contribution resulting in a fluctuation around a mean value as well as discrete peaks which occur at random times. In the following, the different components are described according to [10, 64, 65, 69, 72, 73].

Because of the conductivity of the single components such as electrode supports, envelope, base and socket, there is always a leakage current. It is the only continuous DCR component. Imperfect insulation can result into higher leakage currents. It is the dominant component for low temperatures and a low U_{PMT}.

One of the main contributions to the pulsed component of the DCR is the thermionic emission. It primarily arises from the photocathode, but also the emission from the dynodes contribute. There is a strong temperature dependence. At room temperature, thermionic emission is the dominant contribution to DCR whereas it is negligible for lower temperatures. The induced current increases linearly with the gain thus increasing exponentially with U_{PMT}. DCR pulses generated by thermionic emission are usually of single electron type or smaller.

In general, the electric fields inside a PMT are fairly low. Strong fields can occur because of the unavoidable roughness of the electrode surfaces. The adsorption of alkali metals at the electrodes considerably lowers their electron affinity. Both effects cause the so-called field emission. Due to the high electrostatic fields and lowered surface barrier, electrons can be emitted at the dynodes. These electrons can hit other surfaces inside the PMT and can cause the emission of photons which can reach the photocathode. This induces a DCR signal. There is no strong temperature dependence, but it increases non-linearly for larger U_{PMT}. As it increases faster than the gain, field emission is the dominant process for high supply voltages. This imposes a practical limit to the maximum gain.

Background radiation is caused by different contributions. One aspect is natural radiation primarily from the window material. The decay of the radioactive nuclides produces either light by Cherenkov radiation or by the direct interaction with the photocathode. The passage of mainly electrons and muons from cosmic rays can generate Cherenkov radiation, too.

1.4.4.3 Correlated Background

Every signal – regardless if induced by an incident photon or a darkcount event – can be accompanied by a correlated background process. Their appearance artificially increases the DCR component and disturbs the timing as well as the photon counting performance. One can distinguish between four different contributions. The distinction is formed mainly by the time distribution.

Prepulses:
Prepulses are pulses preceding the main one. They are strongly correlated to the parent pulse. Prepulses occur when a photon passes the photocathode without any interaction but producing a photoelectron via the direct photoeffect on the surface of the first dynode or the focusing electrode. This photoelectron is then amplified in the normal procedure. As it so to say skipped one stage of amplification, such pulses are usually smaller than the main one. They also occur earlier in time. The time difference is almost the same as the transit time [74, 75].

Late Pulses:
Another contribution to correlated background in PMTs are late pulses. They can be attributed to electron backscattering effects mainly at the first dynode. This can happen either elastically or inelastically. In both cases, electrons scatter from the first dynode and then move in the opposite direction away from the dynode. Due to the electric field, they are slowed down and reaccelerated towards the dynode again where they produce a signal. For elastically backscattered electrons, the resulting signal is almost the same as a normal pulse. But for inelastically scattered electrons which occur with higher probability, the amplitude is much lower. Depending on the size of the PMT, the time delay can last between 10 ns and 100 ns [71, 74, 75, 76, 77].

Afterpulses:
Afterpulses have two main origins distinguished mostly by the time interval to the true pulse. Firstly, afterpulses can occur due to luminous reactions. By the impact of many electrons hitting the dynodes, photons are emitted. Some of those photons can reach the photocathode and induce a signal. This gives rise to afterpulses delayed by the sum of the light and electron pulse transit time which typically lies between 20 ns to 100 ns [65]. Much longer time delays occur because of ionisation of residual gases. Although the photomultiplier tube is maintained evacuated, there is still a certain amount of residual gases left inside. This is enforced by the migration of helium inside the tube as well as the desorption of materials of their structure. Accelerated electrons can hit those gas molecules and ionise them. The ions are accelerated in the opposite direction towards the photocathode or the dynodes. When they impinge onto the cathode or a dynode, they generate one or more secondary electrons which in return are accelerated and amplified. Such generated photoelectrons have a higher pulse height and longer delay if they originate from within the electron-optical input system, whereas photoelectrons from the multiplier system are smaller and less retarded. The delay with respect to the true pulse can vary between few hundred nanoseconds to several microseconds [65, 69, 71].

Scintillation:
One last component of correlated background is scintillation. Some of the electrons produced during the amplification process may deviate from their intended trajectories. They do not contribute to the output signal but impinge onto the glass envelope or onto parts of the dynode support structure and can produce scintillation light. When it reaches the photocathode, the photons can also cause correlated pulses.

Chapter 2

Absolute Calibration of a PMT

In this chapter, the absolute calibration of a photomultiplier tube of the type R8520-406 from HAMAMATSU K.K. is presented. The basic concept of the calibration is explained and the experimental setup used in this work is described. This includes the entire setup with focus on the PMT itself as well as further components such as the LED. The exact measurement and analysis is described along with the data processing and the detailed fit performance. The results of the single fits are shown together with the final result for $-100\,^{\circ}\mathrm{C}$. In the end, the analysis and the fit routines are discussed. Some suggestions for a further development of the entire measurement and analysis proccess are given.

2.1 Concept of the Absolute Calibration

For this work, the absolute calibration of a PMT means measuring the number of detected photons in terms of 1 p.e and calibrating the PMT with respect to the 1 p.e. pulse. It is substantial to know its exact value. E. H. Bellamy et al. developed a model to describe the realistic response of a PMT which determines the absolute value of the 1 p.e. pulse [78]. The basic idea is to determine the charge spectrum. A realistic PMT response function is fitted and some parameters are extracted which can be used for calibration purposes. It is fundamental to use an appropriate response function. According to E. H. Bellamy and S. Tokar [78, 79], the PMT can be divided into two independent parts. Firstly the photoconversion and electron collection and secondly, the amplification.

Photoconversion and Electron Collection:
A pulsed light source – for instance a LED – is considered. In most cases, the number of emitted photons is Poisson distributed. The photoemission process in the photocathode together with the subsequent collection of the electrones by the electron-optical input system is a random binary process. The resulting distribution is a superposition of Poisson and binary processes. This leads again to a Poisson distribution [78, 79]:

$$P(n;\mu) = \frac{\mu^n \cdot \mathrm{e}^{-\mu}}{n!} \qquad \text{with} \qquad \mu = N_{\mathrm{ph}} \cdot \mathrm{QE} \cdot \mathrm{CE}\,, \tag{2.1}$$

where $P(n;\mu)$ is the probability of observing n photoelectrons with the mean number μ which is the product of the number N_{ph} of photons hitting the photocathode, the quantum efficiency QE and the CE.

Amplification:
When one single photoelectron reaches the dynode system, the response of the multiplicative dynode system can be approximated by a Gaussian distribution. A large secondary emission coefficent at the first dynode ($\delta_1 > 4$) and a coefficent close to 1 is assumed for the first few stages. Then the response of the dynode system is given by [78]:

$$G_1(x) = \frac{1}{\sqrt{2\pi}\sigma_1} \cdot \exp\left(-\frac{(x-Q_1)^2}{2\sigma_1^2}\right), \tag{2.2}$$

in which x is the charge variable, Q_1 the average charge for the collection of 1 photoelectron and σ_1 the corresponding standard deviation.

One can also determine the distribution for the collection of more than one photoelectron by the first dynode. This needs the expansion of eq. 2.2 and the assumption that the amplification processes of distinct photoelectrons is mutually independent. In this case, the amplifier output is a superposition of n one-electron cases. It can be written as [78]:

$$G_n(x) = \frac{1}{\sqrt{2\pi n}\sigma_1} \cdot \exp\left(-\frac{(x-nQ_1)^2}{2n\sigma_1^2}\right). \tag{2.3}$$

Again, x denotes the charge, Q_1 the average collected charge of 1 p.e., σ_1 the standard deviation and n the number of photoelectrons.

The resulting response of an ideal PMT can be written as the superposition of eq. 2.1 and eq. 2.3. This gives [78]:

$$\begin{aligned} S_{\text{ideal}}(x) &= P(n;\mu) \otimes G_n(x) \\ &= \sum_{n=0}^{\infty} \frac{\mu^n \cdot \mathrm{e}^{-\mu}}{n!} \cdot \frac{1}{\sqrt{2\pi n}\sigma_1} \cdot \exp\left(-\frac{(x-nQ_1)^2}{2n\sigma_1^2}\right) . \end{aligned} \tag{2.4}$$

It is important to mention that in eq. 2.4, the scenario of a photoelectron missing the first dynode and being captured by one of the subsequent ones is neglected.

Background Processes:
An ideal PMT was considered so far. A real PMT will always suffer from noise contributions such as described in sec. 1.4.4. They generate an additional charge and modify the output charge spectrum. One can split the background processes into two different contributions. Type I background processes originate from low charge proccesses as for instance leakage current. They are present in every event and generate a non-zero signal when no photoelectron was created. This results into a pedestal with a Gaussian distribution. Type II are discrete background processes described by an exponential function. They can govern a measured signal with a certain probability. Examples are thermal emission, correlated noise, etc. (for an overview see sec. 1.4.4.3). On the basis that no primary photoelectrons are emitted ($n = 0$), the background function can be written as [78]:

$$B(x) = \underbrace{\frac{(1-w)}{\sqrt{2\pi}\sigma_0} \cdot \exp\left(-\frac{x^2}{2\sigma_0^2}\right)}_{\text{type I}} + \underbrace{w\theta(x)\alpha \mathrm{e}^{-\alpha x}}_{\text{type I + type II}} \tag{2.5}$$

$$\overset{\substack{1/\alpha \ll Q_1 \\ \mu \geq 2}}{\approx} \frac{1}{\sqrt{2\pi}\sigma_0} \cdot \exp\left(-\frac{(x-Q_0-Q_{\text{sh}})^2}{2\sigma_0^2}\right) , \tag{2.6}$$

where w is the probability that a measured signal is accompanied by a type II background proccess, σ_0 is the standard deviation of the type I background distribution, α is the coefficent of the exponential decrease of the type II background and $\theta(x)$ is a step function descibing:

$$\theta(x) = \begin{cases} 0 & x < 0 \\ 1 & x \geq 0 \, . \end{cases}$$

The first term in eq. 2.5 descibes the case when only the type I background proccess is present. It is a Gaussian function multiplied with the probability $1 - w$ that there is no type II background proccess. The second term corresponds to the case when an additional background event from the type II proccess occurs. It consists of the probability w for a type II background proccess and an exponential decrease. The step function ensures that there is only a contribution for $x \geq 0$. When the noise intensity can be assumed to be low ($1/\alpha \gg Q_1$) and the light intensity to be large ($\mu \geq 2$), eq. 2.5 can be simplified to eq. 2.6. In this case, Q_0 is the mean charge of the pedestal and $Q_{\text{sh}} = w/\alpha$ describes the effective spectrum shift due to background. The background function is then treated as a constant shift in the charge spectrum.

Final PMT Response:
Finally, the response function of a real PMT can be determined as the convolution of eqs. 2.4 and 2.5 to be [78]:

$$\begin{aligned} S_{\text{real}}(x) = & \int S_{\text{ideal}}(x')B(x-x')\,\mathrm{d}x' \\ \overset{\substack{1/\alpha \ll Q_1 \\ \mu \geq 2}}{\approx} & \underbrace{\left[\frac{(1-w)}{\sqrt{2\pi}\sigma_0}\cdot\exp\left(-\frac{(x-Q_0)^2}{2\sigma_0^2}\right) + w\theta(x-Q_0)\cdot\alpha\mathrm{e}^{-\alpha(x-Q_0)}\right]\mathrm{e}^{-\mu}}_{\text{background}} \\ & + \underbrace{\sum_{n=1}^{\infty}\frac{\mu^n\cdot\mathrm{e}^{-\mu}}{n!}\cdot\frac{1}{\sqrt{2\pi n}\sigma_1}\cdot\exp\left(-\frac{(x-Q_0-Q\mathrm{sh}-nQ_1)^2}{2n\sigma_1^2}\right)}_{\text{signal}}. \end{aligned} \tag{2.7}$$

The first term of eq. 2.7 describes the background contribution. It consists of the superposition of eq. 2.5 and a Poisson distribution for the case $n = 0$ The second term of eq. 2.7 refers to the signal distribution. It is the superposition of the Poisson distribution for $n > 0$, the response of an ideal PMT according to eq. 2.4 and the simplified background distribution descibed by eq. 2.6. This leaves seven free fit parameters of eq. 2.7. Q_0 and σ_0 describe the pedestal. The discrete background processes are characterised by w and α. Only the remaining three parameters – Q_1, σ_1 and μ – refer to the true signal. μ is the only parameter which is direct proportional to the intensity of the light source, whereas Q_1 and σ_1 describe the amplification process of the dynode system. For the analysis, an additional scaling factor was used as the 8th fit parameter.

2.2 Experimental Setup

The absolute calibration of the PMT was performed in the setup which is descibed in the following. A first overview of the entire setup is given in sec. 2.2.1 and the single components are described in more detail in sec. 2.2.2 and sec. 2.2.3. This corresponds especially to the PMT but also to further constituents as the LED and the supply devices.

2.2.1 Entire Setup

The entire setup can be seen in fig. 2.1. The main part consists of a PMT and a LED in opposite of it. In order to reduce the flux onto the PMT, the LED was turned away. Both PMT and LED were put into a dark box to reduce disturbing stray light from outside. As the focus of this measurement is the temperature dependence, the entire dark box was placed into a climate chamber which is able to cool down to about $-70\,^{\circ}\mathrm{C}$. A pulse generator was connected to the LED to operate it in pulsed mode. Only positive pulses with a width of 10 ns and a repetition rate of 5 MHz were used. The pulse amplitude was varied to generate different intensities. A second output of the pulse generator was connected to the oscilloscope and served as trigger. The PMT response was only stored to the hard drive when the oscilloscope had been triggered. It saved the voltage versus time values of 200 ns length with a time delay of -40 ns. A temperature sensor was placed directly onto the housing of the PMT to observe its operating temperature.

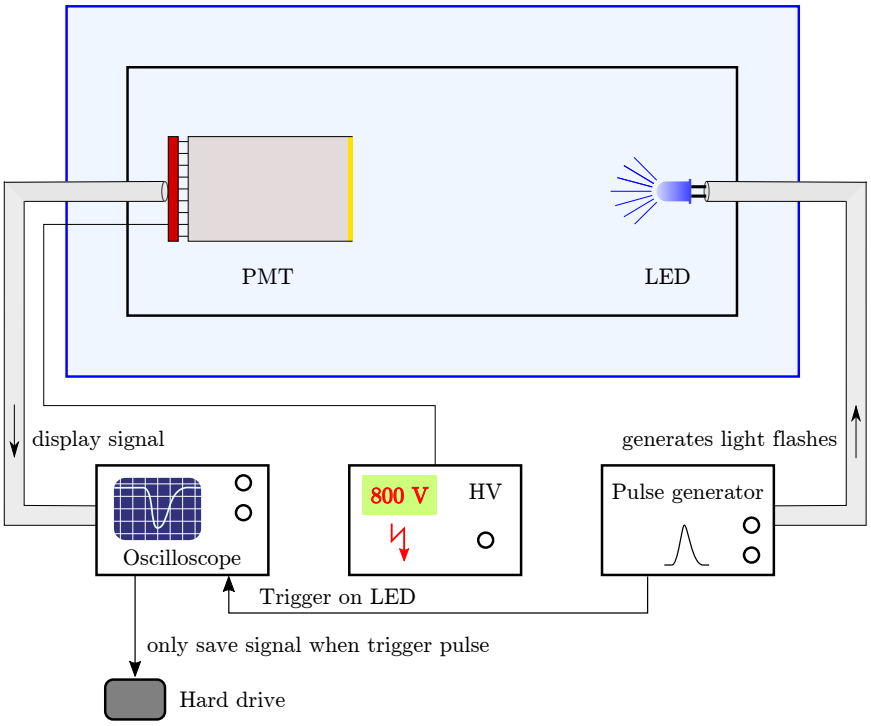

Figure 2.1: Setup for the characterisation of the PMT with a pulsed LED. The PMT is placed in a dark box and supplied with 800 V. Opposite to the detector, a blue LED is placed. The readout processing is managed in such way that the PMT signal is only saved in case the LED emitted light. For the investigation of temperature dependencies, PMT and LED are placed in a climate chamber.

2.2.2 PMT

A R8520-406 PMT from the Hamamatsu Photonics K.K. was used in this work. It was selected according to the requirements necessary to fulfil its role as a reference detector (see chap. 4). A picture can be seen in fig. 2.2. The PMT is mainly blue sensitive up to wavelengths of about 160 nm. This is necessary since the later application will be at wavelengths of about 175 nm. The wavelength of the maximum response is 420 nm. Synthetic silica is used as window material to increase the UV sensitivity. Another characteristic is the suitability for low temperature operation down to -110°C. This is important as later measurements will be performed at cryogenic temperatures (see chap. 4). The PMT has a bialkali photocathode with an effective area of about $(20.5 \times 20.5)\,\mathrm{mm}^2$. The dynode structure is a metal channel one with 10 numbers of multiplication stages. This compact structure provides excellent timing resolutions with an anode pulse rise time of typically 1.8 ns and an electron transit time of about 12.4 ns. The optimal supply voltage is about 800 V providing a gain of about 10^6. Further details can be found in [80].

2.2.3 Further Components

The entire setup includes further componets. The PMT is connected to a SHQ 122M power supply from the company iseg [82]. A blue LED from the HLMP-CB15 series of Agilent Technologies was used as a light source [83]. Its peak wavelength is 472 nm which corresponds appropriately to the peak sensitivity at 420 nm of the PMT. The LED is connected to a 1 Hz-125 Hz Philips pulse

Figure 2.2: PMT of type R8520-406 from Hamamatsu Photonics K.K. [80]. This type was used within this work as a reference detector. Reprinted from [81].

generator from the series PM 5785 with a risetime of 1 ns [84]. The signal was processed with a LECROY waverunner 1 Ghz oscilloscope from the 6100A series [85]. A climate chamber from TESTEQUITY LLC was used for the temperature regulation. It was from the model 1007C [86]. The temperature was measured with a NiCr-Ni temperature sensor from LEYBOLD [87]. It was directly connected to a readout CASSY-module which displays the absolute temperature [88].

2.3 Measurement and Analysis

In this section, the measurement and analysis is descibed. This includes the data processing as well as the determination of the charge spectrum and a corresponding fit. It is forms the basis for the further analysis. This is explained in in sec. 2.3.2. Several difficulties and modifications are discussed. The results for the single intensity measurements are presented in sec. 2.3.3. A temperature dependence is investigated in sec. 2.3.4. The final results are discussed further ideas are suggested.

2.3.1 Data Processing

As already described in sec. 2.2.1, the LED was operated in pulsed mode and served as external trigger. The PMT signal has only been saved when the LED gave a trigger. The intensity of the LED was reduced until the mean number of detected photons was between 0 p.e. and 1 p.e. This results mainly in two different situations. Both are displayed in fig. 2.3 at the left. Most of the time, there will only be detected a noise signal. An exemplary waveform for such a situation is shown at the upper left in red. The PMT output voltage $U_{\text{pulse}}(t)$ is plotted versus the time t. Only a fluctuation around a mean value different from zero is measured. It is caused e.g. by leakage current as already discussed in sec. 1.4.4 and sec. 2.1. In some cases, there will be a LED signal detected. An example is visible in the same figure at the lower left. For clarity, the same time window is shown. At $t \approx 23\,\text{ns}$, a PMT pulse occurs. The PMT response can be expected to be located always at the same position with respect to the LED trigger as t_{trans} can be assumed to be small. This can also be confirmed by the data and is essential for the further analysis.

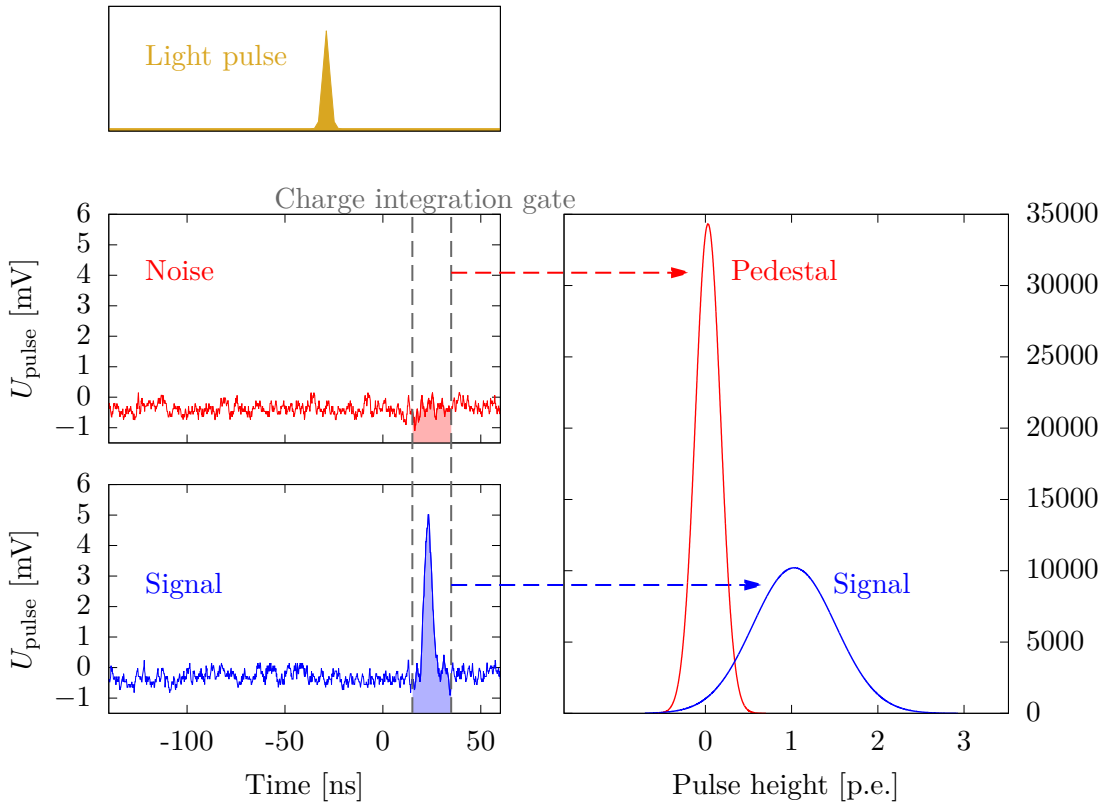

Figure 2.3: Exemplary illustration of the charge spectrum acquisition from the waveforms for low illumination and external trigger. *Left:* examples for waveforms with noise (above) and with a real signal (below). Both waveforms are integrated between 15 ns and 35 ns and the integral is plotted into the charge spectrum. *Right:* exemplary charge spectrum. The x-axis is normalised to the Q_1 value obtained for this certain measurement. Red shows the pedestal and blue the signal distribution.

As a next step, all data is integrated within the time window at which the PMT response typically occurs. A charge integration gate between 15 ns and 35 ns was chosen in order to avoid data loss for higher pulses. The integration includes real signal pulses as well as noise waveforms and was corrected simultaneously for baseline fluctuations. The datapoints before the occuring pulse were summed and subtracted from the total integral with a correction of the sampling rate at first. For a better statistic, the recording area of the baseline was chosen to be as large as possible. A corresponding charge spectrum is obtained in fig. 2.3 at the right. The integration provides two components. The first one is the pedestal from the noise integration. This is the dominating part. As the baseline was subtracted, it is located at 0 p.e. The second contribution is the light response at the 1 p.e. position. For larger intensities, additional signals appear at higher p.e. This yields the final charge spectrum to which the superposition of all single components is fitted. This approach is described in the next section.

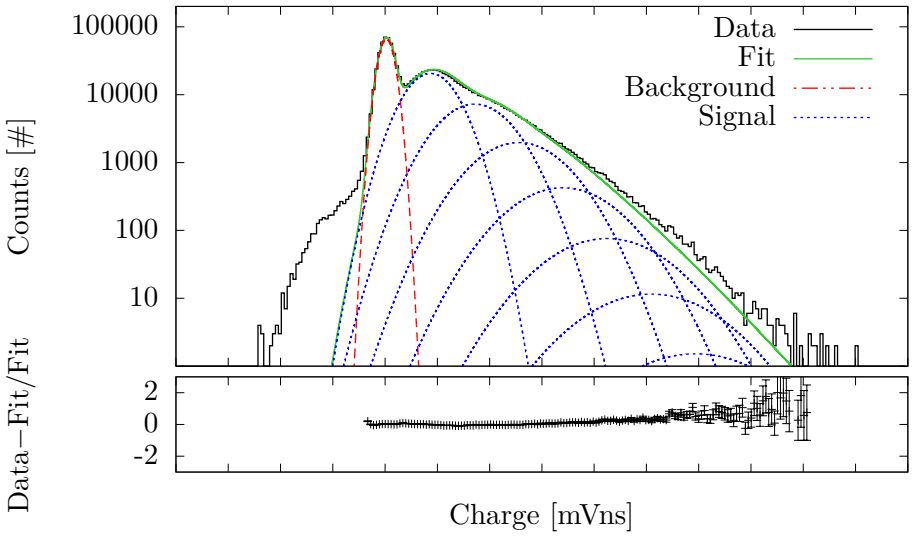

Figure 2.4: Exemplary charge spectrum for a measurement at 23 °C and $\mu \approx 1$. The fit of the spectrum and its single components are visible. A fit (green) of the form of eq. 2.7 was performed to the data (black). The dashed red curve corresponds to the background component and the dashed blue one to the light signal. The lower plot shows the residual of fit and data.

2.3.2 Fit Performance

A fit of eq. 2.7 was performed to the final spectrum. This was done via the programme ROOT. The allowed range of the eight fit parameters is limited to guarantee a stable fit behaviour. For instance, the probability parameter w is restricted between 0 and 1. Values outside this range do not have any physical meaning and are excluded. The spectrum was fitted from 6 bins to the left with respect to the maximum bin to the last bin above 1. In order to obtain a better fit performance, each fit is carried out 40 times in succession. The end parameters of each fit yield the starting parameters of the next one. This improves the fit in each step. A special fit routine of ROOT tests after finding a local minimum if there are further minima in proximity. This prevents the fit from running into a local minimum by mistake and it finds the global minimum. This yields a fit of the form visible in fig. 2.4. The histogram in black indicates the integrated data. In green, the final fit is shown. At the bottom, the residual of fit and data is plotted. The reduced χ^2_{red} is about 14.6. One can see the single components of the fit. The red line refers to the background contribution. This includes the pedestal represented by a Gaussian as well as the exponential function. The dotted blue curves are the single p.e. distributions. Figure 2.4 corresponds to a relatively large intensity measurement in which up to 7 p.e. are visible. Fit and data agree relatively good above a statistic of approximately 100 counts. Below, the deviation gets larger, but also the errors increase.

The prominent distribution at the left side of the charge spectrum has not been included into the fit. One would expect a straight decrease as shown from the background distribution. Because of this left distribution, it was not possible to fit the entire spectrum. A further problem is that the 1 p.e. as well as the 2 p.e. peak have a larger width than the pedestal. They are even more

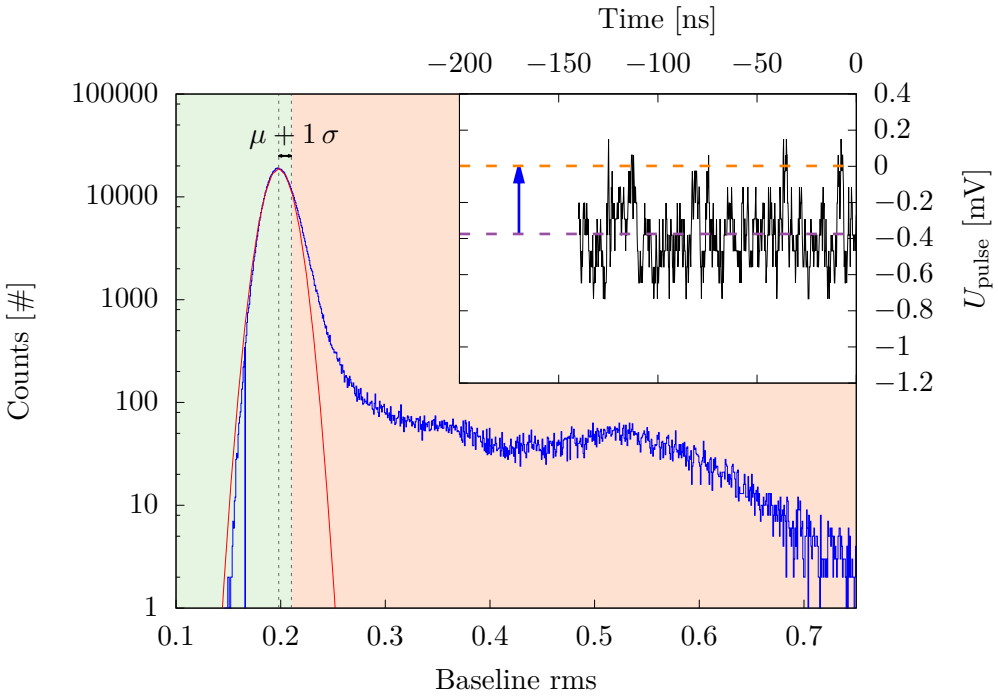

Figure 2.5: Histogram of the baseline rms before the pulse at 23 °C. An exemplary baseline before the pulse with its rms value indicated as blue arrow is plotted in the inlet. In blue, the distribution of the baseline rms is shown. It can be seen that most rms values are Gaussian-like distributed, but there is also an asymmetric distribution at the right with high fluctuations of the baseline.

extended at the left side. An idea to investigate the origin of this left distribution was to examine the distribution of the baseline root mean square (rms). It can be calculated via [89]:

$$u_{\text{rms}} = \sqrt{\frac{\sum_{i=1}^{n} u_{\text{i}}^2}{n}}\,, \tag{2.8}$$

in which u_{i} are the single voltage values within the baseline before the peak with n datapoints. When it is plotted into a histogram, one obtains the distribution shown in fig. 2.5. There is a peak larger than zero which is the most probable rms value. This distribution is Gaussian-like, but with a asymmetric edge at the right side towards larger values. There seem to occur additional waveforms with very high baseline rms values up to 1.4. This results into a second accumulation peak at about 0.55. The investigation of waveforms with such baseline rms values did not show a systematic difference from the outer appearance compared to other waveforms. They only possess larger noise fluctuations. Waveforms with such high baseline rms values were excluded from the charge spectrum. This was done in the following way as indicated in fig. 2.5. A Gaussian fit within an interval from 0.02 left and 0.015 right of the mode – the most probable value – is performed to the histogram of the baseline rms. All values higher than $\mu + 1\sigma$ were cut away. A detailed motivation of this criterion is given in sec. 2.3.5.1. The resulting consequences of this cut can be best seen for a measurement with no incident light which is shown in fig. 2.6. The corresponding charge spectrum is plotted without any cuts in fig. 2.6a. It shows a symmetric, non-Gaussian distribution around zero. The right accumulation can be accounted to a signal response by mistake. Figure 2.6b shows the same data after the application of a $1\,\sigma$-cut. Not only the odd distribution at the left end of the spectrum vanishes, but also the one at the right. Only the pedestal peak

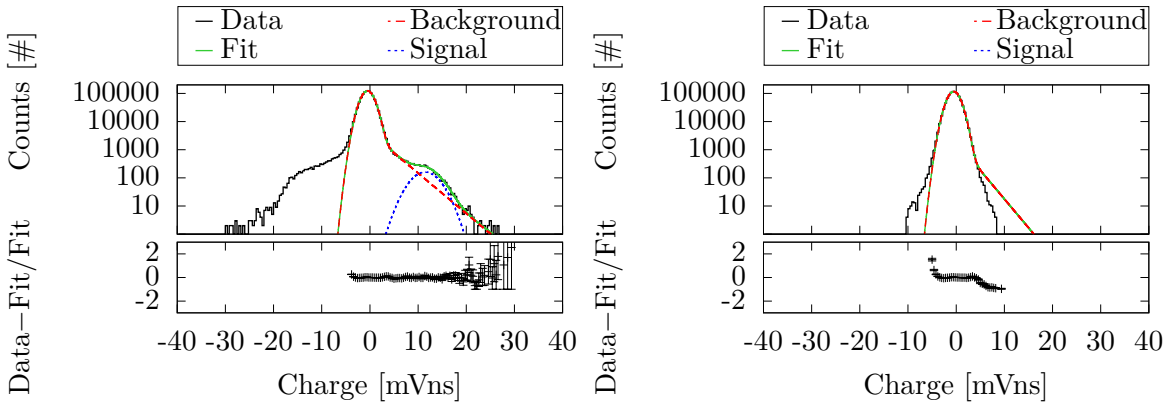

(a) Charge spectrum without any cuts. **(b)** Charge spectrum with $1\,\sigma$-cut.

Figure 2.6: Comparison of a charge spectrum without (a) and with (b) $1\,\sigma$ cut for a temperature of $-73\,°\mathrm{C}$ and no illumination. (a) shows an almost symmetric accumulation around zero of a non-Gaussian distribution. When the $1\,\sigma$ cut is applied, both accumulations disappear almost entirely and only the Gaussian-like pedestal is left.

remains. This indicates that the waveforms with large fluctuations distort the charge spectrum not only at the left but also at the right of the pedestal. With the $1\,\sigma$-cut, those could be eliminated. Further improvements are that the entire spectrum can be fitted and the χ^2_{red} could be reduced by a factor of two.

The $1\,\sigma$-cut did not resolve the problem that the width of the 1 p.e. peak σ_1 had to be strongly restricted which caused the fit parameter σ_1 to run into the upper limit. This imposes a severe problem. An idea was that fluctuations of the pedestal peak – described by σ_0 – also have impact on the signal itself. They were added to the signal distribution in the fit formula which is then modified to:

$$S_{\mathrm{real}} = \underbrace{\left[\frac{(1-w)}{\sqrt{2\pi}\sigma_0}\cdot\exp\left(-\frac{(x-Q_0)^2}{2\sigma_0^2}\right) + w\theta(x-Q_0)\cdot\alpha\mathrm{e}^{-\alpha(x-Q_0)}\right]\mathrm{e}^{-\mu}}_{\text{background}} + \underbrace{\sum_{n=1}^{\infty}\frac{\mu^n\cdot\mathrm{e}^{-\mu}}{n!}\cdot\frac{1}{\sqrt{2\pi n}\sigma_1+\sqrt{2\pi}\sigma_0}\cdot\exp\left(-\frac{1}{2}\left(\frac{x-Q_0-Q_{\mathrm{sh}}-nQ_1}{\sqrt{n}\sigma_1+\sigma_0}\right)^2\right)}_{\text{signal}}. \tag{2.9}$$

The terms marked in red refer to the modified parts compared to eq. 2.7. The fit of eq. 2.9 is more stable and the restriction of σ_1 has less often to be made. For the further analysis, eq. 2.9 was used.

2.3.3 Intensity Measurements

The measurement, data processing and fit as described in sec. 2.3.1 and 2.3.2 were performed for different temperatures and intensities. Figure 2.7 shows the value of Q_1 depending on μ which is proportional to the intensity of the incident light. It was measured for four different temperatures of 23°C, −9°C, −43°C and −73°C. The intensities are not the same for the different temperatures

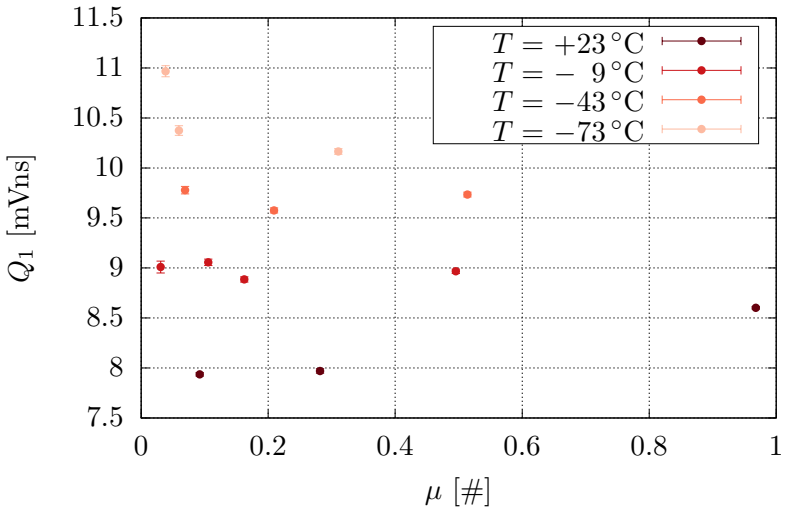

Figure 2.7: Q_1 in dependence on the intensity for different temperatures. The errors come from the fit. Q_1 is approximately the same for one temperature. But the different temperature curves vary with their mean value. On average, Q_1 seems to increase for lower temperatures.

because such an adjustment was not feasible with the used pulse generator. In addition to that, the LED was in the climate chamber as well and the IV-characteristic is highly temperature dependent. Both reasons make the adjustment of exactly the same output intensity of the LED impossible. It was possible to adjust approximately the same intensity region between a μ of 0 p.e. and 1 p.e. manually. The value of Q_1 is approximately the same within one temperature regardless of the intensity, but there seems to be a temperature dependence. The different temperature curves are shifted to higher Q_1 values for lower temperatures. This effect is investigated in the next section in more detail.

2.3.4 Temperature Dependency

In order to find a possible temperature dependence of the Q_1 value, Q_1 is plotted versus the temperature T. The weighted mean of all Q_1 values for one temperature is calculated from the different intensities. This is done via the formula for the case of unequal standard deviations σ_1 [89]:

$$\overline{Q}_1 = \frac{\sum_{i=1}^{n} \frac{Q_{1,i}}{\sigma_{1,i}^2}}{\sum_{i=1}^{n} \frac{1}{\sigma_{1,i}^2}} \qquad \text{with} \qquad \overline{\sigma_1} = \sqrt{\frac{1}{\sum_{i=1}^{n} \frac{1}{\sigma_{1,i}^2}}}\,, \tag{2.10}$$

where $\overline{Q}_1$ denotes the weighted mean of the Q_1 value for one temperature, $Q_{1,i}$ the ith Q_1 value, $\sigma_{1,i}$ the corresponding σ_1 value and $\overline{\sigma_1}$ the uncertainty on the weighted mean itself. The results are plotted in fig. 2.8 depending on T. Q_1 increases for lower temperatures. As for later characterisations the Q_1 value at $T = -100\,°C$ is of particular interest, it is extracted from the data. A linear fit is applied to the data including their error with a further extrapolation to $-100\,°C$. This yields a Q_1 value of about (10.9 ± 0.1) mVns.

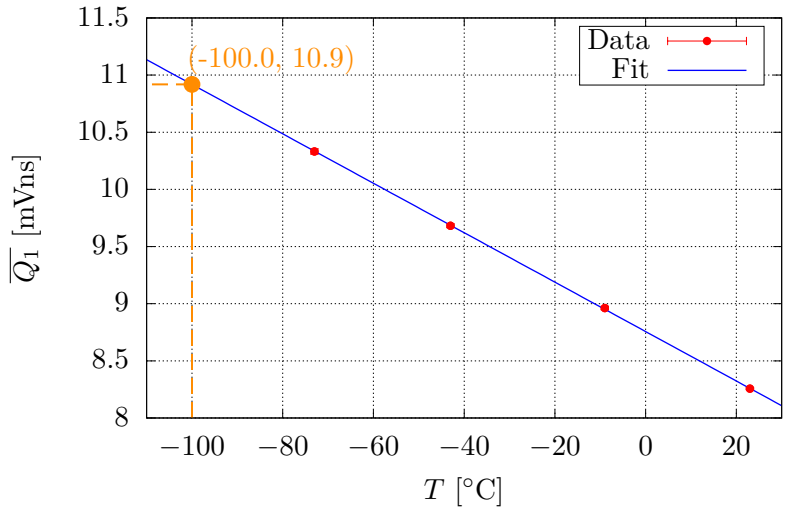

Figure 2.8: Weighted mean value for Q_1 in dependence on the temperature. The errorbars originate from the error of the weighted mean. In blue, a linear fit to the data with corresponding extrapolation to $-100\,°C$ is plotted.

2.3.5 Further Analysis

Some additional analysis details and further motivation for the implemented data processing steps are given in this section. This includes the investigation of several possible cuts to the baseline rms as for example $1\,\sigma$, $2\,\sigma$ etc. and the justification of the finally used $1\,\sigma$-cut. Several fit parameters as well as the reduced χ^2 of the normal fit model are compared to the ones of the modified one. A closer consideration of some of the parameters describing the background reveal further insight to the goodness of the fit. Finally, the resolution of each measurement is determined.

2.3.5.1 Different Cuts

Different cuts to the baseline rms were investigated to reduce the noise in the charge spectrum. This was done for the fit model of eq. 2.7. For the final analysis, the $1\,\sigma$-cut was used. In the following, the different cuts and their consequences on several fit parameters are discussed.

One of the most important parameters describing the goodness of a fit is the χ^2_{red}. It is the ratio of the χ^2 and the degrees of freedom n_{F}. The χ^2 is the sum of the squared differences of data and fit divided by the squared error of each datapoint. n_{F} is the difference of the number of datapoints and the number of fitted parameters. For a succesful fit, χ^2_{red} should be close to one [90, 91]. In case $\chi^2_{\text{red}} \gg 1$, it indicates that the fit function does not describe the data very well. For the case of $\chi^2_{\text{red}} \ll 1$, it is most likely that the measurement uncertainties were overestimated. Figure 2.9 shows the χ^2_{red} for different cuts measured for different intensities I with $I_1 < I_2 < I_3 < I_4$. The different σ-cuts indicate how large the maximal baseline rms is allowed to be. $0\,\sigma$ means that all data to the right of the maximum μ are excluded from the fit, $1\,\sigma$ that all to the right of $\mu + 1\,\sigma$ and so on. ∞ refers to the fit without any cuts. On average, χ^2_{red} decreases for more stringent cut limits. The lower the intensity is, the extremer is this effect. For the lowest intensity, χ^2_{red} decreases from 10 to 2. This indicates that the large baseline rms values falsify the charge spectrum in such a way that the fit cannot be applied appropriately any more. A suitable cut is fundamental for a

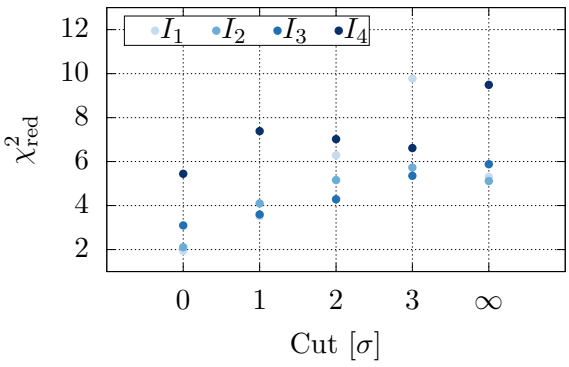

Figure 2.9: χ^2_{red} depending on the application of different cuts for different intensities. The measurement was performed for $T = -9\,°\text{C}$.

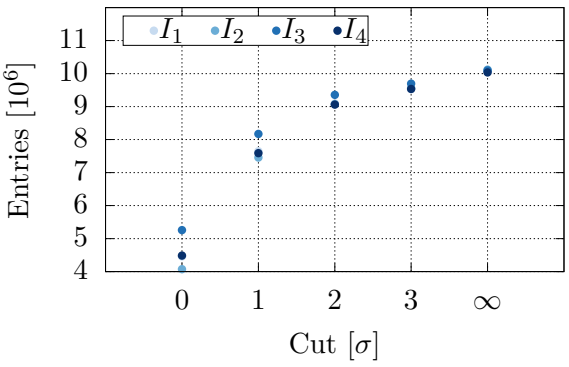

Figure 2.10: Number of entries in the histogram in dependence on the different cuts for different intensities. The same data as in fig. 2.9 are used.

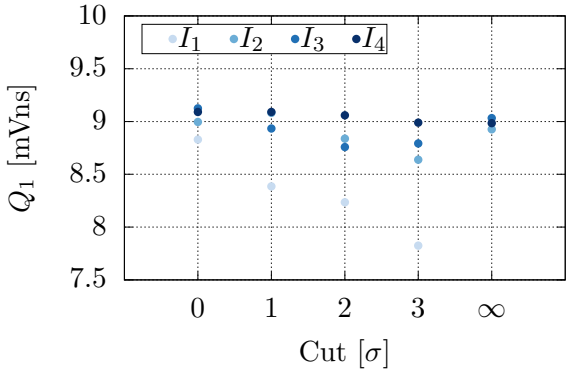

Figure 2.11: Q_1 versus different cuts for several intensities at $T = -9\,°\text{C}$. The normal fit model was used.

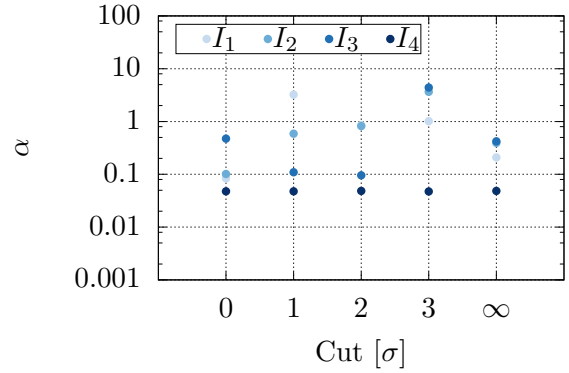

Figure 2.12: α depending on different cuts for several intensities at $T = -9\,°\text{C}$ for the normal fit model.

succesful fit. For the fit without any cuts, the χ^2_{red} is lower suggesting a better fit result than for instance the $3\,\sigma$-cut. This is because not the entire fitrange – as for all other cuts – was used.

The strong σ-cuts also have a downside. This refers to the remaining statistics of the data. More stringent cuts also mean that less datapoints are left in the spectrum. Figure 2.10 shows the number n of entries depending on the different cuts for the same measurement as in fig. 2.9. n decreases rapidly for stronger cuts regardless of the intensity. The most prominent drop can be noticed between the $0\,\sigma$- and the $1\,\sigma$-cut. In this region, most data are lost whereas the χ^2_{red} does not increase in this extent. For this reason, the $1\,\sigma$-cut was considered as the best trade-off.

Another aspect are the fit results for signal and background components depending on the cut. In fig. 2.11, Q_1 depending on the cut is visible for different intensities. It shows that the value of Q_1 is almost unchanged for higher intensities. In the case of I_4, Q_1 lies around 9 mVns with no large fluctuations. This is different for I_1. It decreases from around 9 mVns to about 7.7 mVns showing a very unstable behaviour. This can be explained by noise contributions from waveforms with large baseline rms values. Q_1 should be constant for one intensity. The fluctuation decreases for more stringent baseline cuts.

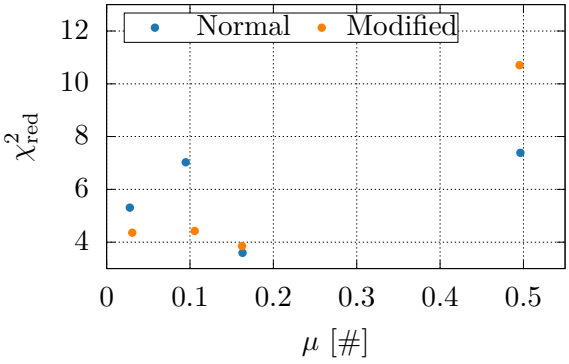

Figure 2.13: χ^2_{red} versus μ corresponding to the intensity for normal and modified fit formula. The data are taken at $T = -9\,^{\circ}\text{C}$. and the $1\,\sigma$-cut was applied.

The larger fluctuations from waveforms with large baseline rms values are not only visible in the signal, but also in the background contribution. This can be seen in fig. 2.12. It shows the parameter α, which describes the exponential decay of type II background processes, in dependence on the cut. The same measurement is shown as in fig. 2.11. For higher intensities, the fit parameter α is more stable. The lower the intensities get, the larger the fluctuations become. It shows that the fit does not work very stable especially for low intensities. This may indicate that the fit model does not describe the type II background processes appropriately. As its contribution is far larger for low intensities, it mainly disturbs low intensity fits.

2.3.5.2 Comparison of Fit Models

For a more stable fit behaviour, the modified fit of eq. 2.9 was used for the analysis. It also reduced the χ^2_{red}. This can be seen in fig. 2.13. It shows χ^2_{red} versus μ for the normal model from eq. 2.7 and the modified model from eq. 2.9. The measurement was made at $T = -9\,^{\circ}\text{C}$. Especially for low intensities, the χ^2_{red} is very low and stable. For higher intensities, χ^2_{red} increases. This behaviour can be observed for every temperature.

The more stable fit behaviour can be also observed concerning the Q_1 value. This is visible in fig. 2.14. The same dataset as in fig. 2.13 is plotted. The deviation of Q_1 for different intensities is much smaller for the modified model and the error on the weighted mean is reduced. The values for Q_1 seem to be decreased in case of the modified fit. This may indicate an overestimation of the Q_1 in case of the normal fit which may be caused by the unknown contribution of the type II background processes. The strong deviation of normal and modified model especially for low intensities confirms this suspicion.

Figure 2.15 shows one of the most significant differences between normal and modified fit. Due to the additional contribution of σ_0 to the signal width, σ_1 becomes smaller. One can also observe smaller fluctuations and more stability for the modified model compared to the normal one. The errors of the normal model are so extremely small because the fit run into the limitation which had to be made in order to obtain a reasonable fit.

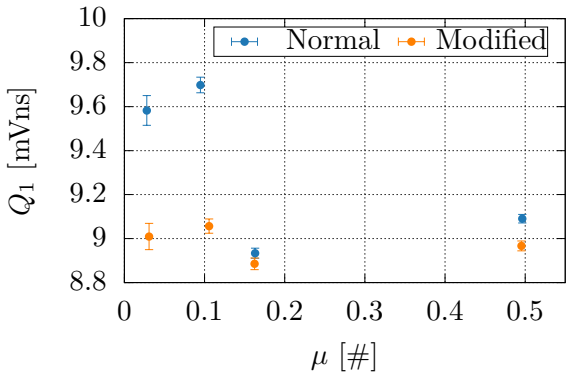

Figure 2.14: Q_1 depending on the intensity for normal and modified fit formula. The dataset was measured at $T = -9\,°\mathrm{C}$ and the $1\,\sigma$-cut was applied.

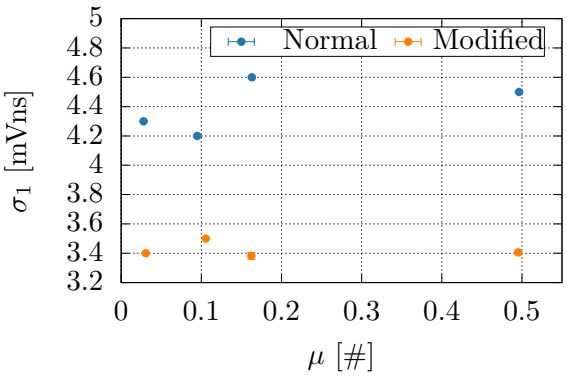

Figure 2.15: σ_1 in dependence on the intensity for both normal and modified fit formula.

2.3.5.3 Background Parameters

The intensity dependence cannot only be performed for Q_1 but also for other parameters. This refers for instance to the fit parameters describing the background distributions. One of them is Q_0. Figure 2.16 shows Q_0 in dependence on the intensity for different temperatures in case of the modified model and a $1\,\sigma$-cut. Similar to Q_1, it is almost constant over the intensity. But it decreases for lower temperatures. This effect can be explained by the decrease of electronic noise when cooling down which reduces Q_0.

This is different for background type II proccesses. They are described by the parameters α and w. Both are plotted in fig. 2.17 and fig. 2.18, respectively. As the two parameters occur as a product in the fit formula, they have a contrary behaviour. An increase of α results into a decrease in w and vice versa. This can also be observed in the plots. Figure 2.17 shows α depending on the intensity for different temperatures. Regardless of the temperature, it can be seen that α is relatively large for low intensities and decreases for larger ones. This refers to a large contribution of the exponential function for low intensities which is decreasing for higher ones. Background proccesses of type II have a higher contribution for low intensities. This is also what one would expect.

A contrary behaviour yields fig. 2.18. It depicts w depending on the intensity for different temperatures. For lower intensities, the probability is smaller than for larger ones. The reason is that background type II proccesses are always accompanying a real signal. For larger intensities, there are more photons emitted and thus more signals detected. This increases w.

2.3.5.4 Resolution

The resolution is one of the parameters descibing a single electron spectrum. It is obtained by the division of the FWHM by its position which is Q_1. It is calculated via the formula [65, 92]:

$$\text{resolution} = \frac{2 \cdot \sqrt{2\ln(2)} \cdot \sigma_1}{Q_1}\,. \tag{2.11}$$

Figure 2.19 shows the resolution depending on the intensity for different temperatures. On average, it is about 0.9. For the two most extreme temperatures, there are larger deviations. For $T = +23\,°\mathrm{C}$,

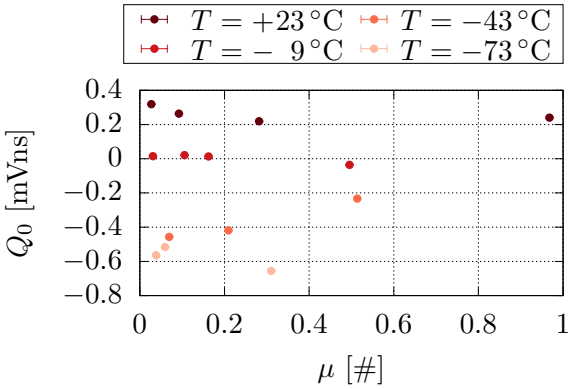

Figure 2.16: Q_0 versus the intensity for different temperatures. For all datapoints, the modified fit model as well as the $1\,\sigma$-cut were applied.

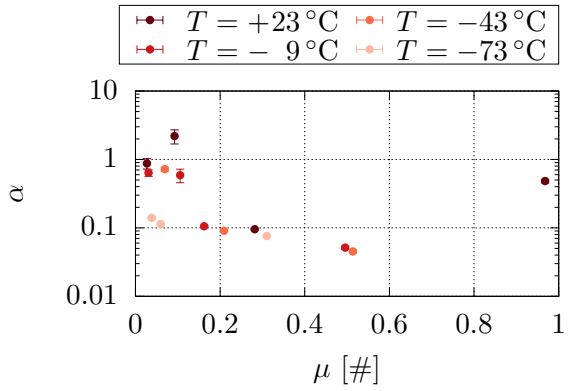

Figure 2.17: α depending on the intensity for several temperatures. Measurement with applied $1\,\sigma$-cut and modified fit formula.

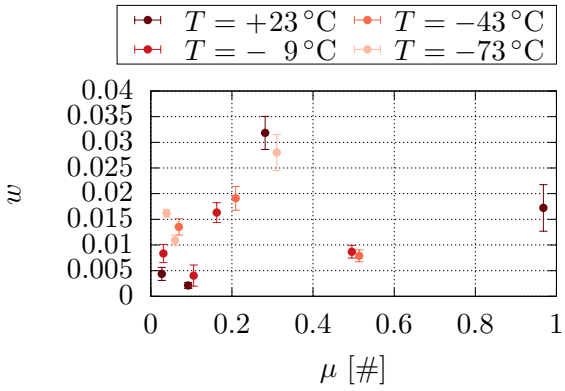

Figure 2.18: Probability w for an accompanied background process of type II versus the intensity for distinct temperatures. $1\,\sigma$-cut and modified fit formula were used.

it decreases rapidly with increasing intensity from about 1.1 to approximately 0.8. The contrary behaviour can be observed for $T = -73\,°\mathrm{C}$. The resolution increases from 0.73 to 0.9. Since the large deviations from the average value primarily occur for very low intensities, the unsufficient description of the type II background processes may be the reason for this.

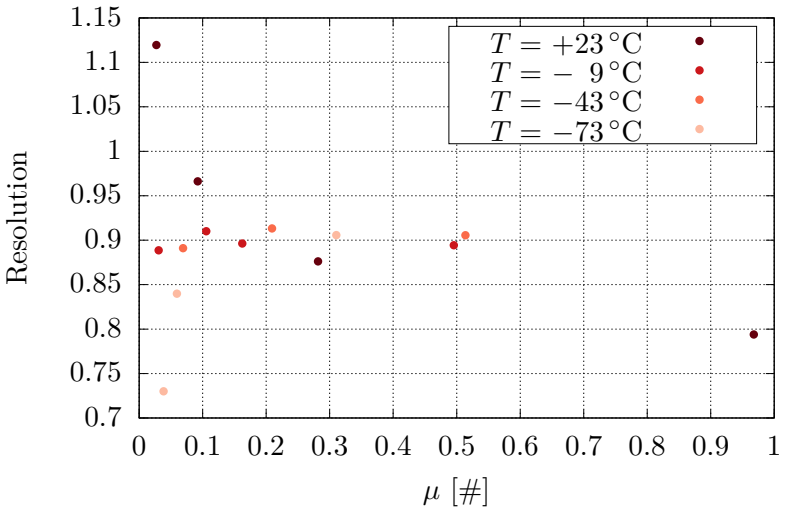

Figure 2.19: Resolution depending on the intensity for several temperatures. On average, the resolution is about 0.9 for most datasets.

2.4 Results and Discussion

Within the scope of this work, an absolute calibration of a PMT R8520-406 was realised at cryogenic temperatures. A pulsed LED was used as a light source. The operation of the LED inside the climate chamber yields the problem of electric coupling between LED and PMT. An example is visible in fig. 2.20. It displays a typical noise waveform for a temperature of 23 °C (fig. 2.20a) and −73 °C (fig. 2.20b). For fig. 2.20a, only fluctuations around a mean value are visible. But for a low temperature such as in fig. 2.20b, an oscillation at the position at which the signal typically appears is visible. This oscillation appears for every waveform and only for the measurements at −73 °C and −43 °C with a larger amplitude for −73 °C. A possible explanation is the temperature dependent change of the resistances and capacities of the electronic components of both PMT and LED. Their performance is optimised for room temperature. When the PMT is cooled down, the resistances and capacities are altered, thus changing the resonace frequency of the circuits. Figure 2.20b indicates a temperature dependent electronical coupling of PMT and LED. A possible solution would be to place the LED outside the climate chamber and guide the light inside through an optical fibre.

A fit of the form of eq. 2.9 was applied to the charge spectrum in order to determine Q_1. Although the absolute calibration of the PMT was possible, there were several difficulties and limitations to the analysis itself. The fit behaviour was not always stable. A tiny alteration in the starting conditions resulted into completely different fit results. This includes changes in binning of the spectrum, number of fitted p.e., start parameters, limits of the parameters, fitrange and applied cuts. Within the scope of this work, not all possible fit configurations could be investigated. There is still potential to optimise the fit conditions and obtain a better fit result and χ^2_{red}. The start parameters have the most stringent impact on the convergence of the fit. The parameter σ_1 imposed the major problem. Its upper limit had to be firmly restricted. The manual adjustment mainly determined the value of σ_1. This problem could be partially solved by using the modified fit function from eq. 2.9. But the problem persisted especially for lower intensities. Low intensities

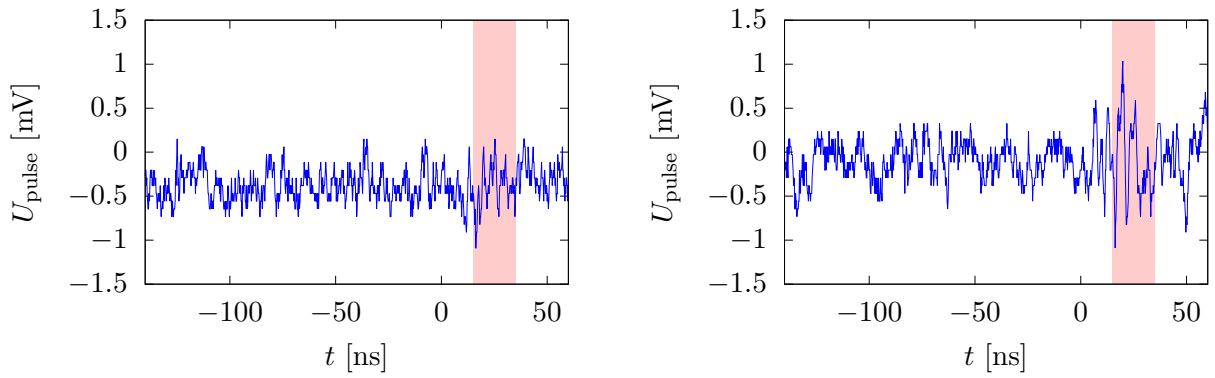

(a) No oscillation. **(b)** Oscillation.

Figure 2.20: Exemplary noise signal at 23 °C without any abnormal behaviour (a) and noise signal at -73 °C (b). It shows an oscillation exactly within the charge integration gate (red) where all PMT pulses occur. The oscillation is only apparent for measurements at -43 °C and -73 °C and always appear at the same position. This indicates an electronic coupling of LED and PMT.

further yield the problem that the contribution of the exponential background function is extremely large compared to the real signal. A restriction of α towards higher values made a fit impossible. This indicates that especially for low intensities, there are contributions which cannot be descibed only by the Gaussian functions for pedestal and signal and make the exponential function necessary. The fit problems during this work suggest that the model of [78] does not describe the charge spectrum entirely. This may be because the approximation of eq. 2.5 was used which is only valid for a small noise intensity and illumination intensities higher than $\mu > 2$ [78] . Both conditions are strictly speaking not given in this work. A possible solution would be to fit the non-simlplified version of eq. 2.7.

Despite these problems, the fit was found to describe the data sufficiently so that the charge value for Q_1 could be determined for different intensities and temperatures. A temperature dependence of the Q_1 value was found resulting directly into a temperature dependence of the gain. Both increase for lower temperatures. A temperature dependence of the gain is indeed predicted for bialkali PMTs from literature. There are two different trends in opposite directions. Firstly, the QE increases for a decreasing temperature. This is because the generation of optical phonons is suppressed for low temperatures and energy losses of the photoelectrons in the photocathode are reduced which results in an increase of the gain. Various temperature dependent measurements of the QE have already been performed by different groups confirming an increase of the QE for lower temperatures [93, 94]. This trend has also been observed for the PMT model used in this work by E. Aprile et al. who measured a relative increase of the QE of about 10 % from room temperature to −100 °C [95]. Another effect is that the coefficent of secondary electron emission at the dynodes increases for lower temperatures [93]. Both increase QE and δ yielding an enhancement of the gain and Q_1 for lower temperatures. Secondly, there was another trend observed reducing the gain for a lower temperature. This is because the resistance of the cathode material as well as the one of the dynodes change with temperature altering the electric field between the dynodes for a constant supply voltage. As the capacities and resistances of a PMT are typically optimised

for room temperature, variations in the electric field commonly lead to a decline in the CE at the dynodes and the gain for lower temperatures. This was measured by M. Prata et al. [96]. For this work, a linear extrapolation was found to describe the data sufficiently. The Q_1 value for $-100\,°\mathrm{C}$ could be determined to be $(10.9 \pm 0.1)\,\mathrm{mVns}$. This value is consistent with the result of [97] which is about 8 mVns at $-98\,°\mathrm{C}$ for another PMT of the same series.

Chapter 3

Characterisation of a SiPM in the Absence of Light

With regard to the characterisation of a SiPM, measurements in the absence of light already yield most of the relevant parameters. These include for instance noise, gain and the breakdown voltage. In this chapter, a description of the setup used in this work is given. The applied data processing and analysis procedure is explained. The main part forms the presentation and discussion of the characteristic properties of the used SiPM.

3.1 Setup

The measurements have to be performed at −100 °C which makes the implementation for example in a commercial climate chamber impossible. In addition to that, the setup was built for measurements with LXe. Only high purity components such as polytetrafluoroethylene (PTFE), copper and aluminium are used to minimise contaminations from outgassing materials. The required thermal insulation from the outside also includes the requirement of special feedthroughs for the electronic. In the subsequent sections, the setup used in this work is described in more detail.

3.1.1 Entire Setup

A schematic block diagram of the entire setup is depicted in fig. 3.1. There are four main components which are the cryostat, the gas system, the temperature control system and the electronic system. The different parts are described in the following in more detail.

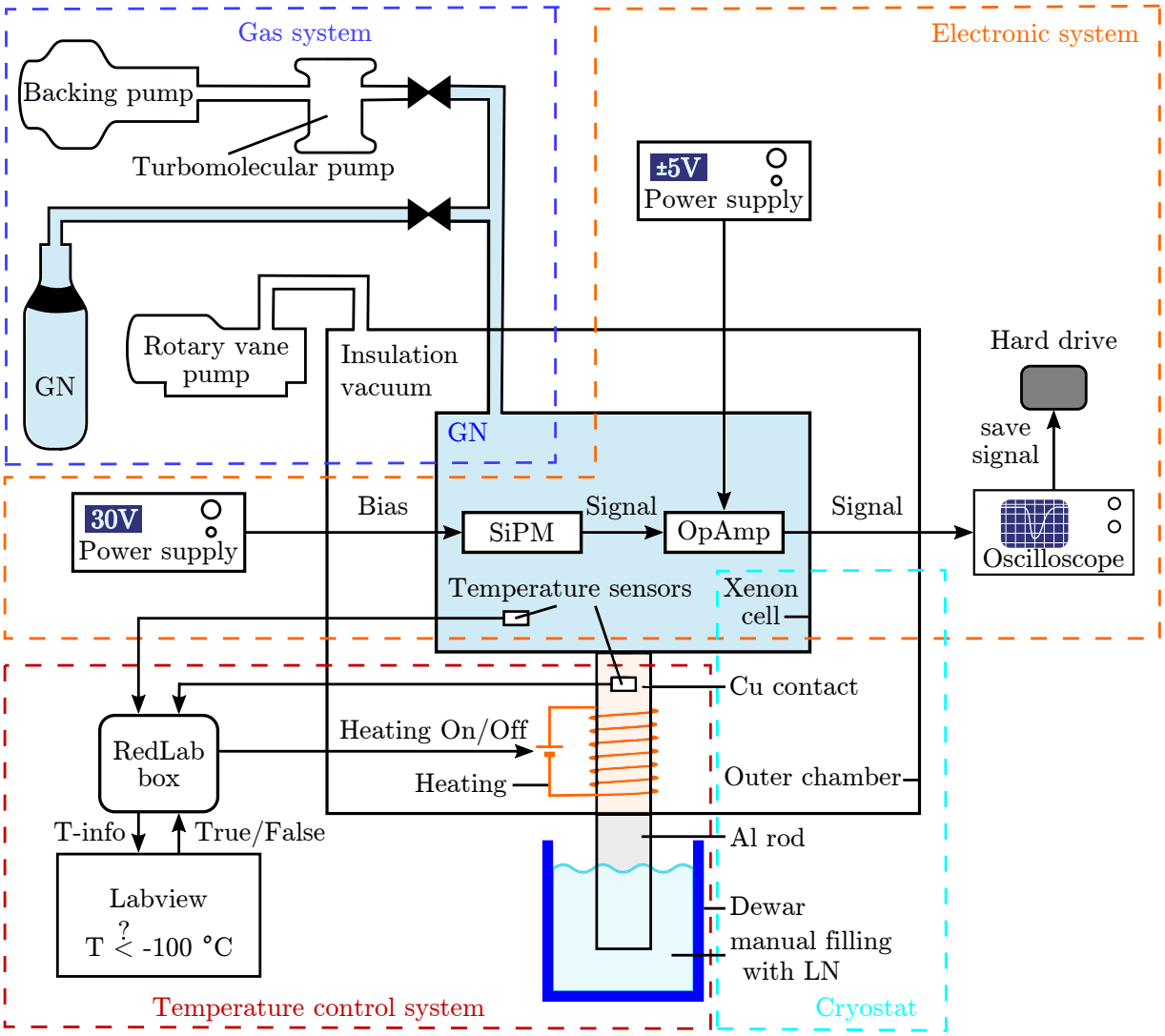

Figure 3.1: Simplified block diagram of the entire setup.

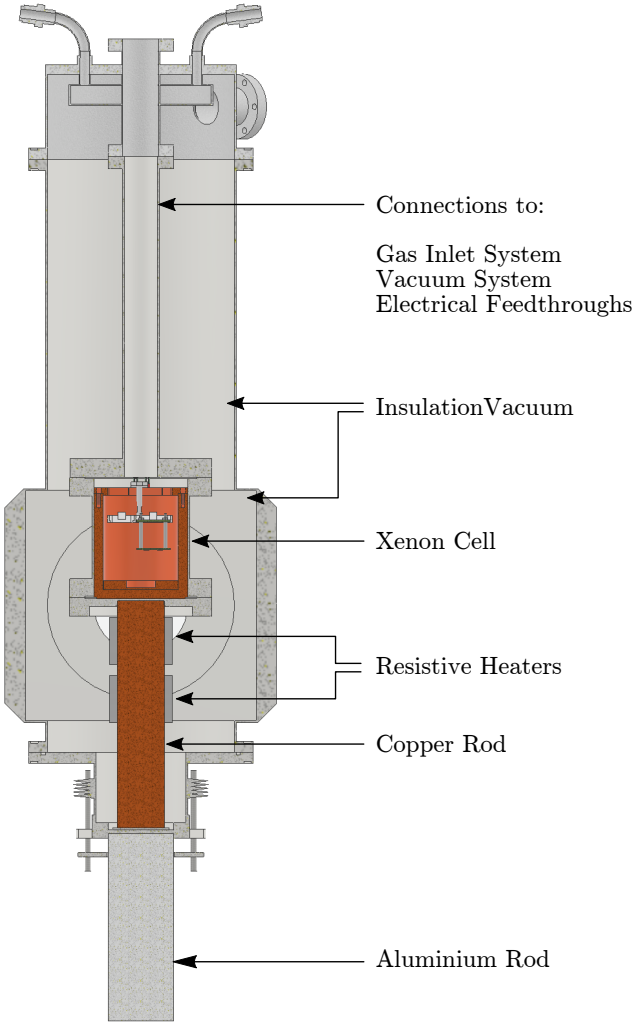

Figure 3.2: CAD drawing of the cryostat. It mainly consists of the xenon cell and the outer chamber. The connections to the gas system as well as the electrical feedthroughs are positioned at the top. A copper and aluminium rod represent the cooling contacts below the xenon cell. Resistive heaters are installed at the copper rod to regulate the temperature.

3.1.2 Cryostat

A CAD drawing of the cryostat is shown in fig. 3.2. It consists of an inner and an outer chamber. The former one is called xenon cell and forms the part of the setup in which the measurements are performed. It consists of a steel cylinder with a thickness of 2 mm at the bottom. For a better temperature mixing, a copper cup is placed inside. Three temperature sensors are arranged between the steel wall of the inner cell and the copper cup at different heights (top, middle and bottom). At the top of the copper cup, the holding for the detector is mounted. It is made of PTFE due to purity reasons. The top of the xenon cell is directly connected via a steel tube to the gas inlet- and vacuum system as well as to the electrical feedthroughs. A copper rod represents the cooling contact at the outer bottom of the inner cell. A heating is installed around this rod which is described in more detail in sec. 3.1.4. Another temperature sensor is placed onto the rod.

Its bottom is in thermal contact with the inner bottom of the outer chamber. An aluminium rod is fixed at the outer bottom of the outer chamber. It is directly immersed into a dewar filled with liquid nitrogen (LN). The outer chamber only serves as insulation vacuum to minimise heat inputs from outside. It also contains electrical feedthroughs of the heating and an additional connection to the vacuum system. A more detailed description of the cryostat can be found in [97].

3.1.3 Gas System

The gas system is connected to the top of the cryostat and has two subsystems. One is for the outer chamber and another for the xenon cell. The subsystem for the outer chamber basically consists of an oil-guided slide vane rotary vacuum pump from the company EDWARDS [98] ensuring an insulation vacuum of about 3×10^{-4} bar. The pump is operated during the entire measurement. In contrast to that, the subsystem for the xenon cell consists of more parts. On the one hand, there is the vacuum system containing two vacuum pumps and on the other hand, there is a gas inlet system. The two vacuum pumps are responsible for the evacuation of the inner chamber. Its necessity is explained in sec. 3.2. Firstly, there is the backing pump consisting in an oil-free dry scroll pump from the company BOC EDWARDS [99]. Its task is to evacuate the xenon cell so that the second pump can be turned on. This is a turbomolecular pump from the company PFEIFFER [100] capable of reaching a pressure of about 2×10^{-8} bar. A gas cylinder is connected to the xenon cell providing measurements in a gaseous atmosphere. For the measurement in this chapter, it is one filled with gaseous nitrogen (GN). For a thorough overview of the construction and working principle of the complete gas system, see [97].

3.1.4 Temperature Control System

The task of the temperature control system is to ensure a stable temperature of $-100\,^{\circ}\mathrm{C}$ at the SiPM over time. It includes different components. Firstly, the actual cooling system. This is mainly formed by a dewar manually filled with LN. An aluminium rod is immersed presenting the cooling contact to the outer chamber. A copper rod inside the outer chamber serves as the cooling contact to the xenon cell. All contacts of the chamber and the rods are filled with indium to ensure a better thermal contact. As the average temperature of LN is lower than -196 °C under normal pressure [101], an additional heating has to be installed to keep the temperature at the SiPM stable at $-100\,^{\circ}\mathrm{C}$. This is the second component of the temperature control system. The heating is formed by a resistor chain wrapped around the copper rod. A constant current through the chain causes the resistors to heat up. This heat is then transferred to the copper rod. The actual temperature control is performed by means of the temperature sensors and a LABVIEW programme. There are five temperature sensors in total. Three of them are placed at the outside of the copper cup in grooves at different positions. They serve as additional monitoring information. The two remaining temperature sensors are the most relevant for the actual control as one is used as trigger for the heating and the other displays the temperature at the SiPM. The trigger sensor is arranged at the copper rod and the sensor for monitoring onto the SiPM holder near the SiPM itself. The temperature sensors are Thin Film Platinum Resistance Temperature Detectors (RTDs) of the HEL-700 series from the company HONEYWELL [102]. Depending on the temperature, they output a different voltage which is then converted to a temperature. This happens via a RedLab 3104 box from MEILHAUS ELECTRONIC GMBH [103]. It collects the information of all temperature sensor and passes them as a temperature information to the LABVIEW programme on a computer.

It displays the temperatures of the different sensors and regulates the heating. For this purpose, the sensor on the copper rod is used as trigger. A temperature request is performed within the Labview programme. In case the temperature measured by the sensor on the copper rod is lower than $-100\,°C$, a certain signal is given to the RedLab box which then switches on the heating. If it is larger than $-100\,°C$, another signal is returned to the box causing the heating to switch off. In this way, the temperature is regulated to constant value of $-100\,°C$ at the SiPM. The entire heating system and temperature control was built by P. Hufschmidt within the scope of his master's thesis [97].

3.1.5 Electronic System

The electronic system is mainly responsible for the data aquisition procedure. A constant bias is applied to the SiPM via a power supply from the company iseg [82]. The raw output signal of the SiPM is passed on to two operational amplifier (OpAmps) enhancing the signal by a factor of about 100. A detailed circuit diagram of the OpAmps is explained in sec. 3.1.6. Each OpAmp is provided with a constant voltage of $\pm 5\,V$ from a power supply of the company Hewlett Packard [104]. The amplified signal is passed on to an oscilloscope from the company LeCroy [85] where the data is stored onto a hard drive. Only the SiPM and the OpAmp are installed within the xenon cell and cooled down to $-100\,°C$. All other devices are located outside the cryostat. The bias of the SiPM as well as the supply voltage of the OpAmp and the output signal are lead in or out, respectively, by electrical feedthroughs installed at the top of the cryostat. It has to be noted that all electric lines except the ones onto the amplifier board are shielded. A PTFE coating is used for the cables inside the xenon cell.

3.1.6 SiPM and Operational Amplifier

A SiPM from the company FBK with the labelling FBK VUV-HD LF was used in this work. The term "VUV" refers to the sensitivity in the ultraviolet region (vacuum ultraviolet) of the SiPM required for the nEXO experiment. The entire SiPM has a size of $6 \times 6\,mm^2$ and is subdivided into four $3 \times 3\,mm^2$ quads. A different doping profile compared to the standard one results in a larger U_{break} and is described by the abbreviation for low field (LF). The SiPM originates from a series of wafers exclusively fabricated for the nEXO collaboration for testing purposes. A SiPM processed from a wafer subsequently labelled as W9 was used in this work. Its (x,y) position onto the wafer is named as (7,6). A schematic view of the wafer with its corresponding positions is depicted in fig. 3.3. The empty spaces indicate unallocated positions. In black, the damaged devices are shown. Only the coloured rectangles refer to the relevant wafer positions. The wafer position of the SiPM used in this work is depicted in red. The SiPM at (3,6) was measured by T. Ziegler [105], the SiPMs at (18,3) and at (1,13) by A. Jamil [106]. Their results are compared to the ones obtained in this work.

A photograph of the SiPM together with its amplifier board is depcited in fig. 3.5. At the top, a board is shown on which the SiPMs can be arranged. The single SiPMs are glued with an epoxy from Polytec EC 101 [107] onto the board. It is hardened in a furnace at $80\,°C$. After that, the contact pads at the surface of the SiPM are connected to the board. This is realised by aluminium wires with $25\,\mu m$ in diameter which are bonded onto the SiPM pad and the board pad [1]. Figure 3.4

[1] Glueing and wire bonding have been done by Gerhard Tischlinger from the Fraunhofer ICS.

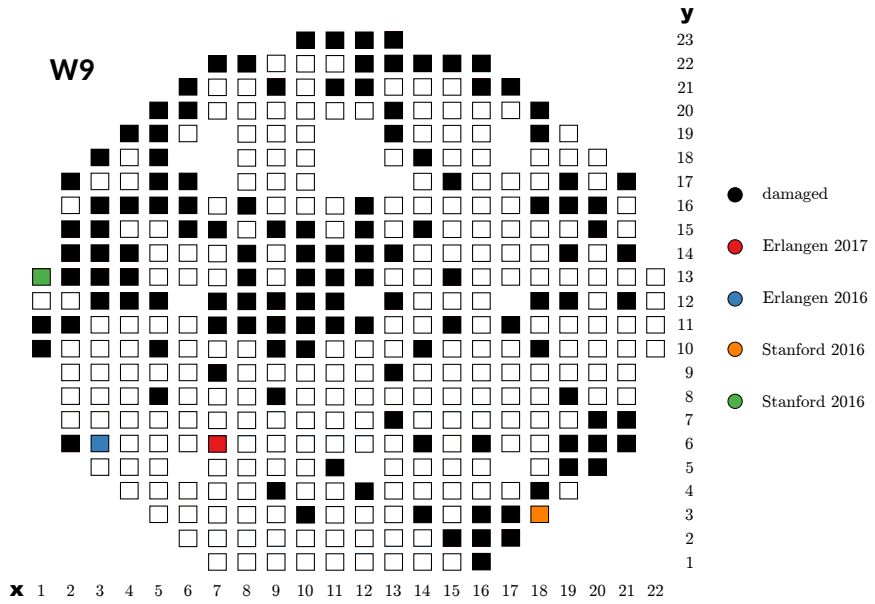

Figure 3.3: Wafer W9 with the corresponding positions of the single SiPMs. A (x,y) matrix illustrates the exact wafer position of the individual pieces. The empty spots are from not used positions. In black, the devices found as damaged after the fabrication process are depicted. The red rectangle corresponds to the SiPM tested within this work. The other three coloured devices refer to further devices used for comparison. Adapted from [27].

shows a picture of the SiPM with bonding. An electric contact is installed from the board pad to the backside of the board connected to the amplifier board by SAMTEC-connectors which can be seen in fig. 3.5. The two boards are kept together via four long screws separated by four PTFE spacers for electrical insulation. At the backside of the amplifier board, the bias as well as the output signal connections are located.

The entire circuit diagram of the OpAmps is shown in fig. 3.6. The amplifier circuit consists of two OpAmps, thus providing an amplification in two stages. They are from the company ANALOG DEVICES from the ADA4895-1ARZ series [108]. Both are operated as inverting amplifiers. The SiPM is placed at the marked position. One pin is connected to the bias via a low-pass filter to eliminate high frequency disturbances. The other one feeds the SiPM signal directly into the first amplifier. The signal was filtered before by means of a high-pass filter and a bandpass one. The amplifier output is not only coupled to the input via a resistance specifying the amplification factor, but also in parallel with a capacitor. Its purpose is to reduce the amplification of very high frequencies. The output of the first amplifier is then connected to the input of the second one which is identical to the first one. Each possesses an amplification factor of -10. An amplification of about 100 is obtained alltogether. Each OpAmp is supplied with a voltage of $\pm 5\,\mathrm{V}$ as shown in the circuit diagram. The remaining capacitors have the task to smooth the supply voltage and minimise electronic noise. At the end, the impedance of the amplified signal is adjusted with a $50\,\Omega$ terminating resistor to the remaining connections and the signal is tapped. The exact realisation onto the amplifier board is shown on the lower lefthand side of fig. 3.6.

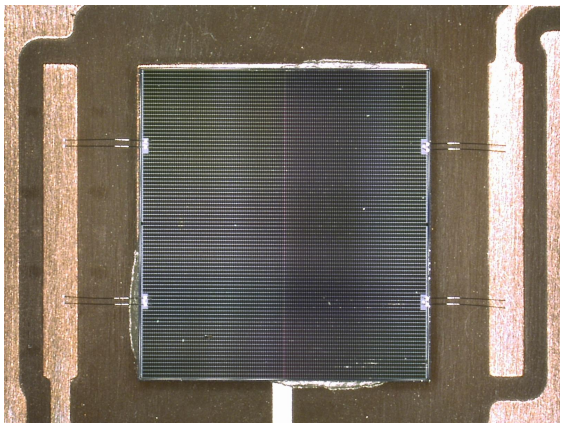

Figure 3.4: Photograph of the SiPM used in this work. It is a VUV sensitive SiPM from FBK with a total area of $6 \times 6\,\mathrm{mm}^2$. It is glued onto a mounting board. The electric contacts are represented by 25 µm thick wirebonds attached to both board pads and SiPM pads.

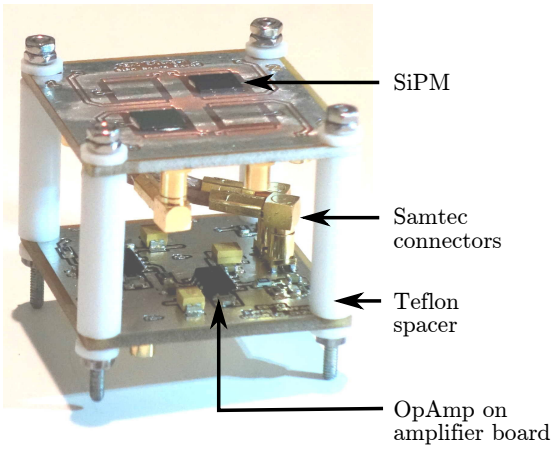

Figure 3.5: SiPM with corresponding mounting board arranged in the holder along with the amplifier board. The connection in between is formed by shielded Samtec connectors. Both boards are hold together via 4 screws. The PTFE spacers serve as electrical insulation.

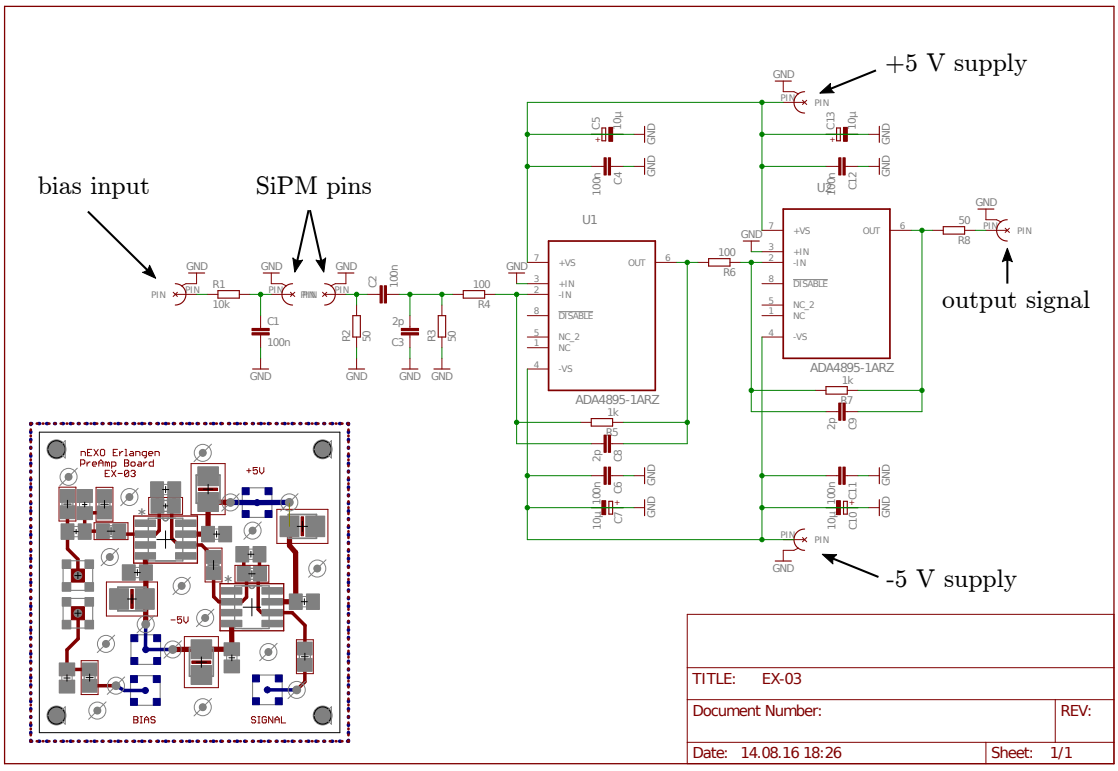

Figure 3.6: Electric circuit diagram of the amplifier used in this work. It consists of two OpAmps connected consecutively. They are inverting amplifiers with an amplification factor of at least -10 each. This results in an amplification of about 100 at the end. Some high-, low- and bandpass filters are integrated to reduce electronic noise.

3.2 Data Acquisition and Waveform Analysis

Based on the setup described in the preceding sections, the measurement procedure and data aquisition was performed in the following way. After the assembly of the cryogenic setup, the first step is to evacuate both the outer chamber and the xenon cell. In case of the outer chamber, this is done via the rotary vacuum pump reaching a pressure of about 3×10^{-4} bar. The vacuum serves insulation purposes and is maintained during the entire measurement. For the xenon cell, this is different, as the actual measurement is performed in a gaseous environment. The evacuation is done in order to reduce contaminations of the xenon cell as well as moisture inside of it. It is performed in two steps. At first, the backing pump is started to eliminate coarse contaminations which would overextend the turbomolecular pump. When a vacuum of about 10^{-3} bar is reached, the turbomolecular pump can be switched on to reach a pressure of about 2×10^{-8} bar. It is kept running for one day before the cooling procedure is started. The cooling is done via filling LN in the dewar. After that, the turbomolecular pump is switched off and the xenon cell is filled with GN up to a pressure of approximately 1 bar. Its purpose is to ensure a heat flow and cooling of both the SiPM and the amplifier board. Furthermore, the use of pure GN avoids ice formation inside the chamber. The cooling process lasts several hours. Further time is needed until a constant temperature of about $-100\,°\mathrm{C}$ is reached at the SiPM.

As soon as this is the case, the measurement can be started. The amplifier as well as the SiPM are switched on. The SiPM needs a bias voltage in the order of about $-30\,\mathrm{V}$. As the operation of the OpAmp is always accompanied by heat losses, this has to be taken into account while adjusting a stable temperature. The amplified signal of the SiPM is fed into the oscilloscope. A trigger on the amlitude of the SiPM is used. As the output generates negative signals, the trigger is set onto the negative edge. Ideally, the trigger should be set to half the height of the 1 p.e. and above all electronic noise. This is adjusted manually. Only signals larger than 0.5 p.e. are displayed. As the measurement is performed in the absence of light, all signals refer to noise contributions of the SiPM. The data acquisition window is set to $10\,\mu\mathrm{s}$ with a time delay of $-4\,\mu\mathrm{s}$. This delay is used to obtain enough statistics for the later baseline subtraction before the pulse. A sampling rate of $2.5\,\mathrm{GS/s}$ and a bandwidth of 200 MHz are used to filter high frequency noise. A voltage range of of $5\,\mathrm{div/mV}$ is used. Every measurement was performed at $-100\,°\mathrm{C}$. For these settings, the data is saved as textfiles containing voltage versus time values. This is done for several bias voltages of the SiPM. The bias was varied in steps of $0.5\,\mathrm{V}$ from $-32\,\mathrm{V}$ to $-36.5\,\mathrm{V}$. It has to be noted that for every bias, the trigger has to be adjusted. This is because the amplitude increases and the voltage value of 0.5 p.e.

The voltage and time values of $10\,\mu\mathrm{s}$ length and trigger at $0\,\mu\mathrm{s}$ are saved for every trigger. This is called waveform. One textfile contains 80 waveforms. The data processing of the measured waveforms happens via a C++-programme of the work group developed by T. Ziegler within the scope of his master's thesis [105]. For convenience, the voltage values are inverted so that the resulting pulses are positive. Ffirst analysis steps can be made with this procedure. This includes the maximum pulse height and the integral of the data. For both analyses, the baseline is subtracted first. For the maximum pulse height, the mean voltage up to $-20\,\mathrm{ns}$ is subtracted from the maximum voltage. The integral baseline is obtained by the summation of all values before $-20\,\mathrm{ns}$ and scaling with the sampling rate. This is then subtracted from the integral. The distribution of the maximum pulse heights or the integrals results in a pulse height spectrum or charge spectrum, respectively (see sec. 3.3.1).

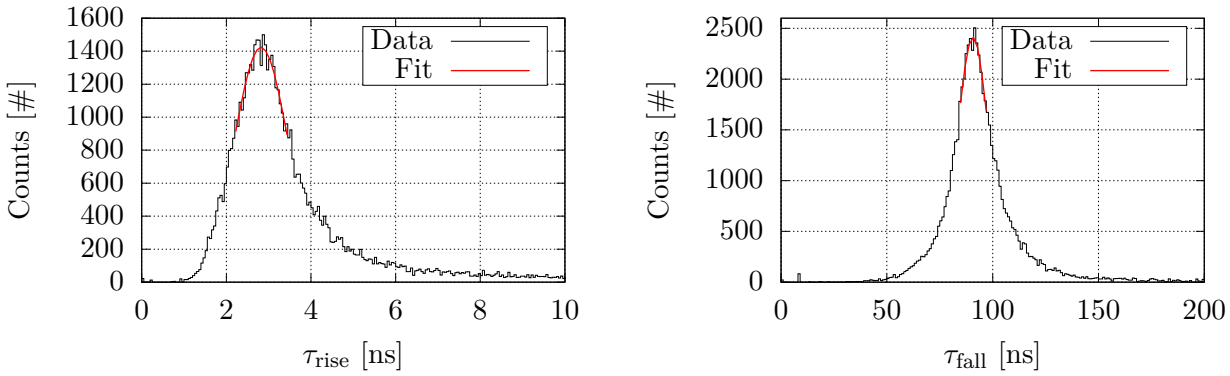

(a) Rise time. **(b)** Fall time.

Figure 3.7: Histograms of the rise and fall time after the first fit with a fixed baseline. Rise- and fall time can vary in a given interval. A Gaussian fit within an $1\,\sigma$ interval around the mean value is applied. The mean value of this fit determines $\overline{\sigma}$ and $\overline{\tau}$ for the second fit.

For a detailed analysis, more knowledge about one pulse is required and the pulses are fitted. As one waveform can include multiple pulses, it is not sufficient to determine the maximum value of the waveform. A peakfinder searches for real peaks separating them from noise peaks. A more detailed description can be found in [105]. The resulting peaks are then used as start parameters for the fit. The entire fit formula was adapted from [109] to:

$$f\left(t, B, N, \sigma, \tau, \sum_{i}^{N}(\mu_i, A_i)\right) = B + \sum_{i}^{N} \frac{A_i}{2} \cdot \exp\left(\frac{1}{2}\left(\frac{\sigma}{\tau}\right)^2 - \frac{t-\mu_i}{\tau}\right) \cdot \operatorname{erfc}\left(\frac{1}{\sqrt{2}}\left(\frac{\sigma}{\tau} - \frac{t-\mu_i}{\sigma}\right)\right), \tag{3.1}$$

where B denotes the constant baseline before the pulse, N the number of fitted pulses, μ_i the time of the ith pulse with amplitude A_i, σ the rise time and τ the fall time. The fit routine is performed in two steps. In the first run, B is fixed to a value obtained from a constant fit to the baseline and the values from the peakfinder are used as start parameters for μ_i and A_i. σ and τ are optimised in a given interval with the initial values of 2.0 ns and 80.0 ns, respectively. The final values of σ and τ are stored into a histogram. Two exemplary distributions of rise and fall time are plotted for $U_{\text{bias}} = -35\,\text{V}$ in fig. 3.7. Both distributions have a modus $\overline{\sigma}$ and $\overline{\tau}$. It is determined by a Gaussian fit within an $1\,\sigma$ interval around the mean value. This is done for every U_{bias}. For the second fit run, the rise and fall time are fixed to the values $\overline{\sigma}$ and $\overline{\tau}$, whereas B, A_i and μ_i are fitted. Every pulse has the same pulse shape with only a varying pulse amplitude, position and baseline. This procedure in two steps guarantees a stable fit behaviour as well as accuracy of the second cycle.

Furthermore, overlapping pulses can be identified. This is particularly important for the analyis in sec. 3.3.4.2. Very closely adjacent pulses are not found by the peakfinder and thus not fitted. This problem is solved by a so-called refitting procedure using χ^2_{red}. For the case of $\chi^2_{\text{red}} > 0.6$, another pulse is added to the fit. If the new χ^2_{red} is improved more than 2 % compared to the initial fit, the additional pulse is kept. This procedure can also be applied for more than one additional pulse in succession. The exact procedure of the refitting algorithm is discussed in [105].

Finally, many different parameters describing a waveform are saved. This includes the time of the trigger, the baseline value, the maximum value and the time of the maximum of one waveform. The fitted pulses are stored in chronological order and A_i, μ_i and $f(\mu_i)$ are saved for every pulse. This enables a detailed analyis.

3.3 Measurement and Analysis

In this section, the measurements of several characteristics of a SiPM of the type FBK VUV-HD LF from FBK are presented. It originates from the wafer position (7,6) and its results are compared to similar devices from the positions (3,6), (18,3) and (1,13). The analyis methods for the single characteristics are described. This includes the pulse height spectrum with which the gain of the SiPM is determined. Several techniques are discussed and the breakdown voltage is obtained. The different noise contributions such as darkcount rate, afterpulsing and optical crosstalk are investigated together with a final overview of the single components. Some further analyses include the recovery time as well as rise and fall time studies. A short summary is given along with a discussion of the results in the end.

3.3.1 Pulse Height Spectrum

The first step in the analysis is to determine the pulse height spectrum. Another possibility is to use the integral resulting in the charge spectrum. Gain and the breakdown voltage can be determined. Figure 3.8 depicts a pulse height spectrum for $U_{\text{bias}} = -36\,\text{V}$ and $T = -100\,°\text{C}$. The red curves are Gaussian fits to the peaks referring to 1 p.e., 2 p.e., etc. Their p.e. value versus the mean fit value of the Gaussian curves is shown in the upper plot. It shows a linear dependency. The mean pulse

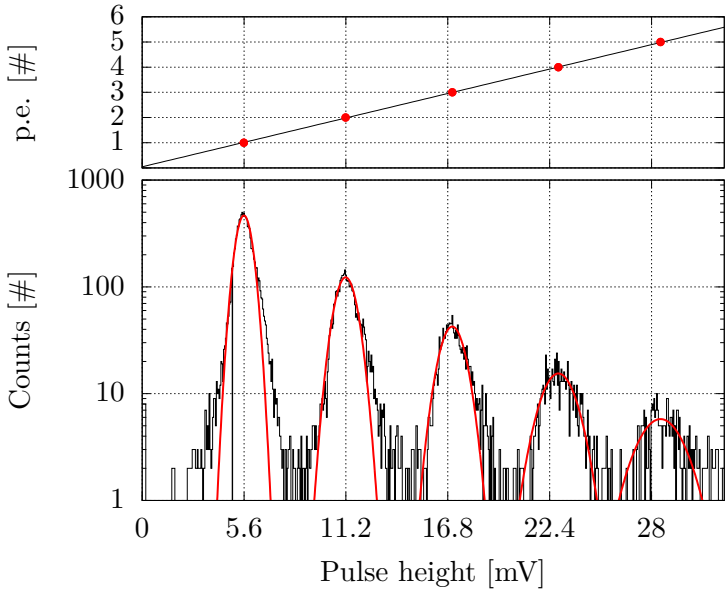

Figure 3.8: Pulse height spectrum (bottom) for a measurement obtained for $U_{\text{bias}} = -36\,\text{V}$. The first peak corresponds to 1 p.e., the second one to 2 p.e. etc. A Gaussian fit is applied to each peak. In the upper plot, the number of p.e. is shown as a function of the mean pulse height. It follows a linear dependency.

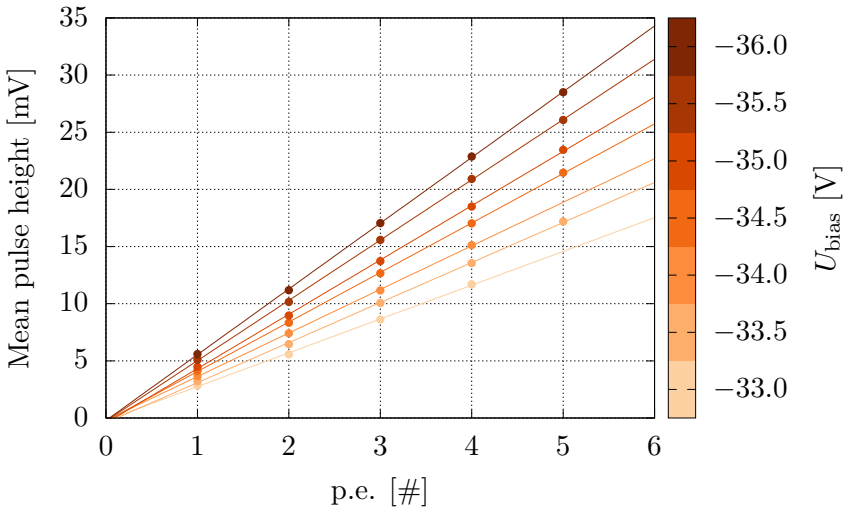

Figure 3.9: Mean pulse height in mV as a function of the number of p.e. for different U_{bias}. It follows a linear dependency. The slope of the curves is larger for a lower U_{bias}.

height depends on U_{bias}. For lower U_{bias}, the pulse height increases. This is illustrated in fig. 3.9. The mean pulse height of a single p.e.-pulse versus the number of p.e. is shown for different U_{bias}.

3.3.2 Gain

The gain can be obtained from the pulse height or the charge spectrum. A correct determination is crucial, since the gain curve yields U_{break}. Errors in U_{break} yield a wrong U_{over}.

Concepts:
The gain is the distance of the peaks in the pulse height or the charge spectrum. It is determined in two different ways. The first possibility was presented in fig. 3.8. A Gaussian function is fitted to each peak in the spectrum. This is done for every U_{bias}. After that, the mean value of the pulse height is plotted versus U_{bias}. This gives a linear curve with the gain being the slope of it.

Another possibility is to use the autocorrelation of the spectrum. It describes in what extent a function or data resembles itself under horizontal translation. The basic working principle is shown in fig. 3.10. The upper plot depicts the original pulse height spectrum in dark blue. It is shifted to the right in steps of 0.2 mV. This is indicated by the spectrum in light blue. The lower plot depicts the autocorrelation of the original spectrum as a function of the shift. The red line represents a fit of five Gaussian functions. Since a non-shifted spectrum resembles itself completeley, the autocorrelation is 1 for a shift of zero. Due to the periodicity of the spectrum, the autocorrelation shows peaks for every shift of 1 p.e. As the gain is the distance of the peaks in the spectrum, a shift of 1 p.e. is equal to the gain. An advantage over the first technique is that it is sufficient to fit only the autocorrelation for a shift of 1 p.e. This is because the correlation of the entire dataset is determined. All orders of p.e. of the original spectrum are already taken into account for a shift of 1 p.e. Only one fit is necessary in contrast to multiple fits in case of the Gaussian fitting technique (see sec.3.3.1).

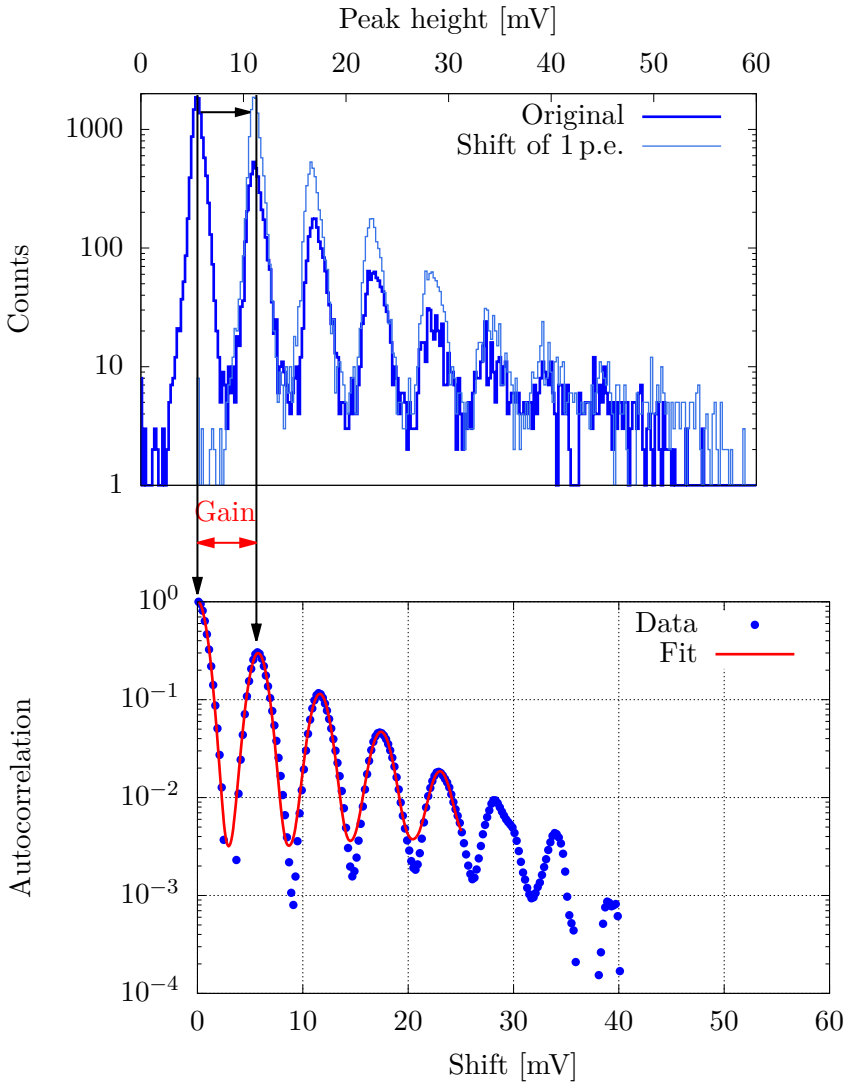

Figure 3.10: Illustration of the autocorrelation method for the gain determination. The upper plot in dark blue shows the pulse height spectrum for $U_{\text{bias}} = -36\,\text{V}$ and a shift of 1 p.e. The plot below depicts the autocorrelation in dependence on the shift in mV. A fit of multiple Gaussian functions (red curve) is performed to determine the gain.

Both techniques yield comparable results. This is illustrated in fig. 3.11. It shows the gain versus U_{bias} obtained by the Gaussian fits and the autocorrelation. For both methods, the same spectra were used.

Pulse Height vs. Charge Spectrum:
The use of the pulse height and the charge spectrum is not equal for the gain determination. The gain is a synonym for the number of secondary electrons. It should be proportional to the charge which is proportional to the integral of the pulses. In contrast, the maximum value of the pulse describes the maximum current. This is the charge per time and not necessarily proportional to the total number of secondary electrons. This should result in a deviation from the gain determined by the pulse height spectrum and by the charge spectrum. In fig. 3.12, the comparison is shown. The red curves belong to the gain from the pulse height spectrum whereas the blue ones originate

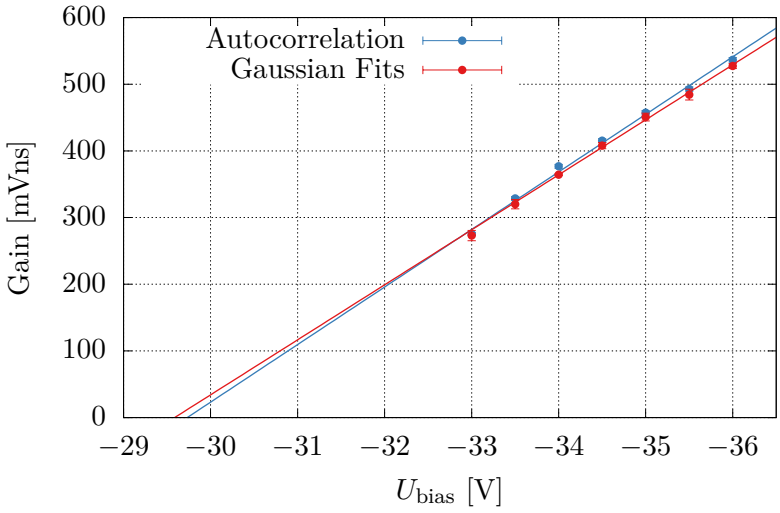

Figure 3.11: Gain versus the absolute value of U_{bias} for the autocorrelation as well as for the Gaussian fit method. Both methods were applied on the same spectra.

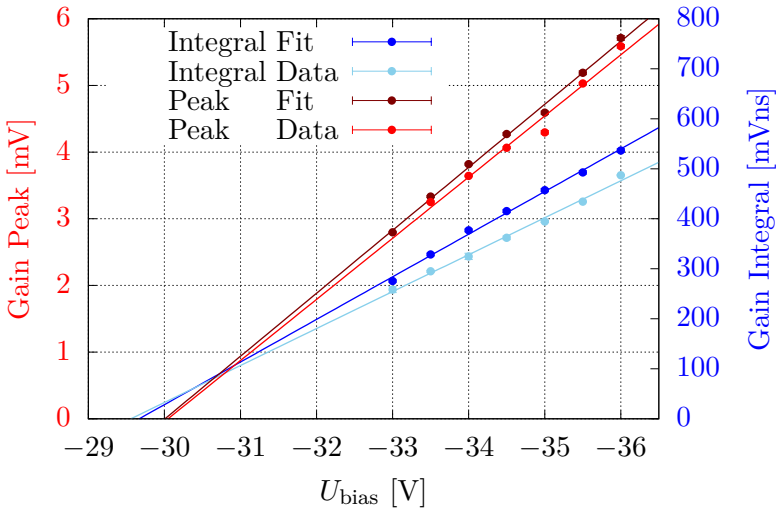

Figure 3.12: Comparison of the gain curves for data obtained from the measurement and for data from the fit for both the pulse height and the charge spectrum. The left y-axis corresponds to the gain curves resulting from the pulse height spectrum (gain peak) and the right y-axis describes the gain curves originating from the charge spectrum (gain integral).

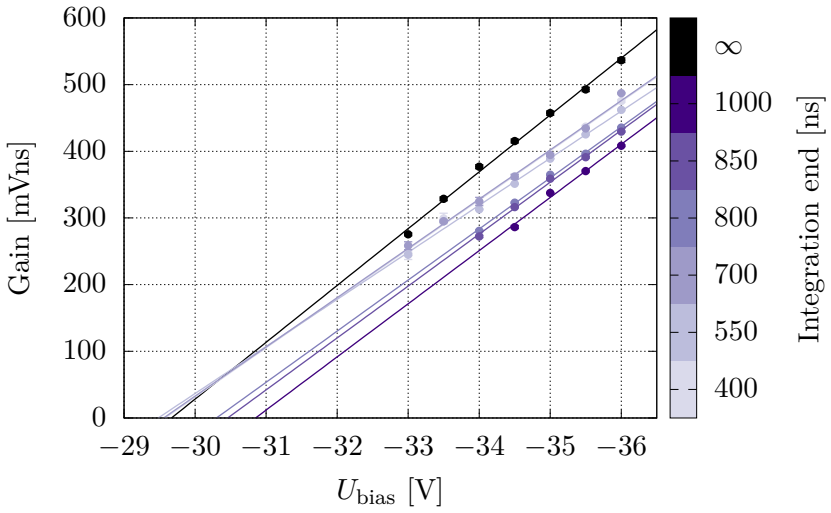

Figure 3.13: Comparison of several gain integral curves for different integration limits of the data. In black, the integral originating from the pulse fit is shown.

from the charge spectrum. For both techniques, the gain obtained from the data and from the fit is depicted. All curves are plotted versus U_{bias}. The left y-axis corresponds to the gain curves for the pulse maximum (gain peak) and the right y-axis to the ones for the integral (gain integral). Two aspects are visible. On the one hand, the zero point of the gain peak and the gain integral curves deviate from each other. Regardless of the slope, which is the gain and cannot be compared by number as they have different units, the zero point of the curves – which is U_{break}– should be the same. For gain peak, U_{break} is $-29.6\,\text{V}$, while for gain integral, it is $-30.0\,\text{V}$. This describes the inequality of the two methods. The second aspect is that the values from fit and data are comparable. They yield the same U_{break}.

Integration Gates:
Although the integration window of the data was chosen so that all pulses are enclosed, the curve of fig. 3.12 suggests that some charge "may be missing". This would explain the larger values in case of the fit, where the entire curve was integrated. Several integration windows were checked. The starting point is fixed at $-20\,\text{ns}$, but the end point of the integration window was altered. In fig. 3.13, the resulting curves are plotted. The black curve represents the total integral of the fit curve. All other curves refer to integrated data with different integration windows. The three datasets with 400 ns, 550 ns and 700 ns overlap almost completeley. A change of the integration window in this region does not affect the result and yields the same zero point as the black curve. However, the datapoints lie below the ones of the fit curve. This deviation increases for a larger integration window. The three curves for 800 ns, 850 ns and 1 000 ns integration yield a larger U_{break}. This behaviour indicates an underhoot after the pulse between 700 ns and 1 000 ns which reduces the integral value. An integration of the data from 700 ns to 1 000 ns yields the difference between the integration up to 1 000 ns and 700 ns. An integration window up to 700 ns is used in the following.

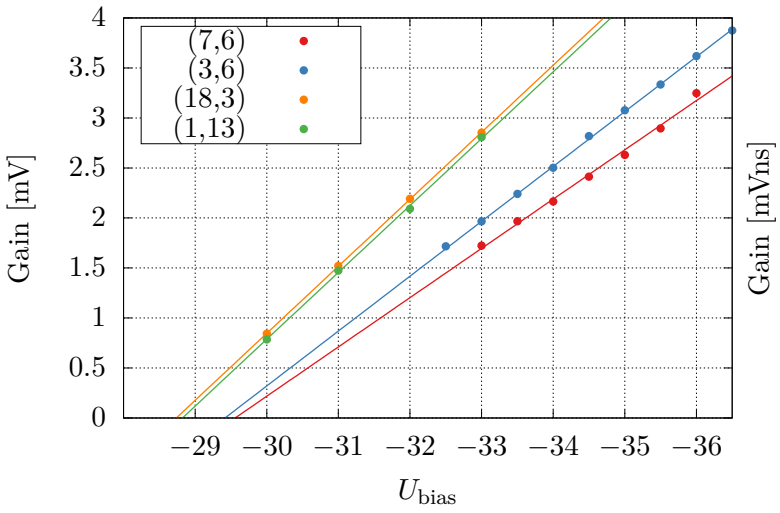

Figure 3.14: Several gain curves for different SiPMs originating from the same wafer. The legend shows the (x,y) position of the SiPM on the wafer. The left y-axis refers to the yellow and green curves while the right one describes the red and blue datapoints.

3.3.3 Breakdown Voltage

The breakdown voltage is determined to be $(29.6 \pm 0.2)\,\text{V}$ for the device at the wafer position (7,6). Collaborators of the nEXO experiment have characterised different devices from the same wafer yielding similar results. This is shown in fig. 3.14. The device at (3,6) was investigated in the same setup as the SiPM at (7,6) [105]. In contrast to that, the two devices (18,3) and (1,13) were characterised in a setup at the Stanford University [106]. All curves yield a similar U_{break}. For the SiPM at (3,6), a breakdown voltage of 29.42 V is obtained. This is similar to the one at (7,6). The SiPM at (18,3) and at (1,13), yield $(28.74 \pm 0.01)\,\text{V}$ and $(28.82 \pm 0.06)\,\text{V}$, respectively.

3.3.4 Contributions to Noise

The determination of the contributions to noise is important for the characterisation of a SiPM. As already explained in sec. 1.3.4, the dominant contributions are the darkcount rate, afterpulsing and optical crosstalk. In this section, the measurements of the noise contributions are shown for the used SiPM. The results are compared to the device at (3,6). An overview of all noise contributions is given at the end.

3.3.4.1 Darkcount Rate

In order to measure the DCR, it is important to known how many pulses per time occured in the absence of light. Besides, the dead time of the measuring device – in this case, the oscilloscope – has to be taken into account. The Poissonian nature of the DCR can be used and the probability to detect n darkcount events within the time interval Δt can be determined via the formula:

$$P(n;\mu) = \frac{\mu^n \cdot \mathrm{e}^{-\mu}}{n!} \qquad \text{with} \qquad \mu = R_{\text{D}} \cdot \Delta t\,, \tag{3.2}$$

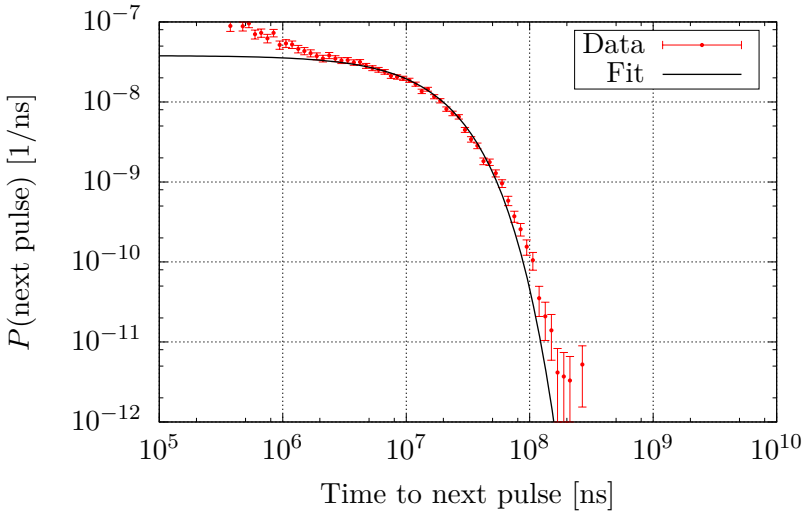

Figure 3.15: Probability of a subsequent pulse to occur at a time difference Δt. In red, the datapoints are plotted with their corresponding errors. The black line refers to a fit of eq. 3.3 in order to determine the DCR.

where μ denotes the average number of DCR events within Δt. For this reason, μ can be written as the product of the mean thermal noise rate R_D and Δt. A careful pulse selection is crucial to determine R_D. The trigger pulse of every waveform is taken. These pulses are also called prompt pulses. For the DCR analyis, they are demanded to be the first pulse within the waveform. This ensures that the prompt pulse is not suffering from afterpulsing. For the pulses satisfying this criterium, the absolute time is calculated compared to the first trigger of the textfile. The chronologically next pulse is taken. It can be of any amplitude and can also be located in another waveform. Its time difference to the prompt pulse is determined. Figure 3.15 illustrates the probability of a next pulse as a function of the time to the next pulse in ns. The red dots are the measured data with its corresponding errors shown for $U_\mathrm{over} = 4.9\,\mathrm{V}$.

According to [26, 51], the probability density ρ_D of a darkcount event can be calculated as:

$$\rho_\mathrm{D}(\Delta t) = P_{\overline{\mathrm{A}}} \cdot R_\mathrm{D} \cdot \mathrm{e}^{-R_\mathrm{D} \cdot \Delta t}\,, \tag{3.3}$$

where $P_{\overline{\mathrm{A}}}$ denotes the probability of no afterpulse within Δt. Equation 3.3 is fitted to the data in fig. 3.15. This is indicated by the black line. For the DCR fit, the data is only fitted up to $\Delta t > 10^4\,\mathrm{ns}$. This is because AP is dominant for shorter time differences.

For a better comparison, the DCR is converted to a rate per mm^2 which is shown in fig. 3.16. It depicts the DCR in dependence on U_over. The red datapoints correspond to the SiPM measured in this work whereas the blue points refer to the SiPM at (3,6). Both DCR distributions follow a linear curve. The DCR does not exceed a value of $3.5\,\mathrm{Hz/mm}^2$. The DCR values below $U_\mathrm{over} = 3\,\mathrm{V}$ deviate from the linear curve and have too low values. This is presumably because the peakfinder does not find all pulses for such low overvoltages. The slope of the DCR of position (7,6) is more than twice the one of (3,6). This cannot be explained by the temperature difference of the two measurements. It was $-104\,^\circ\mathrm{C}$ for the SiPM at (3,6) and $-100\,^\circ\mathrm{C}$ for the SiPM at (7,6). Another indicator may be the time difference of the two measurements. The SiPM at (3,6) was characterised some months before the SiPM at (7,6). Long storage times can alter the DCR, especially under

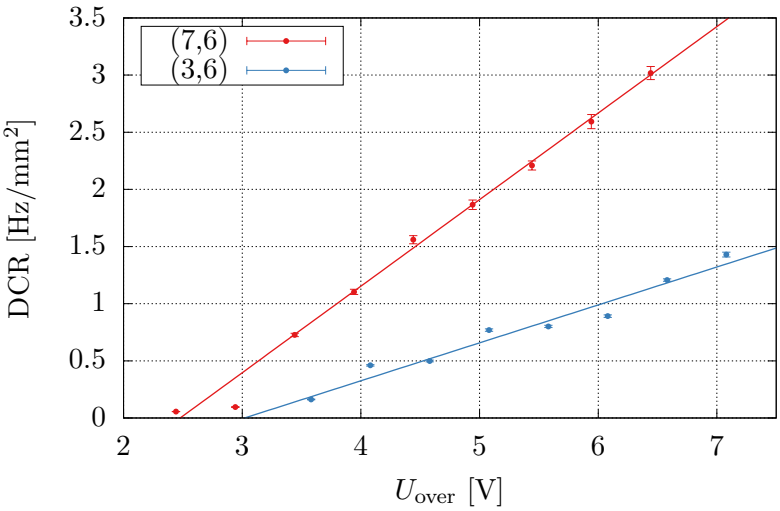

Figure 3.16: DCR versus U_{over}. SiPM (7,6) is plotted in red and SiPM (3,6) in blue. Both curves show a linear dependence on the overvoltage.

radiation and for high storage temperatures. This is because radiation can create impurities in the silicon lattice and high temperatures can create stable, secondary defects [10]. Both effects increase the DCR. Another possibility is that the SiPM at (7,6) may have more impurities from the date of fabrication and thus a higher DCR.

3.3.4.2 Afterpulsing

The analyis of afterpulsing is similar to the one of the DCR. At first, the time to the next pulse is needed. This was already determined in the previous section. The distribution for $\Delta t < 10^4$ ns is mainly relevant for afterpulses. As described in sec. 1.3.4.2, afterpulses originate from released charge carriers trapped earlier in impurity defects. This is described by the trapping lifetime τ_{A}. The probability density for an afterpulsing event ρ_{AP} is depends on the inverse trapping lifetime $R_{\text{A}} = \tau_{\text{A}}^{-1}$:

$$\rho_{\text{AP}}(\Delta t) \propto R_{\text{A}} \cdot \mathrm{e}^{-R_{\text{A}} \cdot \Delta t} \,. \tag{3.4}$$

In contrast to the DCR, afterpulses have a higher probability to occur during the pixel recharging. The recovery of the pixel is crucial for ρ_{AP}. With the incorporation of the recovery process, the probability density for an afterpulsing event is given by [26]:

$$\rho_{\text{AP}} = \left(1 - \mathrm{e}^{-t/\tau_{\text{R}}}\right) \cdot R_{\text{A}} \cdot \mathrm{e}^{-R_{\text{A}} \cdot t} \,, \tag{3.5}$$

whereby τ_{R} denotes the recovery time of the pixel. Its calculation is explained in more detail in sec. 3.3.5.1.

Equation 3.5 only holds true in case of one trapping lifetime. There can be more than one defect in the silicon lattice with individual lifetime contants τ_i. This means that it has to be summed over all n_A defects in order to obtain the total afterpulsing probability density $\rho_\mathrm{AP}^\mathrm{tot}$:

$$\rho_\mathrm{AP}^\mathrm{tot}(\Delta t) = \sum_{i=0}^{i<n_\mathrm{A}} \left[\rho_{\mathrm{A}_i}(\Delta t) \cdot \prod_{\substack{j=0 \\ j<n_\mathrm{A}}}^{j\neq i} P_{\overline{\mathrm{A}_j}}(\Delta t) \right] . \tag{3.6}$$

It has to be ensured that no other time constant j contributes if the ith time constant produces an afterpulse with the probability density $\rho_{\mathrm{A}_i}(t)$. They have to be multiplied with the probabilities $P_{\overline{\mathrm{A}_j}}(t)$ of no afterpulsing event occuring for every other time constants. The summation over all time constants yields $\rho_\mathrm{AP}^\mathrm{tot}$.

Only the part for $\Delta t > 10^4$ ns was fitted in sec. 3.3.4.1. With the combination of eq. 3.3 and eq. 3.6, the entire distribution can be described. The final formula is [26]:

$$\rho_\mathrm{tot} = \underbrace{\rho_\mathrm{D}(t) \cdot \prod_{i=0}^{i<n_\mathrm{A}} P_{\overline{\mathrm{A}_i}}(\Delta t)}_{\mathrm{DCR}} + \underbrace{P_{\overline{D}}(\Delta t) \cdot \sum_{i=0}^{i<n_\mathrm{A}} \left[\rho_{\mathrm{A}_i}(\Delta t) \cdot \prod_{\substack{j=0 \\ j<n_\mathrm{A}}}^{j\neq i} P_{\overline{\mathrm{A}_j}}(\Delta t) \right]}_{\mathrm{AP}} . \tag{3.7}$$

The first term describes the contribution by the DCR and the second one the contribution by AP. In each case, it has to be ensured that no other component contributes. The AP probability is multiplied with the probability $P_{\overline{D}}(t)$ which ensures that no darkcount event occurs and the probability density for a darkcount event is multiplied with all single probabilities $P_{\overline{\mathrm{A}_i}}(t)$ for no AP. Given that the oscilloscope start deadtime is larger than Δt, the probabilities of no darkcount or afterpulsing event are given by [26]:

$$P_{\overline{\mathrm{D}}}(\Delta t) = \mathrm{e}^{-R_\mathrm{D}\cdot\Delta t} , \tag{3.8}$$

$$P_{\overline{\mathrm{A}_i}}(\Delta t) = \mathrm{e}^{-R_{\mathrm{A}_i}\cdot t_\mathrm{rd}} + \mathrm{e}^{-\lambda^{-1}\cdot t_\mathrm{rd}} - \mathrm{e}^{-R_{\mathrm{A}_i}\cdot\Delta t} - \mathrm{e}^{-\lambda^{-1}\cdot\Delta t} , \quad \text{with} \quad \lambda = (\tau_\mathrm{R} + \tau_{\mathrm{A}_i})/\tau_\mathrm{R}/\tau_{\mathrm{A}_i} , \tag{3.9}$$

where t_rd denotes the recovery dead time and τ_R the pixels' recovery time constant. For the fit of the complete distribution of ρ_tot, the one of the DCR is firstly fitted as described in sec. 3.3.4.1 and after that, R_D is fixed for the fit of AP. The entire fit of DCR and AP is depicted in fig. 3.17 for U_over= 5.9 V. It shows the probability for a next pulse in terms of Δt. The red points represent the data with their corresponding error and the black line is the fit of AP and DCR. Afterpulsing dominates for 10^2 ns $< \Delta t < 10^4$ ns whereas for 10^4 ns $< \Delta t < 10^8$ ns, the events are most probable due to the darkcount rate. Events for $\Delta t < 30$ ns are excluded in the fit. The gap at $\Delta t = 10^4$ ns is due to the dead time of the oscilloscope. It is visible that P_tot decreases for a larger Δt. This means that it is more probable for a pulse to occur shortly after the prompt pulse compared to later times.

The best results for the fit are obtained by introducing five different time constants τ_i. Their corresponding lifetime τ_i versus U_over is plotted in fig. 3.18. A decrease of the τ_i can be noticed for an increasing U_over. This can be explained by the higher electric field correlating with a larger U_over. The electrons captured in the lattice defect are more likely released. This reduces τ. With a constant fit, the mean lifetime is determined. It yields $\tau_1 = (0.074 \pm 0.009)$ µs, $\tau_2 = (0.34 \pm 0.04)$ µs, $\tau_3 = (1.57 \pm 0.09)$ µs, $\tau_4 = (60 \pm 18)$ µs and $\tau_5 = (620 \pm 77)$ µs. In contrast to that, only three

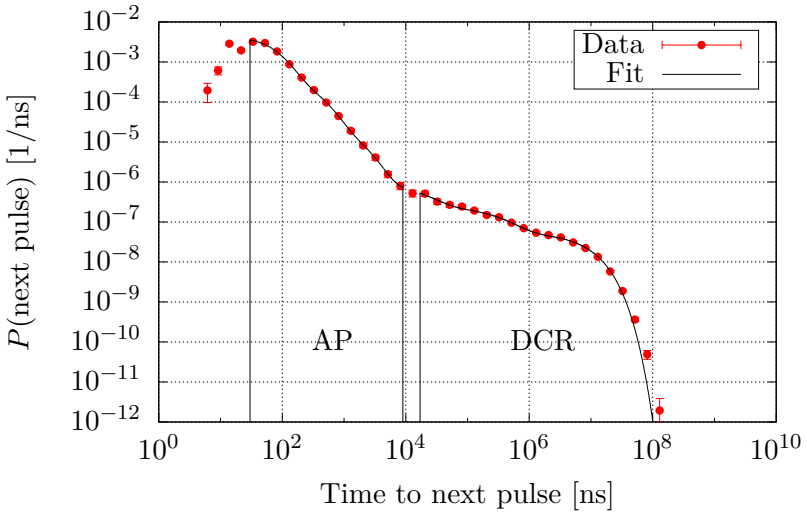

Figure 3.17: Full distribution of the probability for a next pulse depending on the time to the next pulse. In red, the measured data is plotted with a fit of AP and DCR in black. At $\Delta t = 10^4$ ns, there is the dead time of the oscilloscope.

time constants were found for the SiPM of position (3,6). Their lifetime are similar to the SiPM at position (7,6), but the two very large time constants in the range of several µs are missing. A higher number of lattice defects increases the DCR. This may explain the so much larger DCR observed in sec. 3.3.4.1.

The individual afterpulsing probability is determined for each time constant. In fig. 3.19, it is plotted depending on U_{over} for every τ_i. On average, the afterpulsing probability increases for a larger U_{over}. This is reasonable as an increasing U_{over} increases the DCR. An avalanche occurs more often during which electrons can be trapped. Moreover, the lifetime is reduced. This means that the defect is able to trap another electron after a shorter time than for a lower U_{over}. Both effects increase the afterpulsing probability. It does never exceed 0.3. The highest afterpulsing probability between 0.1 and 0.3 is obtained for the shortest lifetime of $\tau_1 \approx 74$ ns. This is also depicted in fig. 3.20. It shows the probability as a function of the lifetime for every U_{over} value. It is visible that the probability firstly decreases for longer lifetimes. Though, τ_3 represents an exception. It has the largest τ, but its afterpulsing probability is approximately as large as the one of τ_2.

The summation of all individual afterpulsing probabilities yields the total AP probability P_{AP}. For the nEXO experiment, only the correlated noise within 1 µs is relevant. In fig. 3.21, only P_{AP} within 1 µs is shown. It is plotted versus U_{over}. The red points correspond to the SiPM at (7,6) measured in this work and the blue points to the SiPM at (3,6). Both detectors show similar results. $P_{\text{AP}}(\Delta t)$ lies approximately between 0.2 and 0.5 for U_{over} between 3.5 V and 6.5 V. An almost linear increase of P_{AP} for higher U_{over} is visible, too.

3.3.4.3 Optical Crosstalk

A pulse height spectrum from a measurement in the absence of light as in fig. 3.8 shows pulses up to several p.e. With no incident light, the only primary source can be darkcount events. Under the

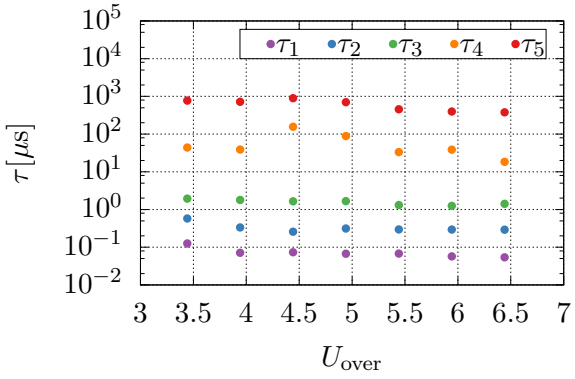

Figure 3.18: Lifetime of the five time constants found in the AP analyis versus U_{over}.

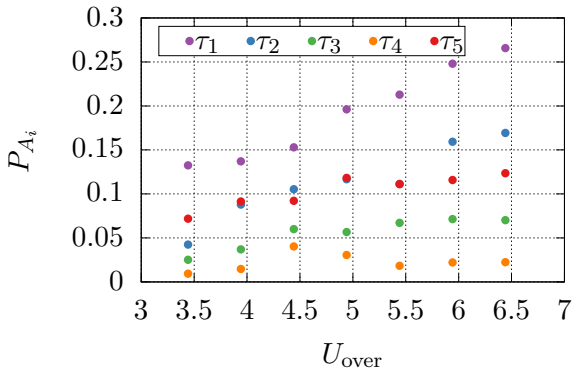

Figure 3.19: Individual afterpulsing probabilities of the single time constants depending on U_{over}.

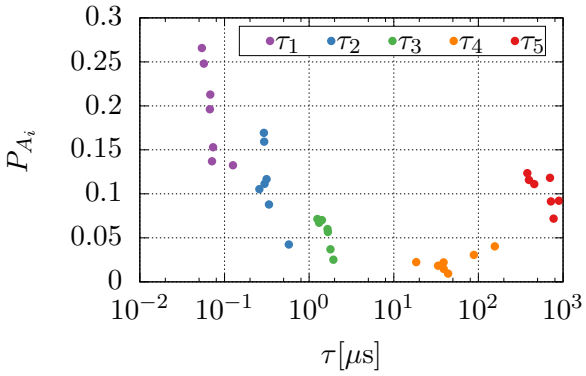

Figure 3.20: Afterpulsing probabilities as a function of the lifetime τ_i for the different time constants.

assumption of a Poisson distribution of the DCR, the probability that multiple darkcount events occur coincidently is only 0.002 6 [110]. It cannot be the sole origin for pulses higher than 1 p.e. The reason for the large number of pulses occuring with more than 1 p.e. is CT. Photons produced during an avalanche can reach an adjacent pixel an trigger another avalanche. This happens almost simultaneously to the orignal pulse. The probability P_{CT} that CT occurs can be calculated from the pulse height spectrum via [110]:

$$P_{CT} = 1 - \frac{N_1}{N_{tot}}, \tag{3.10}$$

where N_1 is the number of events with the pulse height of 1 p.e. and N_{tot} the total number of events in the spectrum. The fraction of N_1 and N_{tot} is the percentage of events with 1 p.e. In a pulse height spectrum with no pedestal, all other events must originate from CT. This gives the probability P_{CT}. This is only true when AP can be excluded from the pulse height spectrum. In order to achieve this, a spectrum is created demanding that the pulses must be trigger pulses and P_{CT} can be determined according to eq. 3.10. The lower plot of fig. 3.22 illustrates P_{CT} in dependence on U_{over} for the devices at (7,6) in red and at (3,6) in blue. Both datasets lie almost

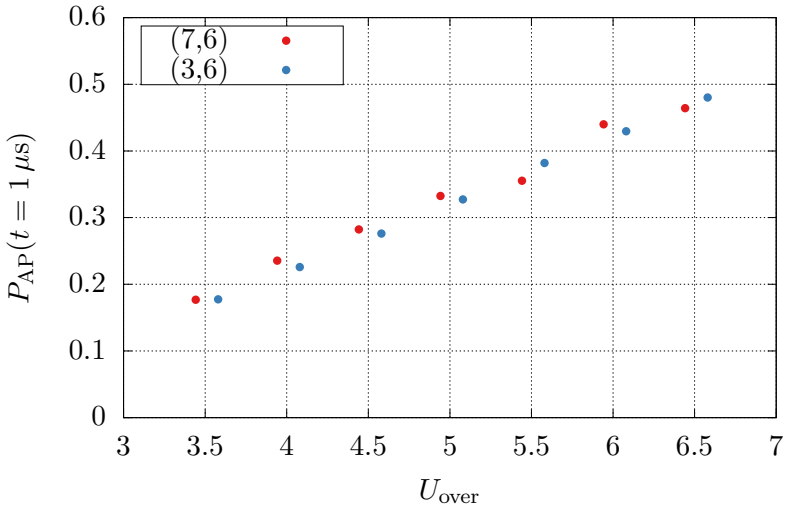

Figure 3.21: Probability for afterpulses to occur within a time window of $t = 1\,\mu\mathrm{s}$ versus U_{over}. It lies between 20 % for U_{over}=3.5 V and 50 % for U_{over}=6.5 V for both devices.

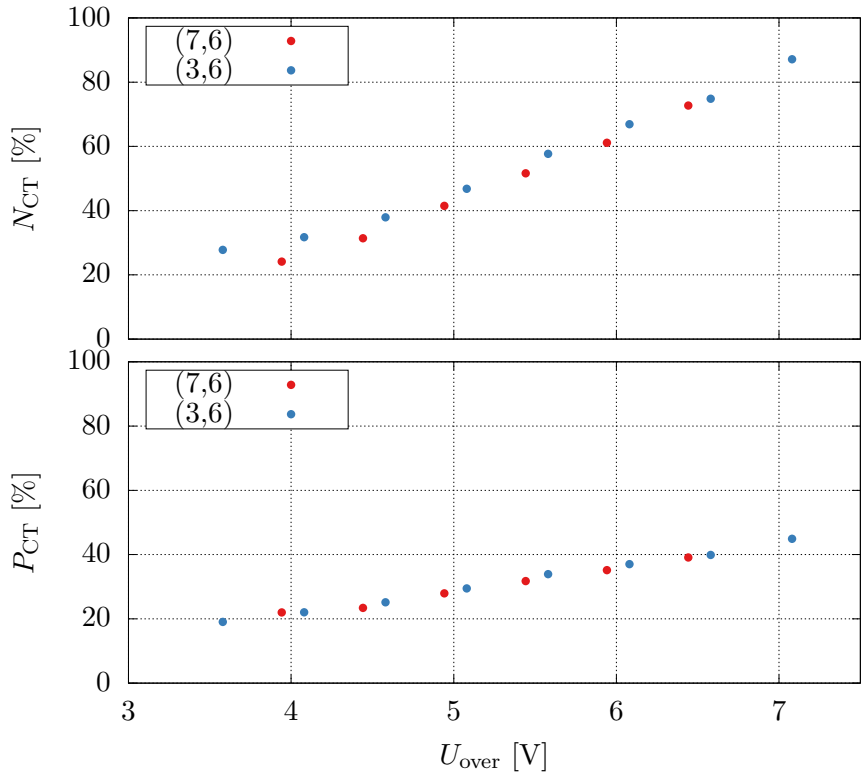

Figure 3.22: N_{CT} and P_{CT} depending on U_{over} for the SiPMs (7,6) in red and (3,6) in blue. For both cases, the devices show a similar behaviour.

completeley on one curve and show a linear increase with U_{over}. P_{CT} is between 20 % and about 40 %.

However, P_{CT} does not take into account if there was one additional CT event or multiple ones. It gives only the probability, that CT occurs regardless of the multiplicity. In order to account for this, the number N_{CT} of CT events can be determined. The mean of the pulse height spectrum is calculated. It is important that the spectrum only contains CT events, otherwise other contributions such as AP are included. This results into the upper plot of fig. 3.22. N_{CT} is plotted versus U_{over} for both devices. It increases with an increasing U_{over}. Especially for high U_{over}, N_{CT} of both devices is similar.

3.3.4.4 Overview

Each noise component was investigated separately so far. An overview of all components is shown in fig. 3.23 depicting the pulse height versus the relative time to the trigger. It includes all events between 1 ns and 10 µs after the initial trigger. The coloured circles mark the different components which can occur. All pulses between 1 ns and 10 ns are prompt pulses. This means that they initiated the trigger. The pulse distribution at 1 p.e. marked red refers to darkcount events or late afterpulses. CT occurs simultaneously with a larger amplitude. Two or more pixel are triggered at the same time resulting in 2 p.e. or higher ones. Afterpulsing occurs shortly after the prompt pulse. It can be recognised from the smaller pulse height than 1 p.e. The pixel is not fully recovered yet and the amplitude is lower than for a 1 p.e. pulse. Its contribution in the pulse height spectrum is visible at the right side. Afterpulses fill the valleys between the integer peaks. With a cut to prompt pulses, their contribution is omitted. After the recovery time, the pulse height is fully restored. It is no longer distinguishable for a single pulse whether it belongs to DCR or AP. This is only possible statistically. For this reason, the pulses with a green circle can originates from both DCR or AP. The probability of a next pulse decreases for longer times. This is illustrated in the plot below. Along with DCR and AP, also CT can occur. This results in a repetition of the band structure at higher p.e. Early afterpulses can be accompanied by CT creating an amplitude between the integer peaks. The same principle applies to late afterpulses and darkcount events with the difference that those are located at integer peaks with a pulse height larger than 1 p.e.

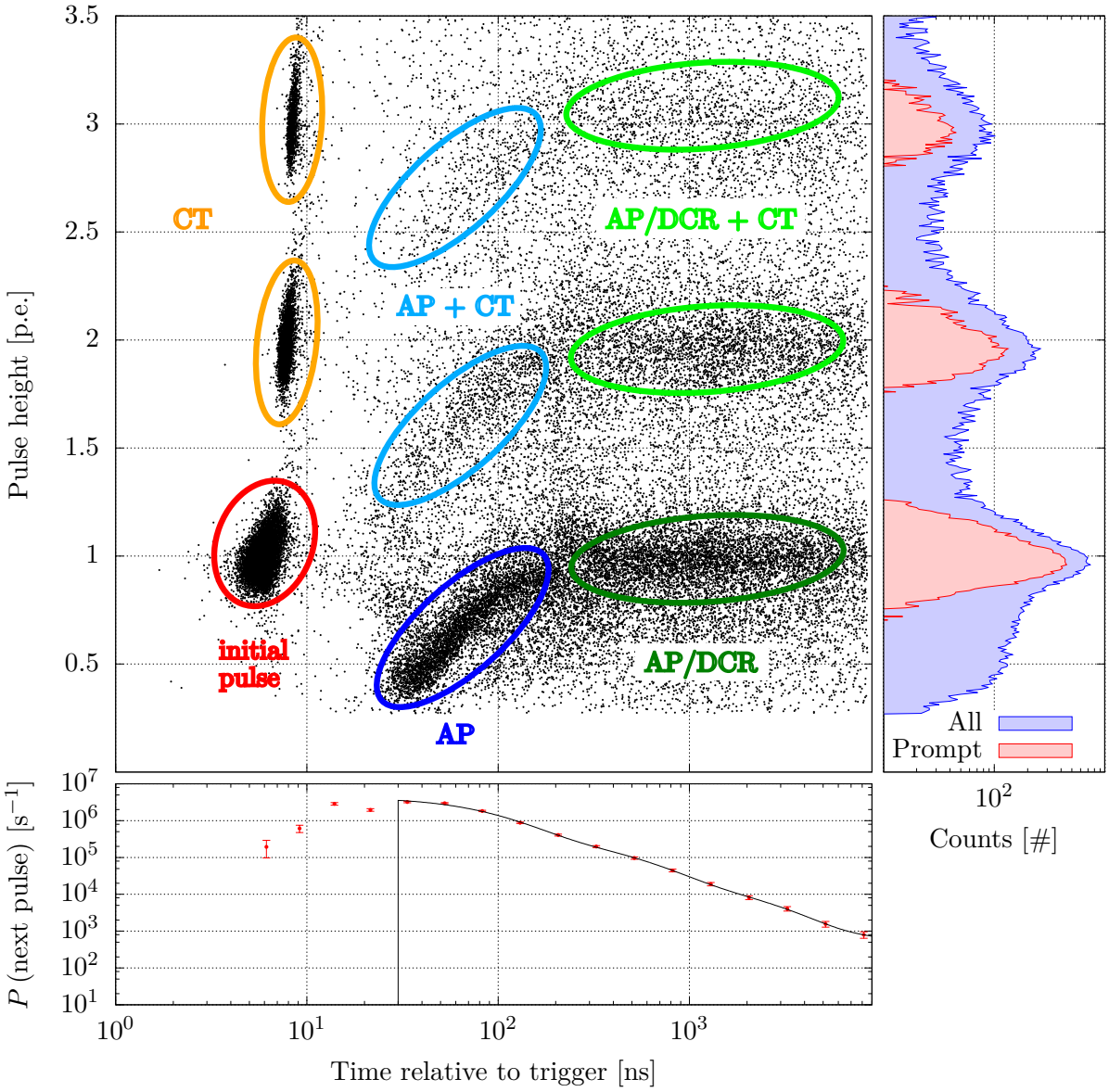

Figure 3.23: Pulse height in p.e. depending on the relative time to the trigger up to 1 µs. The different noise contributions are marked. A projection of the pulse height of all and only the prompt pulses is shown at the right side. The plot below is the projection of the time relative to the next pulse.

3.3.5 Further Analysis

In addition to the most fundamental characteristics such as gain, breakdown voltage and noise contributions, there are further parameters which can be investigated. This includes for instance the recovery time. Its determination is obligatory for the AP calculation. In sec. 3.3.5.1, the determination of the recovery time is explained. Furthermore, rise and fall time studies are presented in sec. 3.3.5.2.

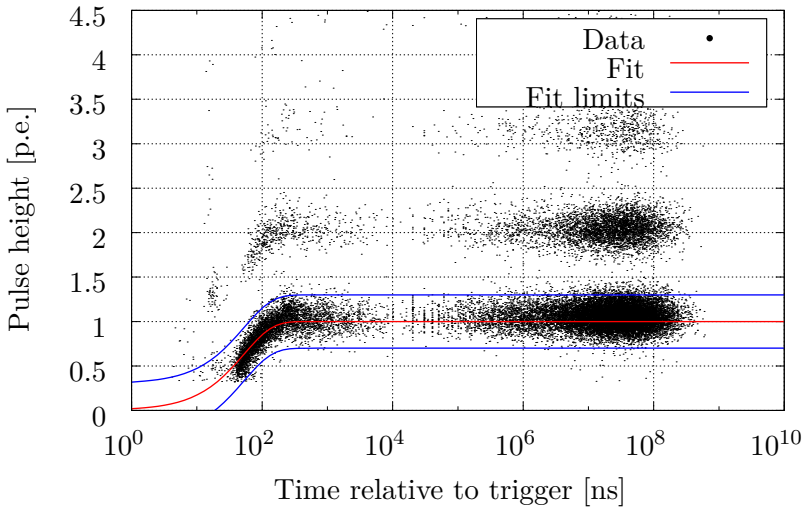

Figure 3.24: Pulse height in p.e. of the not prompt pulses in dependence on the relative time to the trigger. The recovery curve of eq. 3.11 is fitted to the data (red curve). In blue, the fit limits are plotted. They ensure that only pulses with lower or equal to 1 p.e. pulse height are taken into account.

3.3.5.1 Recovery Time

During the recovery time, the sensitivity of the pixel is restricted. This is because the applied U_{over} has not reached its nominal value yet. In addition to the sensitivity, the output pulse height is reduced. The reason is the lower gain due to the lower U_{over}. The recovery time τ_{R} is the time constant during the recovery process.. It depends on the capacitance C_{D} of the pixel and its corresponding quenching resistor R_{Q}. The larger one of both components is, the larger becomes also τ_{R}. Depending on the time t, the recharging process can be described as follows [38]:

$$U_{\text{over}}(t) = U^0_{\text{over}} \cdot \left(1 - \mathrm{e}^{-t/\tau_{\text{R}}}\right) , \tag{3.11}$$

with $U_{\text{over}}(t)$ the current overvoltage over the pixel, U^0_{over} the nominal overvoltage when no recharging occurs and τ_{R} the recovery time constant. Equation 3.11 can be used to determine τ_{R}. The relative time to the trigger pulse is determined and the corresponding pulse height is saved. This results into the plot depicted in fig. 3.24. As prompt pulses are excluded in this picture, only the recharging process is visible. Additional CT causes this structure to be repeated at higher p.e. For the determination of τ_{R}, eq. 3.11 is fitted to this distribution. In order to exclude higher p.e., the data is selected within the shown fit limits in blue. The red line indicates the final fit.

This is done for different overvoltages which generates the plot in fig. 3.25. It illustrates τ_{R} depending on U_{over}. τ_{R} ranges from 44 ns to 56 ns. This is similar to the SiPM at (3,6) which has a τ_{R} between 53 ns and 58 ns. The variation of (7,6) is significantly larger. This may be caused by larger non-uniformities of the pixels or a less stable fit behaviour than for the SiPM at (3,6).

3.3.5.2 Rise and Fall Time

With respect to the fitting procedure described in sec. 3.2, the fit information does not only include the baseline as well as the exact peak position and height, but also the rise time τ_{rise} and fall time

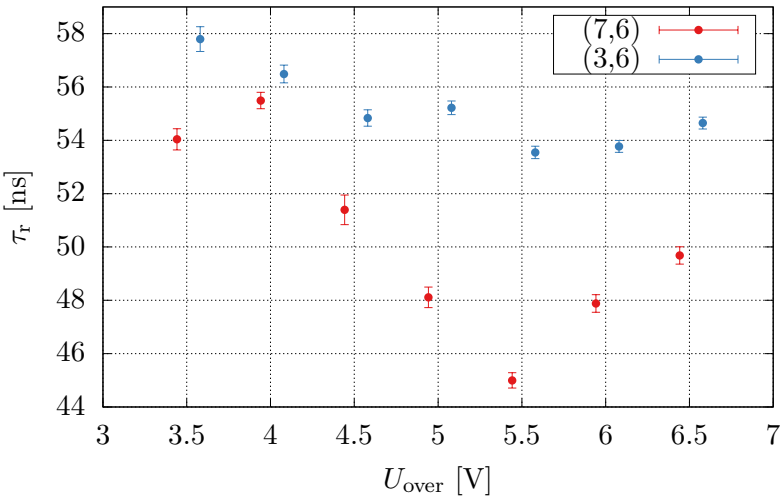

Figure 3.25: Recovery time versus U_{over}. The red points with corresponding errors refer to the SiPM (7,6) while the blue ones describe the SiPM (3,6).

τ_{fall} of the waveform. Within the first fitting routine, the mean τ_{rise} and τ_{fall} have already been determined in sec. 3.2 for each U_{over} . In fig. 3.26, τ_{rise} is plotted versus U_{over}. The red points correspond to the SiPM used in this work at wafer position (7,6) and the blue ones to position (3,6) with their corresponding errors. Both SiPMs have an almost identical τ_{rise} curve ranging from 2.2 ns for 3.5 V to about 2.7 ns for 6.5 V. It increases for larger U_{over}. The exact physical motivation is still unclear as the pulse shape should not change with U_{over}. This may be due to the used readout electronics. The rise time at $U_{over} = 5.5$ V deviates from the other datapoints. This may be caused by an unsufficient fit. Figure 3.27 illustrates τ_{fall} in dependence on U_{over}. In contrast to τ_{rise}, it decreases for higher U_{over} for both SiPMs. While the datapoints of both SiPMs almost lie on the same curve for τ_{rise}, τ_{fall} is significantly larger than the one of (3,6).

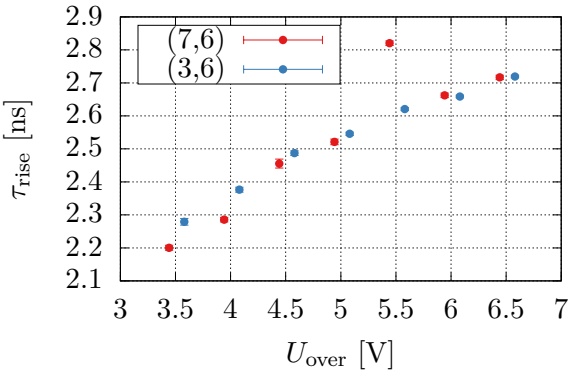

Figure 3.26: Rise time versus U_{over} for the SiPM (7,6) in red and the SiPM (3,6) in blue.

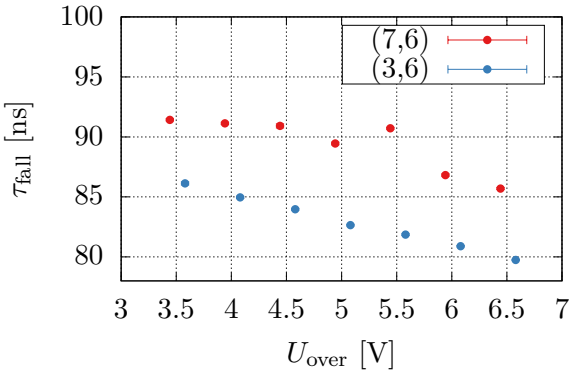

Figure 3.27: Fall time in dependence on U_{over}. The red datapoints describe the SiPM (7,6) and the blue ones the SiPM (3,6).

3.4 Summary and Discussion

A SiPM from FBK was characterised in the absence of light in this chapter. This was done in a setup for cryogenic temperatures at $T = -100\,^{\circ}\mathrm{C}$. Each single pulse was fitted by a C++ programme and the important parameters of the waveform were saved. With the pulse height and charge spectrum, several gain curves were determined and compared. The pulse height was found to not correctly describe the proportionality of the gain to the number of secondary charge carriers and the integral was used for the further analysis. In contrast to that, the use of the data from the measurement and from the fit yield equal results. Two different methods for the gain determination were presented. These are Gaussian fits to the pulse height spectrum and the determination of their slope as well as the use of the autocorrelation of the spectrum. The extrapolation of the gain curve to zero yields the breakdown voltage. It was determined to be $(-29.6 \pm 0.2)\,\mathrm{V}$. This result is comparable to the one of other SiPMs from the same wafer. Different noise contributions were investigated in detail. A model for the DCR and AP was presented. The DCR does never exceed $3\,\mathrm{Hz/mm^2}$ and thus meets the requirements for the nEXO experiment. A linear increase with U_{over} is observed. However, the DCR is more than three times larger than the one of the SiPM at (3,6). This may be explicable by the five instead of three impurities which were found within the AP analyis. Their time constants range from some ns to several µs. SiPM (7,6) has been exposed to α-radiation in vacuum which could have been created radiation damages in the silicon. This may explain the higher number of lattice defects as well as the higher DCR compared to SiPM at (3,6). The AP probability is considerable large with values between 0.2 and 0.5. It shows a linear increase with overvoltage. A similar behaviour could be observed for the SiPM at (3,6). The probability for CT as well as the number of CT events was determined. The results are similar to the device (3,6). P_{CT} lies between 20 % and 40 %. The mean number of CT events increases up to 0.8. This is far larger than the requirement for the nEXO experiment which is 0.2. The recovery time constant as well as rise and fall time constant show similar values commpared to SiPM (3,6). The recovery time constant lies around approximately 50 ns whereas the rise time constant is extremely short with values between 2.2 ns and 2.8 ns. In contrast to that, the fall time constant ranges between 85 ns and 93 ns. One of the main problems during the measurement and analyis procedure was the measurement of $U_{\mathrm{over}} < 3\,\mathrm{V}$. Firstly, the peakfinding algorithm had difficulties to fit such small pulses and failed. This made an evaluation impossible. Secondly, the electronic noise is far too large. Overvoltages below 3 V could not be measured because the signal is so small that it could not be distinguished from noise. Both effects reduced the dynamic range of the SiPM.

Chapter 4

Characterisation of a SiPM with Xenon Scintillation Light

With respect to the characterisation of a SiPM, the measurements with light is one of the most important ones. One of the most fundamental parameters – the PDE – can be determined. In this chapter, the used setup together with the detailed measurement and analysis procedure is described. The PDE results for the SiPM FBK VUV-HD LF from FBK are presented. A discussion of systematic errors is given and further analysis aspects are considered along with a discussion.

4.1 Setup

The same basic setup as described in sec. 3.1 was used. The cooling procedure was the identical. All measurements were performed at a temperature of about −100 °C. The PMT already calibrated in chapt. 2 was used as a reference detector and an α-source was put into the setup. It consists of 48 % ^{241}Am, 40 % ^{239}Pu and 12 % ^{244}Cm. The energy spectrum of the α-source is shown in fig. 4.1. It lies between 5 MeV and 6 MeV. The three constituents have a Gaussian-like distribution with their corresponding maximum referring to their abundance. Most prominent is the peak from ^{241}Am at approximately 5.5 MeV whereas ^{239}Pu has its maximum at ≈ 5.2 MeV and ^{244}Cm at ≈ 5.8 MeV. The chamber is filled with gaseous xenon (GXe) 4.0 [1] at a pressure of about 1 bar. On their way through the GXe, the α-particles produce scintillation light in the UV region at 175 nm. The yellow lines in fig. 4.2 show a simulation of 500 α-tracks from the source through the gas [111]. Nearly all α-particles have the same propation path length of about 2 cm and their emission is equally distributed.

An overview of the arrangement of the relevant parts can be seen in fig. 4.3. At the bottom, the α-source is placed. Both SiPM and PMT are installed at a holder hanging downwards. In fig. 4.4, one can see a photograph of PMT and SiPM including the amplifier boards and the holding structure. The PMT was operated with a supply voltage of 800 V. In contrast to that, the U_{bias} of the SiPM was varied over a range of about 3 V.

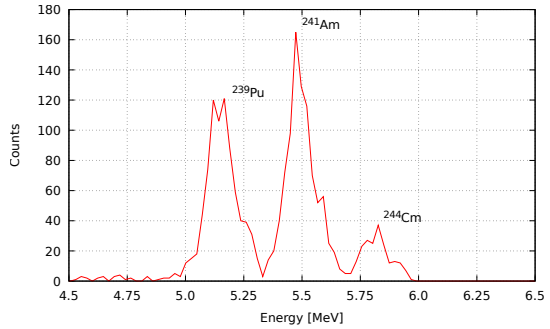

Figure 4.1: Energy spectrum of the used α-source. The measurement was performed by Jürgen Hößl for the nEXO work group.

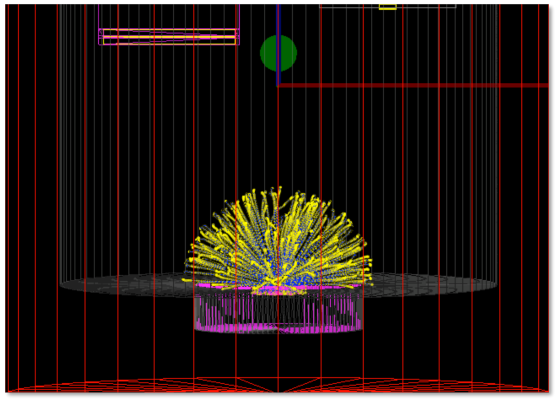

Figure 4.2: Simulation of the α-emission from the radioactive source. The tracks of 500 α-particles are displayed in yellow. Reprinted from [111]

[1] 99.99 % GXe.

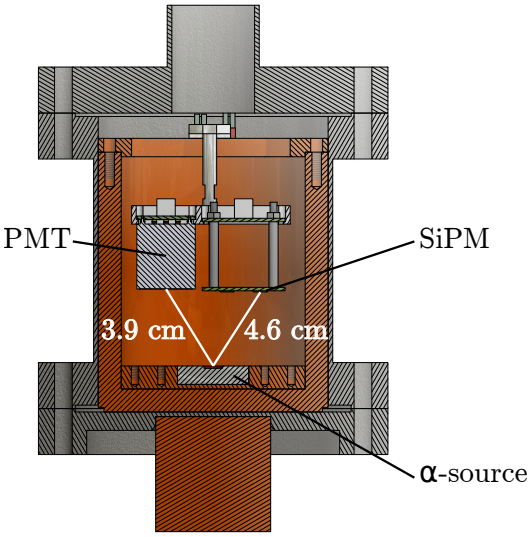

Figure 4.3: Technical drawing of the inner part of the used setup. The detectors are fixed in a holding hanging down and facing the α-source which is installed at the bottom of the chamber.

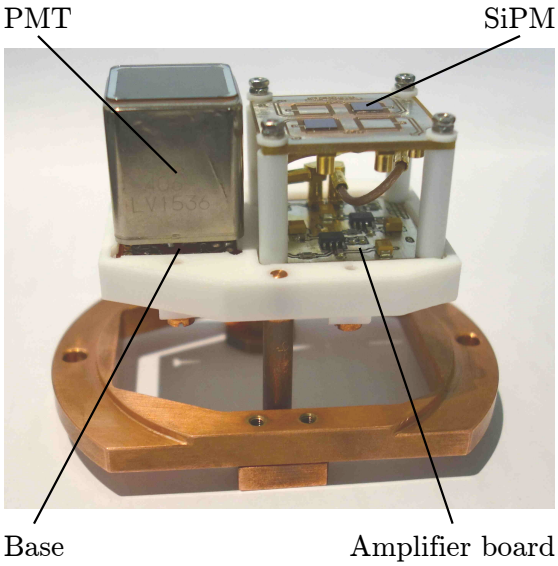

Figure 4.4: Picture of the holding with PMT on the left and SiPM at the right. The corresponding boards are placed below each detector.

4.2 Measurement and Analysis of the PDE

In this section, the basic concept used for the determination of the PDE is described in detail as well as the measurement procedure and the final calculation of the PDE. A propagation of the systematic uncertainties of the PDE is given and further parameters are investigated as well. This includes the correlated noise, the comparison of data and simulation as well as the investigations on the continuity of the light flux onto the detectors.

4.2.1 Basic Concept for the determination of the PDE

In order to calculate the efficiency of a detector – in this case, the PDE – it is essential to know the number N_{ph} of impinged photons. Most of the times, a reference detector is used to measure N_{ph}. In this case, it is a PMT. Reference detector and SiPM should be arranged so that they are exposed to the same flux Φ which is the ratio of number of N_{ph} and area A:

$$\Phi = \frac{N_{\mathrm{ph}}}{A} = \frac{N_\gamma}{\epsilon} \cdot \frac{1}{A} \,. \tag{4.1}$$

Since N_{ph} is the fraction of detected photons N_γ and the efficiency ϵ of the detector, the flux can be rewritten as shown in eq. 4.1.

The setup used in this work is not symmetric and the distances of PMT and SiPM from the source are not the same. The real height of the SiPM is larger than illustrated in fig. 4.3. Moreover, PMT and α-source are in the same plane whereas the SiPM is shifted towards the drawing plane. This gives the real distances of the source as shown in fig. 4.3. A correction factor R has to be multiplied and the assumption of the same flux at both detectors becomes:

$$\Phi_{\mathrm{SiPM}} = R \cdot \Phi_{\mathrm{PMT}} \,, \tag{4.2}$$

with Φ_{SiPM} and Φ_{PMT} the flux at SiPM and PMT, respectively. The correction factor R was obtained in a simulation performed by R. Bayerlein [111]. There were 15 000 α-tracks simulated and for each track, the flux was calculated at the PMT as well as at the SiPM for a xenon pressure of 0.9 bar. A refractive index of $0.095\,206 + \mathrm{i} \cdot 1.964\,0$ was assumed for aluminium which leads to a reflectance of 92.5 %. For copper, $0.944\,18 + \mathrm{i} \cdot 1.353\,5$ was used and a reflectance of 32.7 %. R was obtained by dividing Φ_{SiPM} by Φ_{PMT} for each track and taking the mean R of all 15 000 tracks. The final R was determined to $R = 0.850 \pm 0.001\,9$.

When the corresponding fluxes of both SiPM and PMT are inserted in eq. 4.2, it leads to:

$$\frac{N_\gamma^{\mathrm{SiPM}}}{\mathrm{PDE} \cdot A_{\mathrm{SiPM}}} \stackrel{!}{=} R \cdot \frac{N_\gamma^{\mathrm{PMT}}}{\mathrm{DE} \cdot A_{\mathrm{PMT}}} \,. \tag{4.3}$$

The efficiency of the SiPM is the PDE whereas for the PMT, it is the DE (see sec. 1.3.5 and 1.4.3 for more details). For a reference detector with a known DE, all parameters of eq. 4.3 can be determined except the PDE which can be obtained by rearranging eq. 4.3 to:

$$\mathrm{PDE} = \frac{\mathrm{DE}}{R} \cdot \frac{A_{\mathrm{PMT}}}{A_{\mathrm{SiPM}}} \cdot \frac{N_\gamma^{\mathrm{SiPM}}}{N_\gamma^{\mathrm{PMT}}} \cdot \frac{1}{1 + P_{\mathrm{CT}}} \,. \tag{4.4}$$

The term $1/(1 + P_{\mathrm{CT}})$ is the correction for CT which has to be made to account for the CT events. As already explained in sec. 1.3.4.3, CT leads to the wrongful enhancement of the number of detected photons which strongly deteriotes the PDE determination. The correction for CT events has to be included in the PDE calculation.

4.2.2 PDE Measurement

The measurement procedure was similar to chapt. 2. An α-source was used to excite the xenon atoms and produce scintillation light. They are emitted with a frequency of 3.9 kBq. In contrast to chapt. 2, in which the trigger was externally controlled by the pulse generator, this is not possible now. The PMT was used as a trigger instead. Many thousands of photons are produced in a single α-track which are emitted in all directions. Due to the large photon flux onto the PMT, it could be clearly distinguished between a real signal and noise. The DCR of the PMT can be neglected because the activity of the source is much higher than the DCR. Every trigger corresponds to the detection of a real light signal. It is very likely that photons impinge onto the SiPM when the PMT is triggered.

Both SiPM and PMT signals are saved. The procedure is similar to sec. 2.3.1. Figure 4.5 shows the basic approach. All plots on the left show single waveforms. The plot on the top describes the light pulse. Both plots below (red lines) refer to the PMT measurement. As the trigger was set onto the PMT at a level above electronic noise, every triggered event contains a real PMT signal. This includes two different contributions. On the one hand, there are relatively small signal amplitudes. These are caused by α-particles absorbed in the aluminium holder. On the other hand, α-particles are stopped in the GXe. This results into higher amplitudes. These two pulse height distributions are also visible in the corresponding charge spectrum on the right above. For the SiPM, this is similar. This is illustrated by the lower plots in blues.

All waveforms of the SiPM and PMT response are integrated. This is on the one hand because not all photons reach the detector simultaneously but delayed in time due to reflections inside the chamber. On the other hand, the CT and AP requirements for the nEXO experiment are specified

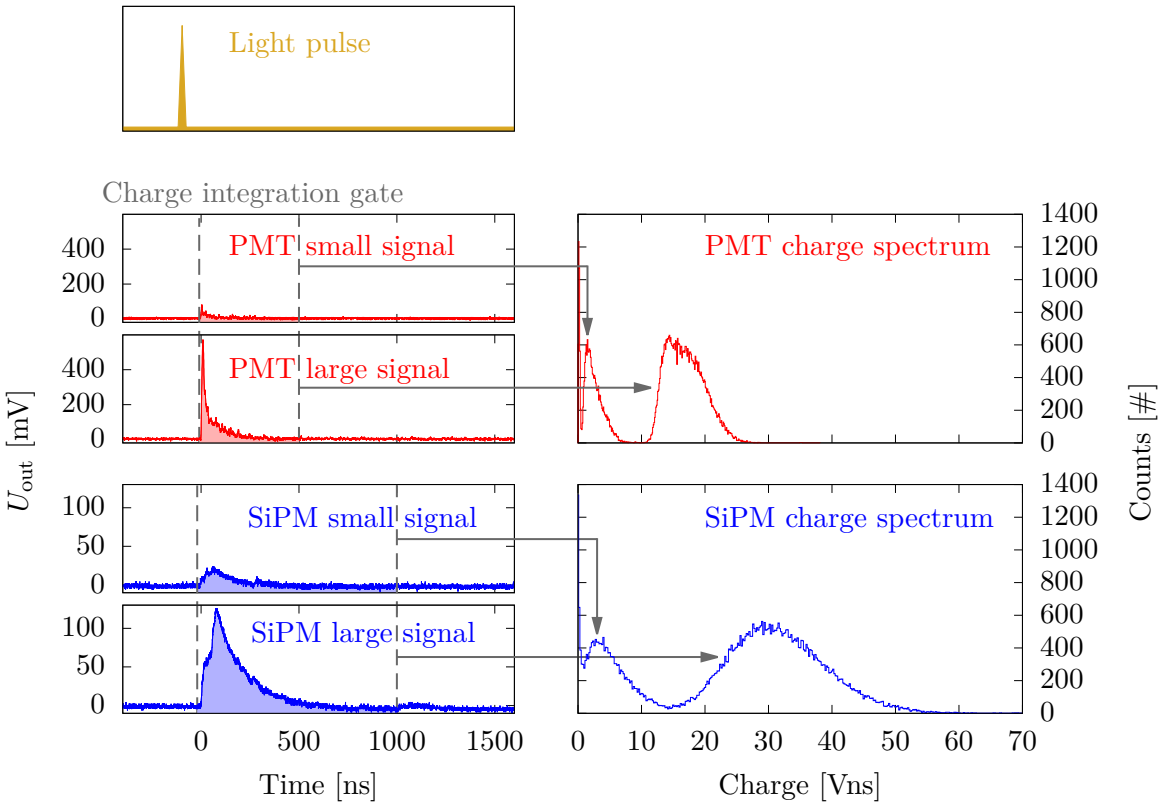

Figure 4.5: Illustration of the data acquisition and analysis procedure. Two exemplary pulses are plotted for each detector. All PMT waveforms are integrated from −10 ns to 500 ns and result in the charge spectrum in red. The SiPM signals are integrated from −20 ns to 1 000 ns and generate a corresponding charge spectrum in blue.

within 1 µs after the prompt pulse. A charge integration gate of 1 µs was chosen for the SiPM. In case of the PMT, the signals were integrated between −10 ns and 500 ns. An example of the final charge spectra can be seen in fig. 4.5.

It is important to know to how many photons this signal corresponds. In principle, all waveforms of the light measurement must be integrated up to 1 µs and divided by the value of 1 p.e. This is one possibility. Another approach was used in this work. The dark measurements are firstly integrated up to 1 µs after the trigger. It is important to choose exactly the same integration window as for the measurements with illumination. This is because one assumes that the dark measurements suffer in the same extent of CT as the ones with illumination. Then the number of detected photons of the SiPM is obtained by dividing the mean value of the spectrum of the measurement with light by the mean of the spectrum of the dark measurement. As both light and dark spectra are affected by CT equally, this method already yields the CT correction. For the PMT, no such effects occur or they can be neglected, respectively. The mean of the charge

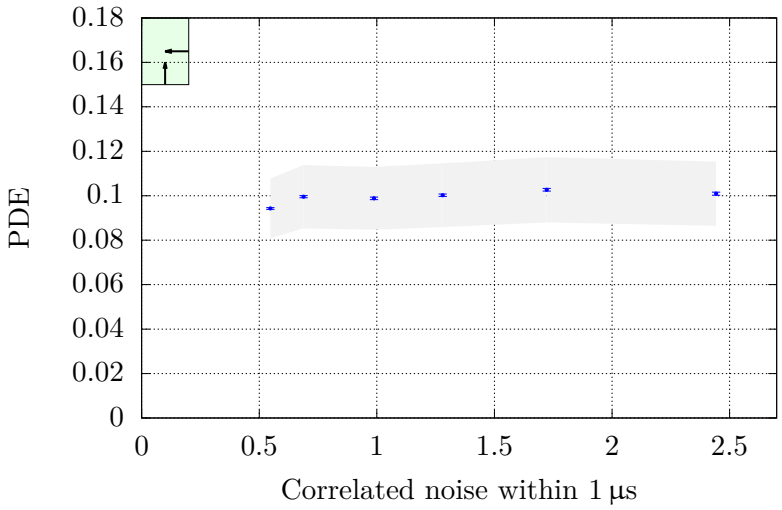

Figure 4.6: PDE versus correlated noise within 1 µs. The errorbars indicate the corresponding statistical error and the grey band the systematic error. The green rectangle shows the region in which the requirements for the nEXO experiment are fulfilled.

spectrum with illumination is only divided by the value of the 1 p.e which has been determined in chapt. 2. The final formula for the PDE calculation is:

$$\mathrm{PDE} = \frac{\mathrm{DE}}{R} \cdot \frac{A_{\mathrm{PMT}}}{A_{\mathrm{SiPM}}} \cdot \frac{m_{\mathrm{light}}^{\mathrm{SiPM}}/m_{\mathrm{dark}}^{\mathrm{SiPM}}}{m_{\mathrm{light}}^{\mathrm{PMT}}/Q_1}\,, \tag{4.5}$$

where m denotes the respective mean value of the spectrum and Q_1 the charge value of the 1 p.e. at $-100\,^{\circ}\mathrm{C}$ from chapt. 2. With this formula, the final PDE was determined for different overvoltages. This is shown in fig. 4.6. The PDE is plotted depending on the correlated noise including CT as well as AP events within 1 µs after the original pulse. It is determined similar to the number of CT events in sec. 3.3.4.3. The mean of the spectrum is divided by the gain value for this spectrum and then subtracted by one in order to exclude the 1 p.e. event which is not affected from CT:

$$\mathrm{CT} + \mathrm{AP}(t < 1\,\mu\mathrm{s}) = \frac{m}{G} - 1\,.$$

The errorbars refer to the corresponding statistical errors. They mainly arise from the Poissonian errors of the spectra. The grey band indicates the systematic error. It is discussed in the next section. With increasing U_{over}, not only the PDE, but also the correlated noise increases. The green box shows the required values for the nEXO experiment. The measured values do not fulfil these requirements.

Reflections of the incident light at the PMT surface have to be taken into account, too. The flux onto the PMT is actually higher than calculated in eq. 4.5. Its real value is estimated via a toy Monte Carlo simulation from [112]. A homogeneous three-dimensional radiating sphere with a radius of 1.8 cm corresponding to the track length of the α-particles was assumed. Only 5.5 % of the incoming light is reflected assuming a mean incident angle of the direct light of 25° onto the PMT surface and the refractive indices of 1.6 for quartz and 1.0 for GXe. Stray light has to be taken into account, too. It can have larger incident angles than the incident light. This leads to

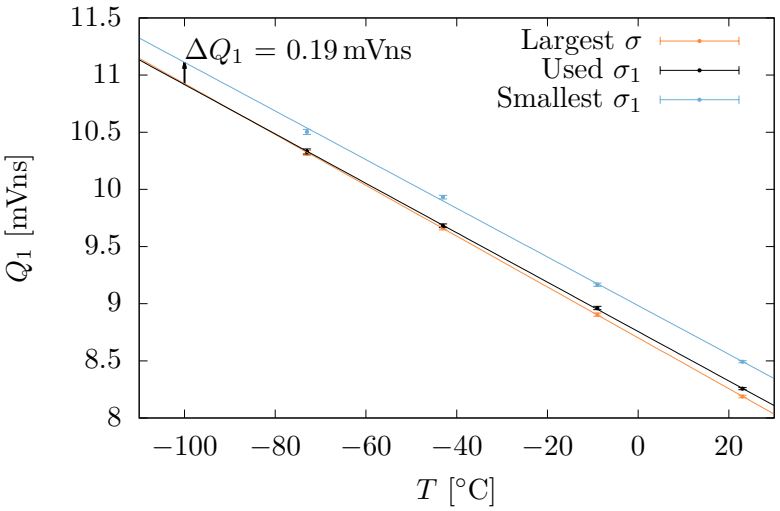

Figure 4.7: Illustration of the systematic error estimation for the Q_1 value. The difference to the mean Q_1 indicates the corresponding systematic error.

reflection losses of about 11 % to 15 %. This results into a reduction of the PDE by a factor of 0.89 to 0.85.

4.2.3 Systematic Error Consideration

The determination of the PDE involves many different parameters which contain systematic errors. These are propagated to the PDE value. The systematic errors of the relevant parameters are discussed below. The main ones are Q_1 and the detection efficiency of the PMT including CE and QE. But also the errors of R and of the areas of the detectors are considered.

Q_1 of PMT:
The Q_1 value of the PMT was determined within the absolute calibration of the PMT in chapt. 2. A fit was performed with Q_1 as one of the fit parameters. As already mentioned, the main problem was that the width σ_1 of the Q_1 value had to be restricted so that the fit was possible. This caused the fit to run into the upper fit limit in about half the cases. This imposes a systematic error onto Q_1. In order to account for this, an error estimation was performed in the following way. The upper limit of the σ_1 value was increased as far as the fit was possible or reasonable. Then the same was done for the reduction of the upper limit. This was done for every fit and the extrapolated Q_1 at $-100\,°\mathrm{C}$ was determined for both cases. Then the difference to the Q_1 obtained in chapt. 2 was calculated. The resulting curves can be seen in fig. 4.7. The black curve corresponds to the Q_1 obtained in chapt. 2, the orange curve to the largest and the blue curve to the smallest possible σ_1. A larger upper limit results into a lower Q_1 and vice versa. As the slope of the largest σ_1 curve is steeper than the one of the black curve, the extrapolated Q_1 of the largest σ_1 is larger than the black curve instead of smaller as expected. A systematic error of -0 is assumed. The difference of the smallest σ_1 and the used Q_1 is $\Delta Q_1 = 0.19$. This gives for the final systematic error $Q_1 = \left(10.9^{+0.19}_{-0}\right)\,\mathrm{mVns}$.

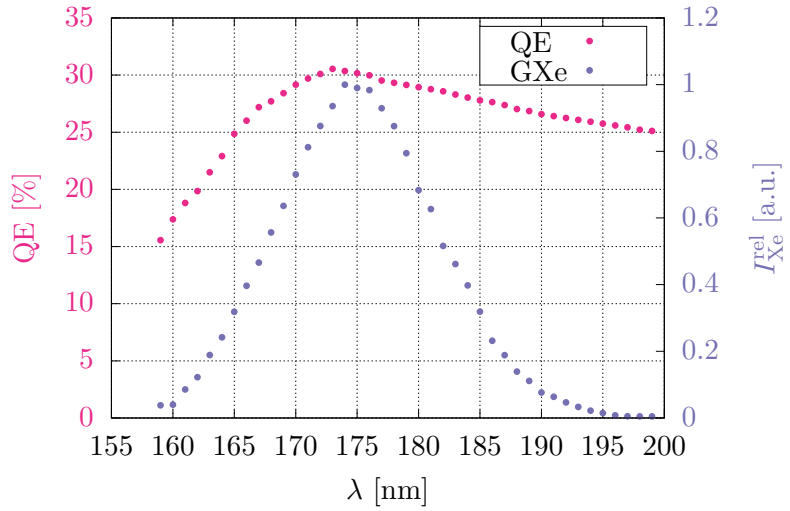

Figure 4.8: Response of the scintillation light of GXe [114] and the QE of the PMT [80] plotted in dependence on the wavelength. Both parameters are given as relative value normalised to their maximum. For the mean QE, a convolution of both curves has to be performed.

DE of PMT:
The systematic error of the DE of the PMT is formed by the QE and the CE. The CE is about 0.7 [113]. A conservative error estimation of CE $= 0.7 \pm 0.1$ is assumed. For the QE, it is different. The manufacturer stated that the QE is about 0.32 at the desired wavelength of 175 nm. But the xenon scintillation light does not peak sharply at exactly this wavelength. One has to take the full emission spectrum of GXe into account. Figure 4.8 shows the QE of the PMT depending on the wavelength as well as the emission spectrum from GXe. Both parameters are plotted as relative values normalised to their maximum. The emission spectrum of GXe was taken from [114] and binned in integer values. It peaks at 175 nm. The QE distribution is obtained from [80] and binned as well. The overall response of the PMT gives a mean quantum efficiency $\overline{\mathrm{QE}}$ and can be calculated via the convolution of the QE and scintillation spectrum:

$$\overline{\mathrm{QE}} = \sum_i \mathrm{QE}(\lambda_i) \cdot \frac{I_{\mathrm{Xe}}(\lambda_i)}{\sum_j I_{\mathrm{Xe}}(\lambda_j)}\,, \tag{4.6}$$

in which $I_{\mathrm{Xe}}(\lambda_i)$ is the intensity of the xenon scintillation light. This was performed in detail in [97]. It results into a mean quantum efficiency of $\overline{\mathrm{QE}} = 0.30 \pm 0.01$. The errors arise from the nonzero line width of spectrum representing an uncertainty in the binning.

Overview:
The areas of both detectors as well as the error of the R correction factor yield systematic errors as well. The sensitive area of the PMT is 420.25 mm^2. It was measured with a calliper with a precision of 0.1 mm. This gives a value of $A_{\mathrm{PMT}} = (420.25 \pm 4.11)\,\mathrm{mm}^2$. For the SiPM, the 6 mm side length from the datasheet was assumed with an error of 0.1 mm. This results into an absolute error of 1.2 mm^2. The error of the correction factor R is obtained from the simulation. Tabular 4.1 summarises all parameters with their absolute systematic error as well as the relative one. The relative errors of the areas as well as the error of R are considerable small and the three main contributions are the uncertainties of Q_1, QE and CE. The relative error of the CE is about one

Table 4.1: Systematical error contributions of the PDE.

Parameter		Value	Absolute Error	Relative Error	
$\overline{\text{QE}}$		0.30	0.01	3.33	%
CE		0.7	0.1	14.29	%
Q_1	[mVns]	10.9	0.19	1.7	%
A_{SiPM}	[mm^2]	36	1.2	3.33	%
A_{PMT}	[mm^2]	420.25	4.1	0.98	%
R		0.8450	0.0019	0.22	%

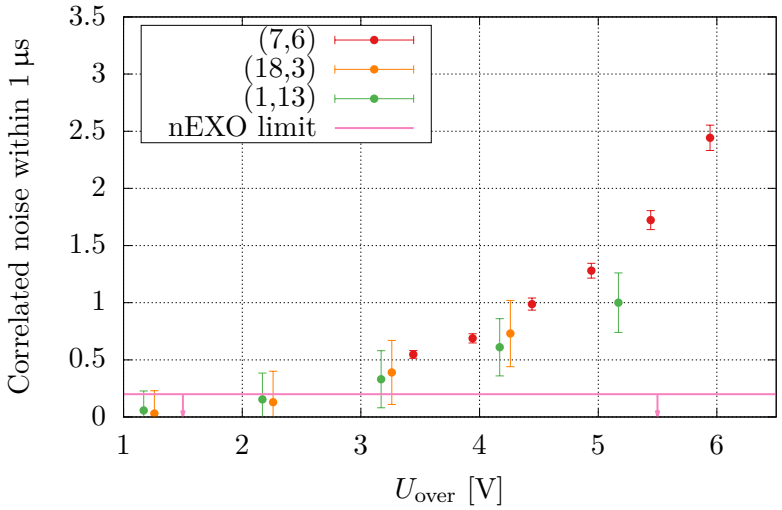

Figure 4.9: Correlated noise versus the overvoltage. The red line indicates the maximal tolerated correlated noise within 1 µs for the nEXO experiment.

order of magnitudes larger than all others. It is taken as the dominant systematic error of the PDE displayed as error band in fig. 4.6.

4.2.4 Further Analysis

Even though the PDE determination is the most important characteristic, further parameters can be investigated. One of them is the correlated noise within 1 µs which has not been discussed so far. A comparison of the measurement with the simulation which was used for the determination of the PDE is made as well as the investigation of the flux stability over time.

4.2.4.1 Correlated Noise

Only the single contributions to correlated noise – CT and AP – were investigated in sec. 3.3.4. For the nEXO specifications, the sum of both effects is relevant. Figure 4.9 shows the correlated noise depending on U_{over} for different devices. The red points represent the data of the SiPM at (7,6) measured in this work with their corresponding statistical errors whereas the orange and green points were measured in [106]. The demanded upper limit for the nEXO experiment for

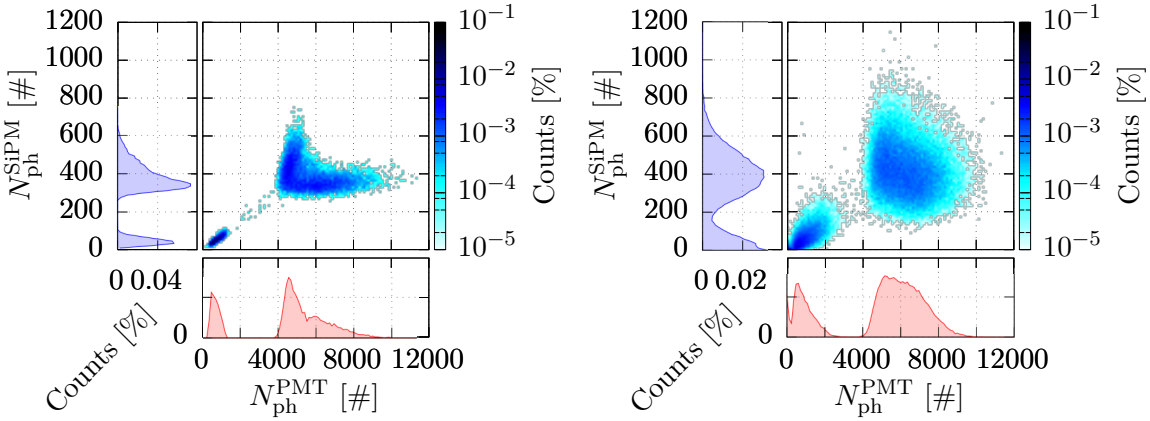

(a) Simulation. **(b)** Measurement.

Figure 4.10: Number of incident photons for the SiPM versus the one of the PMT for the simulation (a) and measurement (b) for several α-events. The colour indicates the frequency of the α-event normalised to its overall number. Each axis shows the projection of the corresponding detector.

correlated noise within 1 µs is shown in pink. The data of all devices show a quadratic dependence and are consistent within their statistical errors. All red datapoints lie above the nEXO limit. This indicates one of the main problems with the setup itself. The measured overvoltages are relatively large. This is due to the large electronic noise of the entire setup which made it impossible to distinguish a signal from the noise for $U_{\mathrm{over}} < 3\,\mathrm{V}$. For a lower electronic noise, it may be possible to measure lower overvoltages and obtain correlated noise values below the nEXO limit such as for the devices at (18,3) and at (1,13).

4.2.4.2 Comparison with Simulation

The simulation is used to determine the correction factor R for the PDE. Several assumptions of e.g. the refractive indices have been made (see sec. 4.2.1). To validate the simulation, it is compared to the data. This is visible in fig. 4.10. Both plots show $N_{\mathrm{ph}}^{\mathrm{SiPM}}$ per α-event versus $N_{\mathrm{ph}}^{\mathrm{PMT}}$ per α-event for (a) the simulation and (b) the measurement. The number of counts is displayed with a colour code and is normalised to the overall number of α-events. It is 15 000 for the simulation and 60 400 for the measurement. The projection is shown for each axis. Both simulation and measurement yield two distributions. One with relatively low photon number per event. These are generated by α-particles losing their energy in the aluminium holder. The second distribution is larger with a higher photon number per event. This is coming from α-particles with energy loss within the GXe. Within this distribution, an anticorrelation is visible. It comes from the arrangement of the detectors. A particle track going in the direction of the PMT will produce more incident photons onto the PMT than onto the SiPM and vice versa. The values of the simulation correspond with the measurement. Only the shape of N_{ph} is different. The distribution of the measurement is much broader and less sharp to the edges. This may indicate a stronger diffusion of the light.

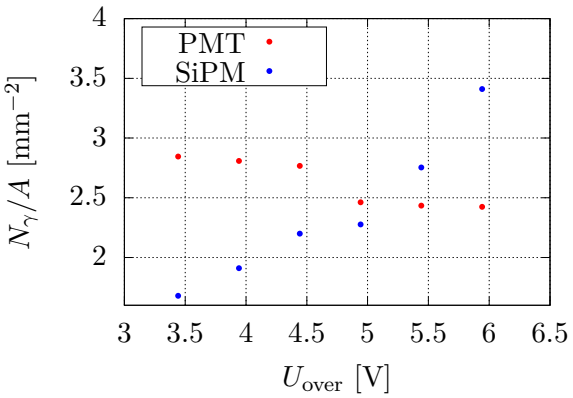

Figure 4.11: Number of detected photons per mm^2 for PMT in red and SiPM in blue.

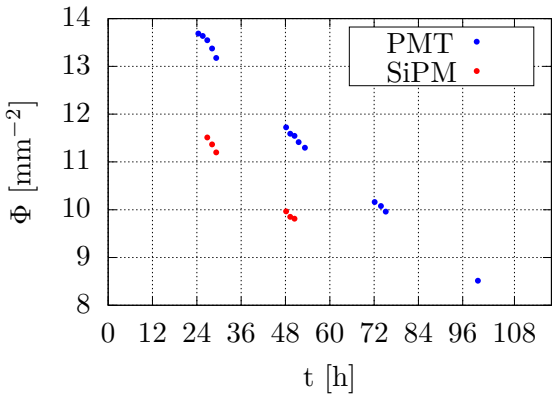

Figure 4.12: Flux of PMT and SiPM over time for SiPM and PMT.

4.2.4.3 Continuity of the Light Flux

For the comparison of measurements performed at different days, a stable behaviour over time is essential. To investigate this, N_γ is plotted versus U_{over} for both SiPM and PMT in fig. 4.11. For a better comparison, N_γ is normalised to the corresponding area of the detectors. For the PMT, N_γ/A is almost constant at about 2.5 photons/mm^2 whereas it is between 1.5 photons/mm^2 and 3.5 photons/mm^2 for the SiPM. The increase of N_γ for the SiPM with a higher U_{over} is due to the increasing PDE and CT probability. The incident flux should stay the same. Since the PMT has always been operated with the same supply voltage, one would expect a constant with increasing U_{over}. A slight decrease is visible.

To investigate this further, the incident flux Φ is plotted versus the time in fig. 4.12. Time zero is the time when the GXe was filled in the chamber. The flux is shown for both SiPM and PMT. Several aspects are visible. Firstly, the flux of the SiPM is always smaller than the one of the PMT. This is due to the asymmetry of the setup. When Φ_{SiPM} is divided by R, the same flux as for the SiPM is obtained. Secondly, Φ should stay the same over time which is not the case. The flux for both SiPM and PMT decrease almost linearly with time. A possible explanation is light pollution occuring with time. Due to the circulation of the gas inside the chamber, molecular impurities are released from the walls and from other components of the setup. These molecules accumulate at the xenon atoms. Propagating photons are more often scattered and absorbed at the molecules. This reduces the arriving flux at the detectors. After three days, the flux of the PMT is almost divided by a factor of two. This imposes a serious problem especially concerning the PDE measurements and may explain the deviation of simulation and data in sec. 4.2.2.

4.3 Discussion

The PDE of a VUV-sensitive SiPM from FBK was determined in dependence on the correlated noise. Although the data points of the PDE lie below the desired value for nEXO, this does not necessarily mean that the detector does not fulfil the requirements. The reason is that the PDE is angular dependent. For the setup used in this work, the mean incident angle is about 30 °. An increasing angle lowers the PDE. This relation makes a comparison with measurements of other collaborators difficult. For instance, measurements of the identical SiPM type processed from

the same wafer yield completeley different PDE values. The PDE is about 15 % [106] whereas it is about 10 % in this work. The incident angle in [106] was $\theta = 0°$. This explains the larger PDE values. For an appropriate characterisation with respect to the nEXO experiment, the same angular distribution as in the final experiment should be used. Another possibility is to measure the angular dependence of the PDE. In any case, the obtained PDE is already close to the lower limit for nEXO. But the large contribution of the correlated noise still imposes a major problem. It increases quadratically with U_{over} and is far too large. The decrease of the correlated noise with U_{over} is faster than the decrease of the PDE. In order to fulfil both requirements of PDE and correlated noise for the nEXO experiment, low overvoltages may be the best choice. In this setup, only overvoltages down to 3 V could be measured due to the large electronic noise and limitations in the analyis as discussed in sec. 3.4.

The measurement of the PDE yields extremely large systematic errors with the main contributions from uncertainties of the reference detector. An exact characterisation of the PMT is fundamental. This includes not only the absolute calibration, but also precise values for QE and CE with corresponding errors. As it can be seen in tab. 4.1, the CE is the parameter with the largest systematic error. Another problem is the systematic error of the Q_1 value. Extrapolation and fit result in relatively large uncertainties. In order to reduce them, an absolute calibration in this setup at $-100\,°\text{C}$ should be considered as well as improvements in the fit performance as already discussed in sec. 2.4.

Due to the asymmetric setup, the incident flux is not the same at SiPM and PMT. A simulation of the used setup has been performed to determine the correction factor R. The comparison of measurement and simulation yields consistent results. The more diffuse shape of the measurement can be explained by scattering of the photons.

Since the entire setup has to be evacuated first and then cooled down to $-100\,°\text{C}$, which takes at least one day with further time needed to measure the different overvoltages, the GXe stays at least two days inside the chamber without any purification. As already explained in sec. 4.2.4.3, the GXe is polluted over time. As this is a continuous process, the PDE is reduced for later measurements in case of a constant U_{over}. This effect complicates the comparison of different measurements at different times. An appropriate purification procedure is essential to guarantee a stable flux over time.

Chapter 5

Summary and Outlook

Within the scope of this thesis, a PMT of the type R8520-406 from HAMAMATSU K.K. and a SiPM of the type FBK VUV-HD LF from FBK have been investigated. An absolute calibration of the PMT between 23 °C and -73 °C has been performed for different intensities with an extrapolation to −100 °C in order to determine the integral value Q_1 at −100 °C. A pulsed LED has been used and a fit model describing the processes in a PMT sufficiently. The Q_1 has been determined to be (10.9 ± 0.1) mVns which is consistent with [97]. The SiPM has been investigated in the absence of light as well as with VUV-scintillation light of GXe at 175 nm. Several parameters such as gain, breakdown voltage, darkcount rate, afterpulsing probability, optical crosstalk, recovery time, rise time, fall time, correlated noise as well as photon detection efficiency have been determined and compared to measurements of other collaborators. Similar results have been obtained except larger fall time values, shorter recovery times, a far larger darkcount rate and two additional afterpulsing time constants compared to the device at (3,6). A simulation of the setup by [111] was used to determine the unknown correction factor R which is necessary for the determination of the PDE in the used setup. Simulation and measurement of this work are consistent. The measured values of correlated noise and PDE do not fulfil the requirements for the nEXO experiment. The correlated noise is too large for a demanded U_{over} larger than 3 V. The PDE never reaches the required minimum of 15 % for a mean incident angle of 30 °. Only the darkcount rate lies far below the maximal required 50 Hz/mm^2 at −104 °C.

With respect to the nEXO experiment, further measurements are necessary. In this work, the measurements were performed in GXe whereas the nEXO experiment will use LXe. A cold getter, safety valves, an aluminium bottle, a steel dewar and an electric winch are needed for the recuperation. Many thousands of SiPMs facing each other will be used in the nEXO experiment. When one SiPM is triggered, photons originating from optical crosstalk may reach another SiPM and trigger it. It should be investigated in what extent the SiPMs influence each other. An idea is to place two SiPMs face to face in a dark box and measure coincidences. For measurements of lower overvoltages, the electronic noise should be reduced. It is planned to modify and test a board of one of the other collaborators. An absolute calibration of the PMT at −100 °C within the xenon cell should be considered as well. To avoid electronic crosstalk, the LED should not be operated at cryogenic temperatures. A possible solution would be to use an optical fibre to guide the light inside the chamber.

List of Abbreviations

SM	Standard Model
$2\nu\beta\beta$**-decay**	double beta decay
$0\nu\beta\beta$**-decay**	neutrinoless double beta decay
NH	normal hierarchy
IH	inverted hierarchy
LXe	liquid xenon
SiPM	silicon photomultiplier
PMT	photomultiplier tube
TPC	time projection chamber
VUV	vacuum ultraviolet
DCR	darkcount rate
AP	afterpulsing
CT	optical crosstalk
PDE	photon detection efficiency
$U_{\mathbf{bias}}$	bias voltage
$U_{\mathbf{break}}$	breakdown voltage
$U_{\mathbf{over}}$	overvoltage
$U_{\mathbf{diff}}$	diffusion voltage
p.e.	photoelectron equivalent
QE	quantum efficiency
APD	avalanche photodiode
HV	high voltage supply
SES	single electron spectrum
FWHM	full width at half maximum
DE	detection efficiency
CE	collection efficiency
LN	liquid nitrogen
GN	gaseous nitrogen
rms	root mean square
GXe	gaseous xenon
MOS	Metal-Oxide-Silicon
OpAmp	operational amplifier
LF	low field

Bibliography

[1] W. Pauli. *Brief an die Gruppe der "Radioaktiven" 1930*. 1930.

[2] C. L. Cowan Jr. et al. "Detection of the Free Neutrino: A Confirmation". In: *Science* 124 (July 1956), pp. 103–104. DOI: 10.1126/science.124.3212.103.

[3] Majorana, E. "A symmetric theory of electrons and positrons". In: *Nuovo Cimento* 14 (1937), 171–184.

[4] W. H. Furry. "On Transition Probabilities in Double Beta-Disintegration". In: *Phys. Rev.* 56 (12 Dec. 1939), pp. 1184–1193. DOI: 10.1103/PhysRev.56.1184.

[5] R. J. McIntyre. "Theory of Microplasma Instability in Silicon". In: *Journal of Applied Physics* 32.6 (1961), pp. 983–995. DOI: 10.1063/1.1736199.

[6] R. H. Haitz. "Model for the Electrical Behavior of a Microplasma". In: *Journal of Applied Physics* 35.5 (1964), pp. 1370–1376. DOI: 10.1063/1.1713636.

[7] V. Golovin. "Avalanche Photodetector". In: *Russian Agency for Patents and Trademarks* Patent NO. RU 2142175 (1998).

[8] Z. Sadygov. "Avalanche Detector". In: *Russian Agency for Patents and Trademarks* Patent NO. RU 2102820 (1998).

[9] D. Renker and E. Lorenz. "Advances in solid state photon detectors". In: *Journal of Instrumentation* 4.04 (2009), P04004.

[10] A. Lehmann. *Detektoren für Teilchen und Strahlung 2*. Lecture. 2016.

[11] B. R. Martin and G. Shaw. *Particle Physics*. 3. WILEY, 2008.

[12] M. Goeppert-Mayer. "Double Beta-Disintegration". In: *Phys. Rev.* 48 (6 Sept. 1935), pp. 512–516. DOI: 10.1103/PhysRev.48.512.

[13] M. G. Inghram and J. H. Reynolds. "Double Beta-Decay of Te^{130}". In: *Phys. Rev.* 78 (6 June 1950), pp. 822–823. DOI: 10.1103/PhysRev.78.822.2.

[14] S. R. Elliott, A. A. Hahn, and M. K. Moe. "Direct evidence for two-neutrino double-beta decay in ^{82}Se". In: *Phys. Rev. Lett.* 59 (18 Nov. 1987), pp. 2020–2023. DOI: 10.1103/PhysRevLett.59.2020.

[15] J. J. Gomez-Cadenas et al. "The Search for neutrinoless double beta decay". In: *Riv. Nuovo Cim.* 35 (2012), pp. 29–98. DOI: 10.1393/ncr/i2012-10074-9.

[16] F. T. Avignone, S. R. Elliott, and J. Engel. "Double beta decay, Majorana neutrinos, and neutrino mass". In: *Rev. Mod. Phys.* 80 (2 Apr. 2008), pp. 481–516. DOI: 10.1103/RevModPhys.80.481.

[17] J. Schechter and J. W. F. Valle. "Neutrinoless double-β decay in SU(2)×U(1) theories". In: *Phys. Rev. D* 25 (11 June 1982), pp. 2951–2954. DOI: 10.1103/PhysRevD.25.2951.

[18] S. R. Elliott and P. Vogel. "Double beta decay". In: *Ann. Rev. Nucl. Part. Sci.* 52 (2002), pp. 115–151. DOI: 10.1146/annurev.nucl.52.050102.090641.

[19] W. Rodejohann. "Neutrino-less Double Beta Decay and Particle Physics". In: *Int. J. Mod. Phys.* E20 (2011), pp. 1833–1930. DOI: 10.1142/S0218301311020186.

[20] S. Adrián-Martínez et al. "Letter of intent for KM3NeT 2.0". In: *Journal of Physics G: Nuclear and Particle Physics* 43.8 (2016), p. 084001.

[21] A. Giuliani and A. Poves. "Neutrinoless Double-Beta Decay". In: *Advances in High Energy Physics* 2012 (2012), p. 38. DOI: 10.1155/2012/857016.

[22] A. Gando et al. "Search for Majorana Neutrinos near the Inverted Mass Hierarchy Region with KamLAND-Zen". In: *Phys. Rev. Lett.* 117.8 (2016). [Addendum: Phys. Rev. Lett.117, no.10, 109903(2016)], p. 082503. DOI: 10.1103/PhysRevLett.117.109903,10.1103/PhysRevLett.117.082503.

[23] *About SNOLAB*. 2012. URL: https://www.snolab.ca/about.

[24] L. Yang. *Status and Prospects for the EXO-200 and nEXO Experiments*. 2016.

[25] J. B. Albert et al. "Sensitivity and Discovery Potential of nEXO to Neutrinoless Double Beta Decay". In: (2017). arXiv: 1710.05075 [nucl-ex].

[26] I. Ostrovskiy et al. "Characterization of Silicon Photomultipliers for nEXO". In: *IEEE Transactions on Nuclear Science* 62.4 (2015), pp. 1825–1836. DOI: 10.1109/TNS.2015.2453932.

[27] nEXO Collaboration. *Material for public release*. 2016.

[28] KETEK. accessed: 4.10.2017. URL: https://4b0vz81vun5u2kaw7x3w6ptl-wpengine.netdna-ssl.com/wp-content/uploads/2016/01/ketek-sipm-technology-microcell-construction-standart-technology-700x305.jpg.

[29] H. Ibach and H. Lüth. *Festkörperphysik - Einführung in die Grundlagen*. 7. Springer, 2009.

[30] G. Lutz. *Semiconductor Radiation Detectors: Device Physics*. 2. Springer, 2007.

[31] V. Saveliev. "Silicon Photomultiplier - New Era of Photon Detection". In: *Advances in Optical and Photonic Devices*. Ed. by Ki Young Kim. Rijeka: InTech, 2010. Chap. 14. DOI: 10.5772/7150.

[32] KETEK. accessed: 4.10.2017. URL: https://www.ketek.net/sipm/technology/.

[33] N. Dinu. "Instrumentation on silicon detectors: from properties characterization to applications". Habilitation à diriger des recherches. Université Paris Sud - Paris XI, Oct. 2013.

[34] L. Evensen et al. "Guard ring design for high voltage operation of silicon detectors". In: *Nuclear Instruments and Methods in Physics Research* 337.1 (1993), pp. 44–52. DOI: https://doi.org/10.1016/0168-9002(93)91136-B.

[35] W. Shockley. "Problems related to p-n junctions in silicon". In: *Solid-State Electronics* 2.1 (1961), pp. 35–67. DOI: https://doi.org/10.1016/0038-1101(61)90054-5.

[36] P. Buzhan et al. “An advanced study of silicon photomultiplier”. In: *ICFA Inst. Bull* 21 (2001), p. 28.

[37] B. Dolgoshein et al. “Status report on silicon photomultiplier development and its applications”. In: *Nuclear Instruments and Methods in Physics Research* 563.2 (2006). TRDs for the Third Millenium, pp. 368–376. DOI: https://doi.org/10.1016/j.nima.2006.02.193.

[38] Klaus Alexander Tadday. “Scintillation Light Detection and Application of Silicon Photomultipliers in Imaging Calorimetry and Positron Emission Tomography”. Dissertation. Ruperto-Carola-University of Heidelberg, 2011. DOI: 10.11588/heidok.00012959.

[39] KETEK. accessed: 4.10.2017. URL: https://www.ketek.net/sipm/technology/device-parameters/.

[40] T. Frach et al. “The digital silicon photomultiplier - Principle of operation and intrinsic detector performance”. In: *2009 IEEE Nuclear Science Symposium Conference Record (NSS/MIC)*. Oct. 2009, pp. 1959–1965. DOI: 10.1109/NSSMIC.2009.5402143.

[41] M. Ramilli. “Characterization of SiPM: Temperature dependencies”. In: *2008 IEEE Nuclear Science Symposium Conference Record*. Oct. 2008, pp. 2467–2470. DOI: 10.1109/NSSMIC.2008.4774854.

[42] W. G. Oldham, R. R. Samuelson, and P. Antognetti. “Triggering phenomena in avalanche diodes”. In: *IEEE Transactions on Electron Devices* 19.9 (Sept. 1972), pp. 1056–1060. DOI: 10.1109/T-ED.1972.17544.

[43] Hamamatsu K.K. *MMC and MPPC module for precision measurement*. accessed: 4.10.2017. URL: http://www.hamamatsu.com/resources/pdf/ssd/mppc_kapd0004e.pdf.

[44] AdvanSiD. accessed: 4.10.2017. URL: http://advansid.com/technology/silicon-photomultipliers.

[45] C. Zener. “A Theory of the Electrical Breakdown of Solid Dielectrics”. In: *Proceedings of the Royal Society of London. Series A* 145.855 (1934), pp. 523–529.

[46] K. B. McAfee et al. “Observations of Zener Current in Germanium $p - n$ Junctions”. In: *Phys. Rev.* 83 (3 Aug. 1951), pp. 650–651. DOI: 10.1103/PhysRev.83.650.

[47] R. H. Haitz. “Mechanisms Contributing to the Noise Pulse Rate of Avalanche Diodes”. In: *Journal of Applied Physics* 36.10 (1965), pp. 3123–3131. DOI: 10.1063/1.1702936.

[48] J. Frenkel. “On Pre-Breakdown Phenomena in Insulators and Electronic Semi-Conductors”. In: *Phys. Rev.* 54 (8 Oct. 1938), pp. 647–648. DOI: 10.1103/PhysRev.54.647.

[49] S. Cova et al. “Avalanche photodiodes and quenching circuits for single-photon detection”. In: *Appl. Opt.* 35.12 (Apr. 1996), pp. 1956–1976. DOI: 10.1364/AO.35.001956.

[50] S. Cova, A. Lacaita, and G. Ripamonti. “Trapping phenomena in avalanche photodiodes on nanosecond scale”. In: *IEEE Electron Device Letters* 12.12 (Dec. 1991), pp. 685–687. DOI: 10.1109/55.116955.

[51] Y. Du and F. Retière. “After-pulsing and cross-talk in multi-pixel photon counters”. In: *Nuclear Instruments and Methods in Physics Research* 596.3 (2008), pp. 396–401. DOI: https://doi.org/10.1016/j.nima.2008.08.130.

[52] G. Vincent, A. Chantre, and D. Bois. "Electric field effect on the thermal emission of traps in semiconductor junctions". In: *Journal of Applied Physics* 50.8 (1979), pp. 5484–5487. DOI: 10.1063/1.326601.

[53] H. Schroeder. "Poole-Frenkel-effect as dominating current mechanism in thin oxide films—An illusion?!" In: *Journal of Applied Physics* 117.21 (2015), p. 215103. DOI: 10.1063/1.4921949.

[54] O. Mitrofanov and M. Manfra. "Poole-Frenkel electron emission from the traps in AlGaN/GaN transistors". In: *Journal of Applied Physics* 95.11 (2004), pp. 6414–6419. DOI: 10.1063/1.1719264.

[55] KETEK. accessed: 4.10.2017. URL: https://4b0vz81vun5u2kaw7x3w6ptl-wpengine.netdna-ssl.com/wp-content/uploads/2016/01/SiPM-Optical-Crosstalk-Mechanism.png.

[56] I. Rech et al. "A New Approach to Optical Crosstalk Modeling in Single-Photon Avalanche Diodes". In: *IEEE Photonics Technology Letters* 20.5 (Mar. 2008), pp. 330–332. DOI: 10.1109/LPT.2007.915654.

[57] A. L. Lacaita et al. "On the bremsstrahlung origin of hot-carrier-induced photons in silicon devices". In: *IEEE Transactions on Electron Devices* 40.3 (Mar. 1993), pp. 577–582. DOI: 10.1109/16.199363.

[58] N. Akil et al. "A multimechanism model for photon generation by silicon junctions in avalanche breakdown". In: *IEEE Transactions on Electron Devices* 46.5 (May 1999), pp. 1022–1028. DOI: 10.1109/16.760412.

[59] A. G. Chynoweth and K. G. McKay. "Photon Emission from Avalanche Breakdown in Silicon". In: *Phys. Rev.* 102 (2 Apr. 1956), pp. 369–376. DOI: 10.1103/PhysRev.102.369.

[60] J. Pulko. "A Monte-Carlo Model of a Silicon Photomultiplier". Dissertation. München: Technische Universität München, 2012.

[61] Gaosong Li. *Light detection with SiPMs for nEXO*. 2017.

[62] Hamamatsu Photonics K.K. "Photomultiplier Tubes - Construction and Operating Characteristics Connections to External Circuits". In: (1998). URL: https://wwwmu.mpp.mpg.de/docs/pmtconstruct.pdf.

[63] SENSE. accessed: 9.10.2017. URL: https://www.sense-pro.org/images/lll-sensors/pmt_principle.jpg.

[64] ADIT Electron Tubes ET Enterprises Limited. "Understanding Photomultipliers". In: (2011). URL: http://www.et-enterprises.com/files/file/Understanding-photomultipliers.pdf.

[65] S.O. Flyckt and C. Marmonier. "Photomultiplier Tubes - Principles and Applications". In: (2002). URL: http://www2.pv.infn.it/~debari/doc/Flyckt_Marmonier.pdf.

[66] Hamamatsu Photonics K.K. *Photomultiplier Tubes - Basics and Application*. 2007. URL: https://www.hamamatsu.com/resources/pdf/etd/PMT_handbook_v3aE.pdf.

[67] L. Classen. "The mDOM - a multi-PMT digital optical module for the IceCube-Gen2 neutrino telescope". Dissertation. Friedrich-Alexander-Universität Erlangen-Nürnberg, Feb. 2017.

[68] J. C. Barton. *Basic Physics and Statistics of Photomultipliers*. 2011. URL: http://www.et-enterprises.com/files/file/technical-information/rp063_basic%20physics%20statistics%20of%20PMTS.pdf.

[69] W. R. Leo. *Techniques for Nuclear and Particle Physics Experiments*. 2. Springer, 1994.

[70] Hamamatsu Photonics K.K. accessed: 12.10.2017. URL: https://www.hamamatsu.com/eu/en/technology/innovation/photocathode/index.html.

[71] B. H. Candy. "Photomultiplier characteristics and practice relevant to photon counting". In: *Review of Scientific Instruments* 56.2 (1985), pp. 183–193. DOI: 10.1063/1.1138327.

[72] A. G. Wright. *Sources of Noise in Photomultipliers*. 2011. URL: http://www.et-enterprises.com/files/file/technical-information/rp068_sources%20of%20noise%20in%20photomultipliers.pdf.

[73] A. G. Wright. "An investigation of photomultiplier background". In: *Journal of Physics E: Scientific Instruments* 16.4 (1983), p. 300. URL: http://stacks.iop.org/0022-3735/16/i=4/a=014.

[74] O. Ju. Smirnov, P. Lombardi, and G. Ranucci. "Precision Measurements of Time Characteristics of ETL9351 Photomultipliers". In: *Instruments and Experimental Techniques* 47.1 (Jan. 2004), pp. 69–80. DOI: 10.1023/B:INET.0000017255.60520.e0.

[75] B. K. Lubsandorzhiev et al. "Studies of prepulses and late pulses in the 8 inch electron tubes series of photomultipliers". In: *Nuclear Instruments and Methods in Physics Research* 442.1 (2000), pp. 452–458. DOI: https://doi.org/10.1016/S0168-9002(99)01272-3.

[76] P. B. Coates. "Photomultiplier collection efficiencies and nonpoissonian pulse height distributions". In: *Journal of Physics D: Applied Physics* 6.2 (1973), p. 153. URL: http://stacks.iop.org/0022-3727/6/i=2/a=303.

[77] B. K. Lubsandorzhiev et al. "Photoelectron backscattering in vacuum phototubes". In: *Nuclear Instruments and Methods in Physics Research* 567.1 (2006). Proceedings of the 4th International Conference on New Developments in Photodetection, pp. 12–16. DOI: https://doi.org/10.1016/j.nima.2006.05.047.

[78] E. H. Bellamy et al. "Absolute calibration and monitoring of a spectrometric channel using a photomultiplier". In: *Nuclear Instruments and Methods in Physics Research* 339.3 (1994), pp. 468–476. DOI: https://doi.org/10.1016/0168-9002(94)90183-X.

[79] S. Tokar et al. *Single Photoelectron Spectra Analysis for the Metal Dynode Photomultiplier*. 1999.

[80] Hamamatsu Photonics K.K. accessed: 23.10.2017. URL: https://www.hamamatsu.com/resources/pdf/etd/R8520-406_TPMH1342E.pdf.

[81] Hamamatsu Photonics K.K. accessed: 22.10.2017. URL: https://www.hamamatsu.com/blobs/.

[82] iseg Spezialelektronik GmbH. accessed: 14.11.2017. URL: https://www.franke-iv.de/Iseg/manual%20shq%20x2x.pdf.

[83] Agilent Technologies. accessed: 23.10.2017. URL: http://data.leocom.kr/datasheets/290281_25602.pdf.

[84] Philips. accessed: 23.10.2017. URL: http://www.download-service-manuals.com/.

[85] LeCroy. accessed: 23.10.2017. URL: https://www.valuetronics.com/pub/media/vti/datasheets/.

[86] LeCroy. accessed: 23.10.2017. URL: https://www.testequity.com/documents/chambers/1007C-EZ.pdf.

[87] Leybold. accessed: 23.10.2017. URL: https://www.leybold-shop.de.

[88] LD Didactic. accessed: 23.10.2017. URL: https://www.ld-didactic.de/documents/de-DE/GA/GA/5/524/524013d.pdf.

[89] H. J. C. Berendsen. *A Student's Guide to Data and Error Analysis*. 1. Cambridge University Press, 2011.

[90] C. Van Eldik. *Methoden der Datananalyse*. Lecture. WS 2014/15.

[91] I. Jung. *Datenanalyse II und C++ Programmierung*. Lecture. WS 2016/17.

[92] S. Brandt. *Data Analysis - Statistical and Computational Methods for Scientists and Engineers*. 3. Springer, 1999.

[93] H. M. Araújo et al. "Low-temperature study of 35 photomultiplier tubes for the ZEPLIN III experiment". In: *Nuclear Instruments and Methods in Physics Research* 521.2 (2004), pp. 407–415. DOI: https://doi.org/10.1016/j.nima.2003.10.094.

[94] A. Lyashenko et al. "Measurement of the absolute Quantum Efficiency of Hamamatsu model R11410-10 photomultiplier tubes at low temperatures down to liquid xenon boiling point". In: *Journal of Instrumentation* 9.11 (2014), P11021. URL: http://stacks.iop.org/1748-0221/9/i=11/a=P11021.

[95] E. Aprile et al. "Measurement of the quantum efficiency of Hamamatsu R8520 photomultipliers at liquid xenon temperature". In: *Journal of Instrumentation* 7 (Oct. 2012), P10005. DOI: 10.1088/1748-0221/7/10/P10005.

[96] M. Prata et al. "Performance and behaviour of photomultiplier tubes at cryogenic temperature". In: *Nuclear Instruments and Methods in Physics Research* 567.1 (2006). Proceedings of the 4th International Conference on New Developments in Photodetection, pp. 222–225. DOI: https://doi.org/10.1016/j.nima.2006.05.092.

[97] P. Hufschmidt. "Characterizing a Wavelength Shifter Coated Silicon Photomultiplier at Cryogenic Temperatures using Scintillation Light in Gaseous Xenon". Master's Thesis. Friedrich-Alexander-Universität Erlangen-Nürnberg, 2017.

[98] Edwards. accessed: 16.11.2017. URL: http://scienceservices.de/media/pdf/Edwards_RV3_5_8_technisches_Datenblatt.pdf.

[99] BOC Edwards. accessed: 16.11.2017. URL: http://www.idealvac.com/files/ManualsII/Edwards_GVSP30_User_Manual.pdf.

[100] Pfeiffer Vacuum GmbH. *Betriebsanleitung TPH 180 H/ TPU 180 H Turbomolekularpumpe*.

[101] H. Stöcker. *Taschenbuch der Physik*. 5. Wissenschaftlicher Verlag Harri Deutsch, 2005.

[102] Honeywell. accessed: 14.11.2017. URL: https://sensing.honeywell.com/honeywell-sensing-hel-700-series-thin-film-platinum-rtd-productsheet-009080-1-en.pdf.

[103] Meilhaus Electronic GmbH. *RedLab 3104 - USB-based Analog Output*. URL: https://www.meilhaus.org/downloadserver/redlab/manual/RedLab%203104_en.pdf.

[104] Hewlett Packard. accessed: 14.11.2017. URL: https://edisciplinas.usp.br/pluginfile.php/2405092/mod_resource/content/1/Agilent_E3631%20Power%20Supply_Users_Guide%20%284%29.pdf.

[105] T. Ziegler. "Characterisation of Silicon Photomultipliers with Xenon Scintillation Light for the nEXO Experiment". Master's Thesis. Friedrich-Alexander-Universität Erlangen-Nürnberg, 2016.

[106] A. Jamil. "Development of a large area silicon photomultiplier array for light detection in liquid xenon". Master's Thesis. Friedrich-Alexander-Universität Erlangen-Nürnberg, 2017.

[107] Polytec PT GmbH. accessed: 14.11.2017. URL: http://www.polytec.com/fileadmin/user_uploads/Polytec_EC_101_eng.pdf.

[108] Analog Devices. accessed: 14.11.2017. URL: http://www.analog.com/media/en/technical-documentation/data-sheets/ADA4895-1_4895-2.pdf.

[109] P. J. Naish and S. Hartwell. "Exponentially Modified Gaussian functions—A good model for chromatographic peaks in isocratic HPLC?" In: *Chromatographia* 26.1 (Dec. 1988), pp. 285–296. DOI: 10.1007/BF02268168.

[110] L. Gallego et al. "Modeling crosstalk in silicon photomultipliers". In: *JINST* 8 (2013), P05010. eprint: 1302.1455.

[111] R. Bayerlein. "Simulation of Alpha Particle Scintillation Light in Liquid and Gaseous Xenon with Respect to Surface Reflections". Master's Thesis. Friedrich-Alexander-Universität Erlangen-Nürnberg, 2016.

[112] T. Michel. *Numerische Simulation Reflexionen auf PMT*. 14.12.2016.

[113] Y. Wei et al. "Study of light detection and sensitivity for a ton-scale liquid xenon dark matter detector". In: *JINST* 8 (2013), T06002. DOI: 10.1088/1748-0221/8/06/T06002.

[114] J. Jortner et al. "Localized Excitations in Condensed Ne, Ar, Kr, and Xe". In: *The Journal of Chemical Physics* 42.12 (1965), pp. 4250–4253. DOI: 10.1063/1.1695927.

Acknowledgements

I would like to express my deep gratitude, warmth and appreciation to the persons below who made my research successful and assisted me at every point to cherish my goal:

- **Prof. Dr. Gisela Anton** for her vital support and encouragement as well as the possibility to write my Master's thesis about this topic.
- **PD Dr. Thilo Michel** for his patient guidance and his enthusiastic encouragements throughout my entire work. I would like to express my very great appreciation for the possibility of various official journeys and his assistance in keeping my progress on schedule as well as his genuinely care about future perspectives.
- **Michael Wagenpfeil** for his valuable and constructive suggestions during the planning and development of my research work. I appreciated the valuable discussions, useful critiques and his willingness to give his time so generously very much.
- **Patrick Hufschmidt** for his support during all kinds of problems in the laboratory and his creative solutions. His sympathetic attitude and encouragements helped me many times during my thesis.
- **Tobias Ziegler** who helped me throughout my entire SiPM measurements and with the analysis.
- **Ako Jamil** who has already been a fantastic supervisor during my Bachelor thesis. I would like to thank him especially for his ideas and support during my PMT measurements.
- **Sebastian Schmidt** for his very patient help during various technical problems especially with python and his creative efforts to organise the work a little more diverse. He increased my frustration tolerance a lot!
- **Katharina Witzmann** for her readiness and patience to assist me with the simulation.
- My entire **work group** for the great teamwork. A Paperchase of a special kind and various inventive hiding places (ceiling!) for my sweets provided some variety in the daily routine.
- **Jutta Dziwis** without whom I would never be able to make a proper travel expense accounting. Her advice to many organisational matters was very useful.
- I would like to offer my sincerest gratitude to all colleagues at the institute, which I cannot list individually at this point due to lack of space. My special thanks are extended to **Lew**

Classen and **Oleg Kalekin** whose immense knowledge and advice about PMTs was very helpful. I would further like to thank **Jonas Reubelt** for the help with the programme for the binary readout of the oscilloscope and **Max Schuster** for his patience to dicuss various problems.

- My entire **family**, especially my father for his support during complicate inkscape, latex or gnuplot difficulties. I would like to thank my mother who did everything to help me during my work and studies as well as my brother who can do magic with all technical devices and fix many problems.
- I am particularly grateful for the assistance of my friends during my entire work. I wish to acknowledge **Lisa Ackermann** for the super teamwork throughout the entire studies, exam preparation and the lab courses. Many adventurous bike, train and car rides with **Theresa Leicht** gave the studies more fun. Finally, I would like to thank **Irene Schleifer** and **Rebecca Bauer** for their constant motivation, support and encouragements.

Statutory Declaration

I declare that I have developed and written the enclosed Master's Thesis completely by myself, and have not used sources or means without declaration in the text. Any thoughts from others or literal quotations are clearly marked. The Master's Thesis was not used in the same or in a similar version to achieve an academic grading or is being published elsewhere.

Erlangen, January 10, 2018

Judith Schneider